FRIENDS OF THE PLEISTOCENE

MISSING
INCIPIENT UNCOUNTED
ABSENT
SLIP
LOST
DIFFUSE
INSUFFICIENT
?
LIKE-THE-2018-FOP
404
STRIKE
MISMATCHED
AWOL
DISTRIBUTED

2019 REUNION TOUR IN THE CENTRAL WALKER LANE

Pacific Cell Field Trip Guidebook

October 3-6th, 2019

Trip leaders: Ian Pierce, Marith Reheis, Ken Adams, Jayne Bormann, Annie Kell, Chad Carlson, Craig dePolo, Bill Hammond, Rachel Hatch, Noah Abramson

Contents

0 Road Logs & How to use this guidebook

0.1 How to use this guidebook

Along with this guidebook we have provided several zip files. The first file contains a number of papers and figures – treat this as an appendix and supplementary info. We don't expect you to look at any of them.

The second file contains a series of PDF maps – these are mostly lidar hillshades of the various stops. We highly suggest you load these onto your tablet or phone using Avenza PDF maps so that you can look at the data while we discuss it and walk around the various sites. The free version Avenza only allows you to load 3 maps at a time. That is OK – just make sure you save all the files to your phone ahead of time. IF you have an apple product you might need to download a file manager app to do this. Goodluck.

For the road log: in the following sections we provide google maps links that are accurate for most of the stops, a table of coordinates for the stops, and turn by turn directions for each day.

We are traveling long distances between gas stations. Please arrive on Thursday night / Friday morning with a full tank of fuel. We are also doing a lot of travel on well-maintained gravel roads. Please have a good spare and tools to change it. Bring your own water. Carpool if you can.
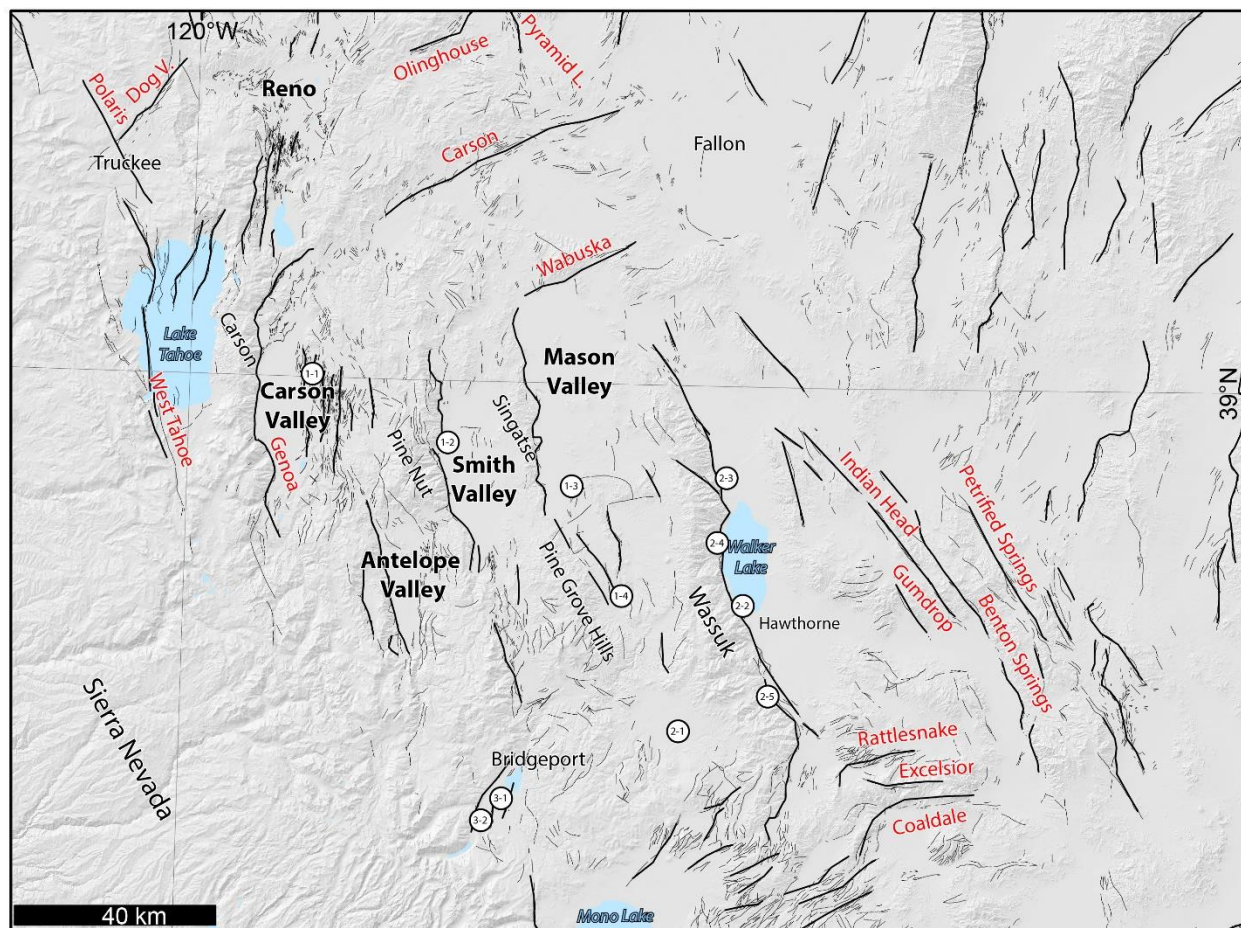
Overview of field trip showing major faults, mountain ranges, and stops.

0.2 Road logs

Overview with coordinates and maps links

Day	Stop #	Stop name	Lat	Long	UTM E (Zone	UTM N 11N)	Google maps directions link
Thursday 10/3	**Camp**	**Eldon Road Camp**	**38.996702**	**-119.676462**	**268212**	**4319819**	https://goo.gl/maps/G5D7yEdqd5tbRwdK6
Friday	All route						https://goo.gl/maps/C9HRAsNVmsJfrBC69
Friday 10/4	1	East Carson Overview	38.996702	-119.676462	268212	4319819	n/a
Friday 10/4	2	Artesia Fan	38.887848	-119.413486	290669	4307100	https://goo.gl/maps/nXqx5LgKqtcFuH5T7
Friday 10/4	3	Mason Overview	38.838028	-119.145041	313825	4300989	https://goo.gl/maps/AiCT3sHbH5pCnpJS8
Friday 10/4	4	Pine Grove Hills	38.629594	-118.997965	326086	4277567	https://goo.gl/maps/vCqYgUBJLXaGN8Za8
Friday 10/4	**Camp**	**Fletcher Spring**	**38.359381**	**-118.897964**	**334173**	**4247395**	https://goo.gl/maps/PYcbhyvVTUNSrCJx5
Friday 10/4	Camp Alternate	Mine	38.426034	-118.737653	348320	4254516	n/a
Saturday	All route						https://goo.gl/maps/8y87kv14DBvBTBZd6
Saturday 10/5	1	Fletcher Valley	38.374509	-118.809305	341953	4248918	https://goo.gl/maps/CtFrysqckEbQVYq78
Saturday 10/5	2	Wassuk SS Overlook	38.580276	-118.703301	351636	4271577	https://goo.gl/maps/JNRChmTv3dawKoCBA
Saturday 10/5	3	Wassuk Shorelines	38.923341	-118.806492	343399	4309821	https://goo.gl/maps/V5DqgxXbjDcPhkaz9
Saturday 10/5	4	Copper Canyon	38.737796	-118.771793	346007	4289170	https://goo.gl/maps/hTfAoM8LcYUjmA1o8

Day		Location	Lat	Long			Link
Saturday 10/5	5	North Canyon	38.451245	-118.663017	354886	4257193	https://goo.gl/maps/cDqsteLVHsbATENT6
Saturday 10/5	**Camp**	**Fletcher Spring**	**38.359381**	**-118.897964**	**334173**	**4247395**	https://goo.gl/maps/qwvPSsuoNtdCfsj76
Sunday							
Sunday 10/6	1	Twin Lakes Road	38.241832	-119.249744	303117	4235041	https://goo.gl/maps/jgen5d9JibsYmuBYA
Sunday 10/6	2	Moraines	38.217569	-119.308094	297943	4232474	https://goo.gl/maps/4xBWd4E4BTYVJg329

DAY 1	Miles from previous Turn	Odometer	Description
Stop 1		0	From camp
Drive down Eldon Road west		0	
Turn left onto E Valley Road	1.7	1.7	
Turn left onto Fish Springs Rd	4.3	6	
Turn right onto E Valley Rd	0.3	6.3	
Turn right onto Pinenut Rd	1.6	7.9	
At traffic circle take 3rd exit onto Muller Pkwy	1.1	9	
Turn left onto US 395 S	0.3	9.3	
Turn left onto NV 208E	15.9	25.2	
Turn left onto Lower Colony Rd	9.8	35	
Turn left onto Artesia Rd	7.1	42.1	
Arrive at Stop 2	2.8	44.9	Turn around in gravel quarry and park along road
Total since last stop	**44.9**		
Stop 2		44.9	
Head southwest on Artesia Rd		44.9	
Turn right onto lower colony road	2.8	47.7	
Turn left onto Day Lane	2	49.7	
Turn left onto NV 208E	5.5	55.2	Last gas is to the left off of NV 208 1.3 miles past turn
Arrive Stop 3	11.1	66.3	
Total since last stop	**21.4**		
Stop 3		66.3	
Head south on State Rt 3c/E Walker Rd		66.3	
Arrive Stop 4	16.8	83.1	
Total since last stop	**16.8**		
Stop 4		83.1	
Continue south on State Rt 3c/E Walker Rd		83.1	

Turn left onto NF-026 at major 4 way intersection signed for Hawthorne, Aurora,	22.8	105.9	
Take first right	0.7	106.6	
Take first right again into camp area (Fletcher Spring)	0.3	106.9	
Total since last stop	**23.8**		

DAY 2	Miles from previous turn	Odometer	Description
Camp		0	
Turn left from springs to head back towards NF-026		0	
Turn right (east) onto NF-026	0.3	0.3	
Arrive stop 1	4.7	5	
Total since last stop	**5**		
Stop 1		5	
Continue E on NF-026 / Lucky Boy Pass Road		5	
Turn left on State Rte 359 N	13.2	18.2	Watch for cross traffic
Continue onto US 95 N	3.8	22	25 mph speed limit in Hawthorne, Get gas if you need it but we will be returning at end of day.
Arrive Stop 2	6	28	Take care entering and exiting highway 95, traffic is very fast. Pull off and form multiple stacks of cars in the pullot.
Total since last stop	**23**		
Stop 2		28	
Continue N on US 95		28	Take care entering highway, traffic is very high speed
Turn right into abandoned gas station	26.5	54.5	make wide u-turn here, we are turning around to head back south on 95
Turn left onto 95 S	0.1	54.6	Take care turning left, there is high speed traffic
Arrive Stop 3	0.3	54.9	Pull off in truck stop here. Be careful of broken glass
Total since last stop	**26.9**		
Stop 3		54.6	
Continue S on US 95 S		54.9	
Turn right onto unmarked dirt road	14.3	69.2	Take care exiting highway. Road is 0.6 miles past turn for Tammarack beach
Turn right onto another unmarked dirt road	0.1	69.3	

Arrive Stop 4	0.8	70.1	
Total since last stop	**15.2**		
Stop 4		70.1	
Turn around and head back to highway		70.1	
Turn right onto US 95 S	0.9	71	Take care entering highway
Continue Straight onto 359 S / thru downtown Hawthorne	17.9	88.9	25 mph speed limit in Hawthorne, Get gas if you haven't yet
Turn right onto Lucky Boy Pass road	3.8	92.7	
Turn left onto unnamed dirt road	0.5	93.2	
Turn right onto unmarked dirt road	1	94.2	
Arrive at Stop 5	1	95.2	follow dirt road back to N then sharply to W (up drainage) when it approaches a fan channel
Total since last stop	**25.1**		
Stop 5		95.2	
Turn around and head back down fan on same road we entered		95.2	
Turn left onto unmarked road	1	96.2	
Turn left onto Luck Boy pass road	0.9	97.1	
Turn left into camp area	17.2	114.3	
Arrive Fletcher Springs / camp	0.3	114.6	
Total since last stop	**19.4**		

DAY 3	Miles from previous turn	Odometer	Description
Camp		0	
From campsite turn right and head towards 4 way intersection		0	
Turn left/west at 4 way intersection	0.6	0.6	
Turn left (south) onto NV 338 towards Bridgeport	15	15.6	Ranch at 2.3 miles was heavily damaged during 9 mile earthquake. Mark Twain stayed here briefly in 1800's
Turn right onto US 395 N	15.2	30.8	enter CA
Drive thru Bridgeport (25 mph) and turn left onto Twin Lakes Road	0.5	31.3	Turn is at Shell station, get expensive gas if you need it.
Arrive stop 1	1.8	33.1	
Total since last stop	**33.1**		
Stop 1		33.1	
Continue on Twin Lakes Road		33.1	
Arrive Stop 2	4.5	37.6	
Total since last stop	**4.5**		

1 DAY 1: Carson to Fletcher Valley

1.1 East Carson Valley Overlook

1.1.1 Introduction

Ian Pierce

Questions to think about during this trip: How do we account for shear without kinematic indicators (piercing points) on low-slip rate lateral faults? How should we deal with seismic hazard in this region if we're "missing slip"? What is off-fault deformation?

Field studies and laboratory models show that as strike-slip systems increase in total displacement, the width of the shear zone decreases, while faults become longer, less complex, more continuous, and more efficient at accommodating strain (Wilcox et al., 1973; Aydin and Nur, 1982; Wesnousky, 1988; An and Sammis, 1996; Stirling et al., 1996; Schreurs, 2003; Faulds et al., 2005; Atmaoui et al., 2006; Zinke et al., 2015; Hatem et al., 2017; Zuza et al., 2017). While many of the transform plate boundaries of the world may be considered mature and capable of producing large earthquakes along well organized fault traces that have accommodated hundreds of kilometers of total slip (e.g., the San Andreas, Altyn Tagh, Sagaing, Denali, or Alpine faults), comparably few immature strike-slip systems have been studied in similar detail (e.g., the Walker Lane, Sicily, the Shan Plateau of Myanmar, or the Shanxi Rift of China). These less well-developed systems have, by this definition, accommodated lesser amounts of total slip, and as a result often lack major through-going faults. Instead these systems form broad regions of faulting and deformation along complex systems of numerous short, discontinuous faults, which are often only capable of producing moderate earthquakes. Studying these complex fault systems in nature offers unique insight into the development of fault systems at a plate boundary scale that can otherwise typically only be understood in a laboratory.
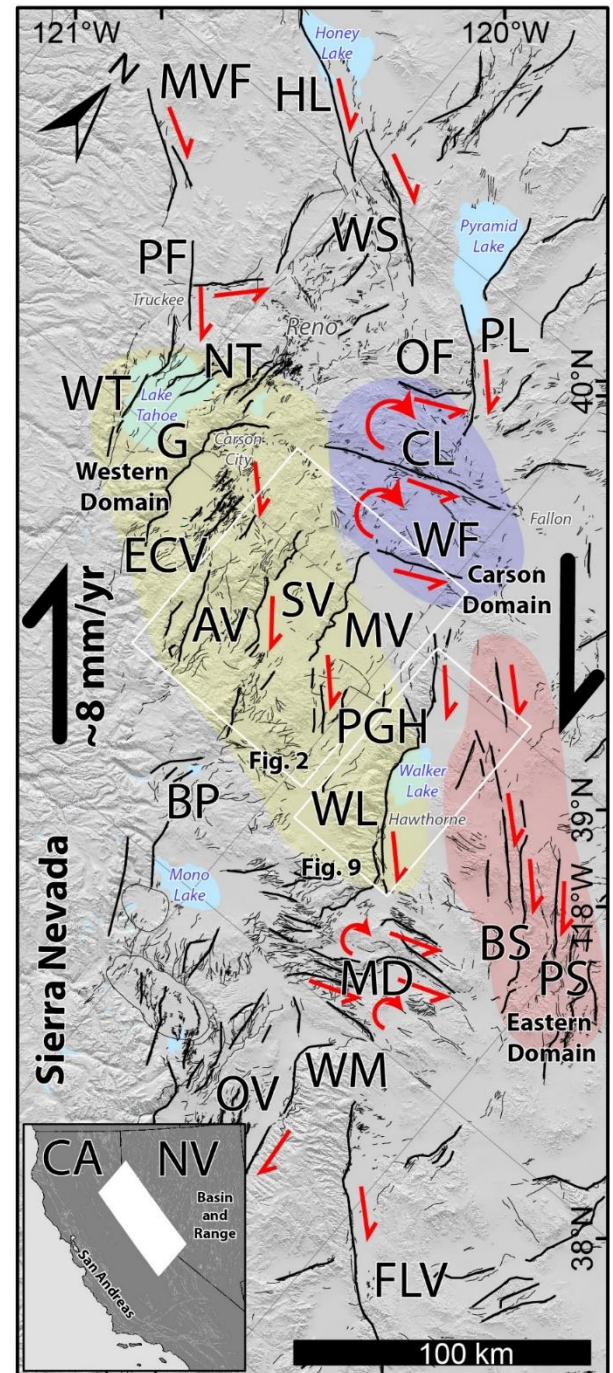

Figure 1 Overview map of Walker Lane. Extent of Figures 2 and 9 are indicated by white boxes. Major faults are thicker while thin faults are from USGS Quaternary fault and fold database. The Central Walker Lane can be divided into the Carson domain (purple), western domain (yellow), and eastern domain (pink). Major faults: MVF-Mohawk Valley, HL-Honey Lake, WS- Warm Springs, PF- Polaris, PL Pyramid Lake, OF-Olinghouse, WT-West Tahoe, NT- North Tahoe (from west to east: Stateline, Incline Village, Little Valley, Washoe Lake), G-Genoa, ECV-East Carson Valley, AV-Antelope Valley, SV-Smith Valley, CL-Carson Lineament, WF-Wabuska, MV-Mason Valley, PGH-Pine Grove Hills, BP-Bridgeport Valley, WL-Walker Lake, BS-Benton Springs, PS-Petrified Springs, MD- Mina Deflection (Rattlesnake, Excelsior, Coaldale), OV-Owens Valley, WM- White Mountains, FLV-Fish Lake Valley.
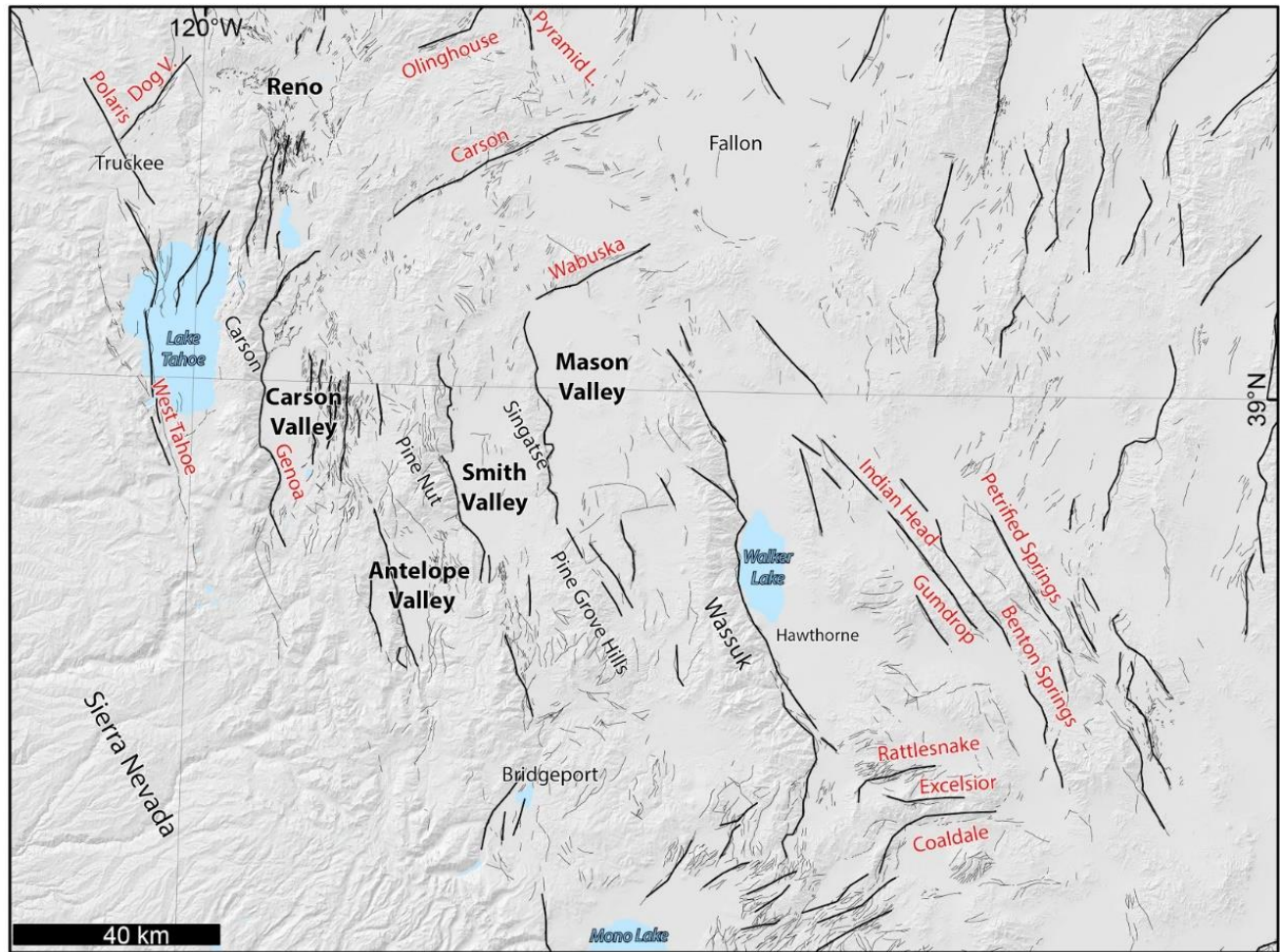
Figure 2: overview of the Central Walker Lane showing major faults and place names.

The Central Walker Lane can be subdivided into three domains (**Figure 1**). The eastern domain or Walker Lake block is composed of the northwest striking dextral strike-slip Benton Springs, Indian Head, Gumdrop, and Petrified Springs faults(Wesnousky, 2005; Angster et al., 2019). The northerly Carson domain (e.g. Cashman and Fontaine, 2000; Wesnousky, 2005; Li et al., 2017) is composed of the transverse, northeast-striking, sinistral Wabuska, Olinghouse (Briggs, 2005), and Carson faults and lineaments. The western domain is composed of the basins and their range-bounding faults that are the focus of this trip, including the Tahoe (Kent et al., 2005; Maloney et al., 2013; Pierce et al., 2017) and Walker Lake (Bormann et al., 2012; Dong et al., 2014; Surpless and Kroeger, 2015) basins, and Carson (Ramelli et al., 1999; dePolo and Sawyer, 2005), Smith (Wesnousky and Caffee, 2011), Mason, and Antelope (Sarmiento et al., 2011) valleys.

The western domain of the Central Walker Lane is defined by a series of subparallel north-striking/east-dipping active range-bounding faults each dividing a mountain range to the west from a half-graben holding a basin to the east. These north-strike of the ranges contrast sharply with the northeast-striking ranges of the Basin and Range to the east of this region, and the continuous high topography of the Sierra Nevada to the west. Most of these range-bounding faults are ~30–45 km long (except for the ~85 km long Wassuk rangefront fault) and form a rough left stepping en-echelon pattern,

with faults spaced ~20–35 km apart from east to west. The westward stratigraphic tilt of these ranges decreases to the northwest from 60° in the Wassuk and Singatse ranges, to <20° in the Carson Range, and <5° in the Sierra Nevada, and likewise the southeasterly Singatse and Wassuk ranges have considerably higher amounts of total extension (>150%) than the ranges to the west (Surpless et al., 2002), which has been cited as evidence of the progressive westward encroachment of faulting into the Sierra Nevada. Thermochronologic data show that many of the mountain ranges in the region have undergone two phases of exhumation: an initial period ~14–15 Ma, and a younger period sometime between 3 and 10 Ma (Surpless et al., 2002). This second phase was initially attributed by Surpless et al. (2002) to be a result of Basin and Range extension, yet this timing coincides with the imitation of the Walker Lane at these latitudes (e.g., Faulds and Henry, 2004), so may be a result of the encroachment of Walker Lane deformation, while the earlier phase may be attributed to Basin and Range extensional faulting (Surpless et al., 2002).
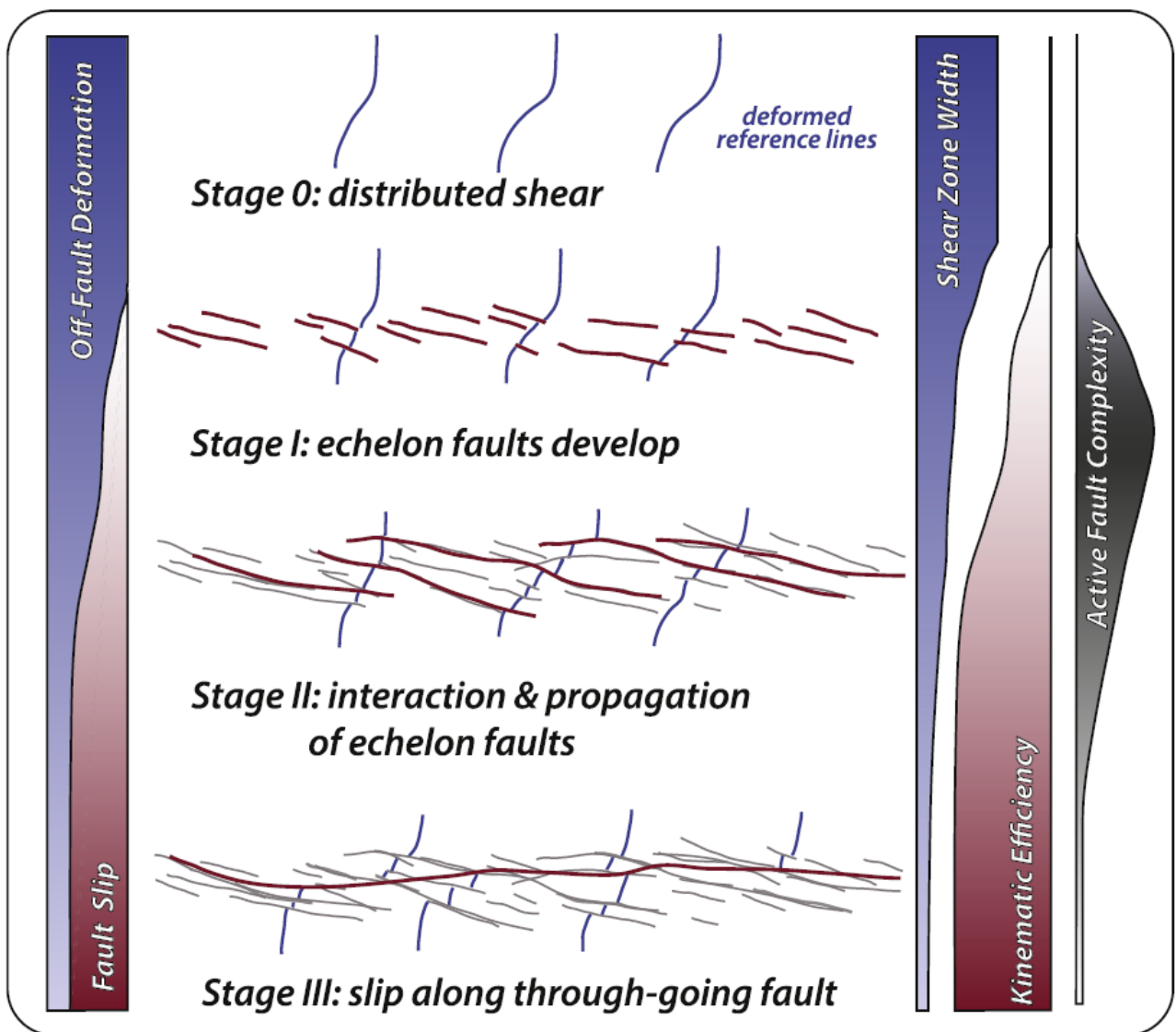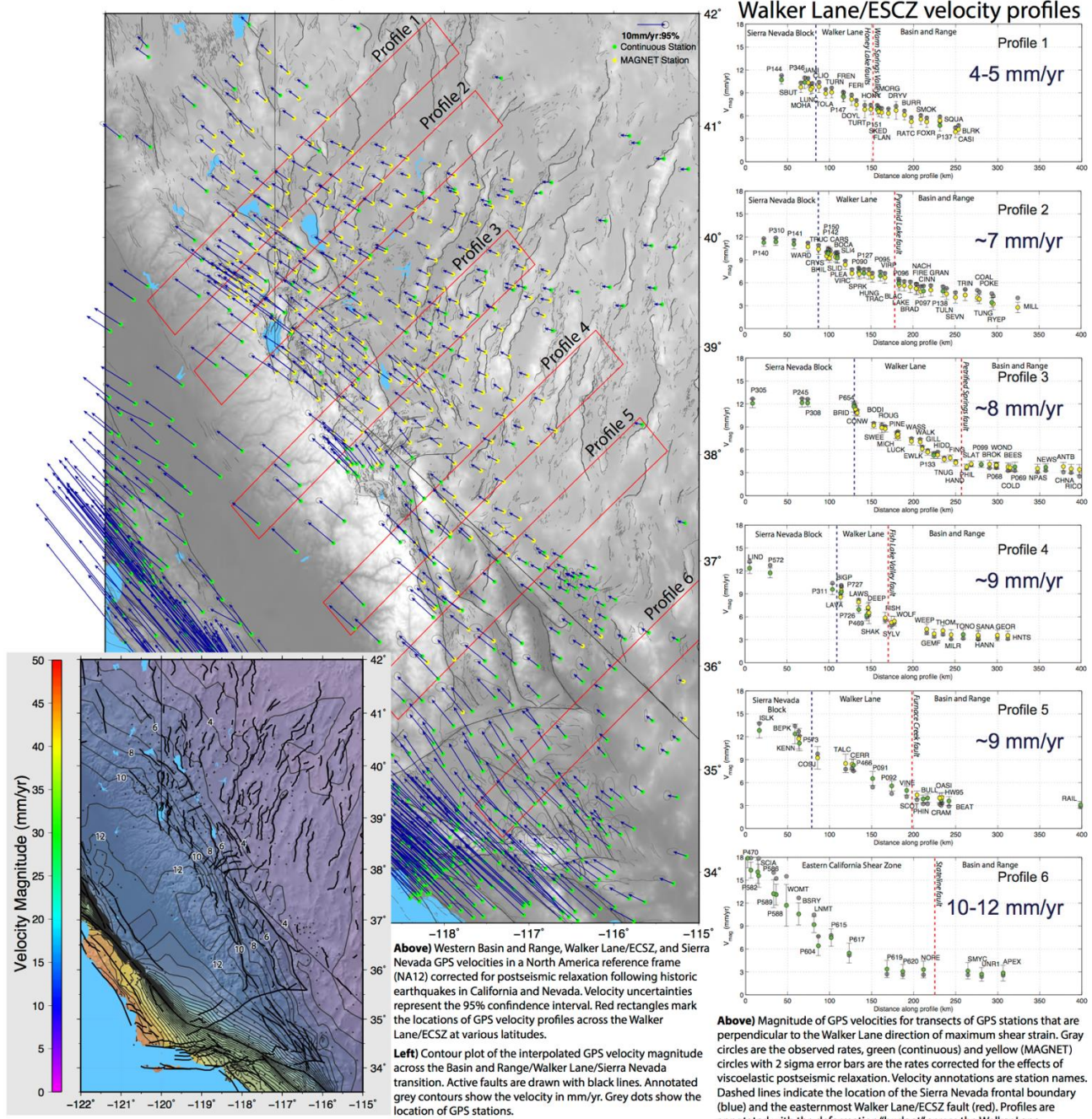

Figure 3: Stages of strike-slip fault growth from experiments in wet clay. Copied from Hatem et al. (2017)

1.1.2 GPS constraints on Central Walker Lane the deformation budget, style of deformation, and fault slip rates

Western Basin and Range GPS Velocities in NA12 North America reference frame

Walker Lane/ESCZ velocity profiles

Above) Western Basin and Range, Walker Lane/ECSZ, and Sierra Nevada GPS velocities in a North America reference frame (NA12) corrected for postseismic relaxation following historic earthquakes in California and Nevada. Velocity uncertainties represent the 95% confidence interval. Red rectangles mark the locations of GPS velocity profiles across the Walker Lane/ECSZ at various latitudes.

Left) Contour plot of the interpolated GPS velocity magnitude across the Basin and Range/Walker Lane/Sierra Nevada transition. Active faults are drawn with black lines. Annotated grey contours show the velocity in mm/yr. Grey dots show the location of GPS stations.

Above) Magnitude of GPS velocities for transects of GPS stations that are perpendicular to the Walker Lane direction of maximum shear strain. Gray circles are the observed rates, green (continuous) and yellow (MAGNET) circles with 2 sigma error bars are the rates corrected for the effects of viscoelastic postseismic relaxation. Velocity annotations are station names. Dashed lines indicate the location of the Sierra Nevada frontal boundary (blue) and the easternmost Walker Lane/ECSZ fault (red). Profiles are annotated with the deformation "budget" across the Walker Lane.

- The velocity data establish that the GPS observed relative right-lateral deformation is greatest across the zone of active faulting that defines the Walker Lane.

- The deformation "budget" across the Walker Lane faults decreases northward, from 10-12 mm/yr in the Eastern California Shear Zone to 4-5 mm/yr in the northernmost Walker Lane.

- The contour map and velocity profiles show that width of the geodetically observed shear zone increases to >200 km at its northernmost extent. The shear zone extends into the western Basin and Range, which is typically considered to be an extensional domain and is characterized by normal faulting.

Figures from: Bormann, J.M., W.C. Hammond, C. Kreemer, G. Blewitt, and S. Jha, 2013, A Synoptic Model of Fault Slip Rates in the Eastern California Shear Zone and Walker Lane from GPS Velocities for Seismic Hazard Studies, 2013 SSA Meeting, Salt Lake City, UT, April 17-19, 84(2), p. 323.

Figure 2. GPS velocities from daily position time series
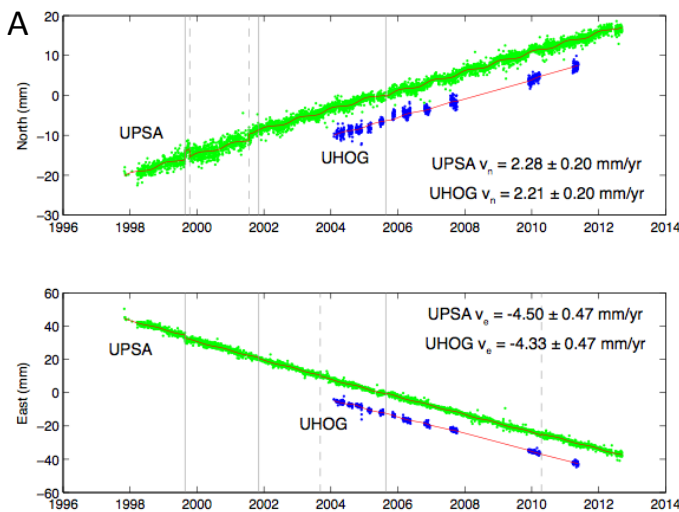
A) Comparison of daily position time-series and velocities derived from co-located continuous and semi-continuous GPS stations. **B)** Example of a deep-braced continuous GPS station. **C)** Example of a MAGNET semi-continuous GPS station.

Possible mechanisms for CWL shear accommodation (Wesnousky et al, 2012):

1) Oblique slip on basin bounding normal faults
   - Suggestions of oblique slip reported on the Antelope Valley and Wassuk Range normal faults (Sarmiento et al., *2011*; Wesnousky, *2005*)

2) Slip partitioning with extension on basin bounding normal faults and shear distributed through valley floors.
   - as seen in Owen's Valley
   - 1932 Cedar Mountain earthquake (Bell et al., *1999*)

3) Combination of normal faulting and block rotation
   (e.g. Garfunkel and Ron, *1985*; Ron and Nur, *1996*)

Figure from Bacon and Pezzopane (*2007*)

Ductile (top) and brittle (bottom) wax models of right lateral transtensional shear.
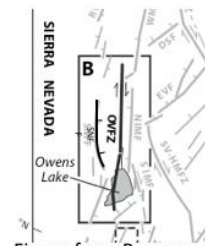
Model courtesy of Jim Brune

Citation: Wesnousky, S., J.M. Bormann, C. Kreemer, W.C. Hammond, J. Brune, 2012, Neotectonics, Geodesy, and Seismic Hazard in the Northern Walker Lane of Western North America: Thirty Kilometers of Crustal Shear and No Strike-Slip?, *Earth and Planetary Science Letters*, v. 329-330, doi:10.1016/j.epsl.2012.02.018.

Accommodation of missing shear strain in the Central Walker Lane, western North America: Constraints from dense GPS measurements

Jayne M. Bormann, William C. Hammond, Corné Kreemer, and Geoffrey Blewitt

Abstract: We present 264 new interseismic GPS velocities from the Mobile Array of GPS for Nevada Transtension (MAGNET) and continuous GPS networks that measure Pacific-North American plate boundary deformation in the Central Walker Lane (CWL). Relative to a North America-fixed reference frame, northwestward velocities increase smoothly from ~4 mm/yr in the Basin and Range province to 12.2 mm/yr in the central Sierra Nevada resulting in a CWL deformation budget of ~8 mm/yr. We use an elastic block model to estimate fault slip and block rotation rates and patterns of deformation from the GPS velocities. Right-lateral shear is distributed throughout the CWL with strike-slip rates generally <1.5 mm/yr predicted by the block model, but extension rates are highest near north-striking normal faults found along the Sierra Nevada frontal fault system and in a left-stepping, en-echelon series of asymmetric basins that extend from Walker Lake to Lake Tahoe. Neotectonic studies in the western CWL find little evidence of strike-slip or oblique faulting in the asymmetric basins, prompting the suggestion that dextral deformation in this region is accommodated through clockwise block rotations. We test this hypothesis and show that a model relying solely on the combination of clockwise block rotations and normal faulting to accommodate dextral transtensional strain accumulation systematically misfits the GPS data in comparison with our preferred model. This suggests that some component of oblique or partitioned right-lateral fault slip is needed to accommodate shear in the asymmetric basins of the western CWL. Present-day clockwise vertical axis rotation rates in the Bodie Hills, Carson Domain, and Mina Deflection are between 1-4°/Myr, lower than published paleomagnetic rotation rates, suggesting that block rotation rates have decreased since the Late to Middle Miocene.
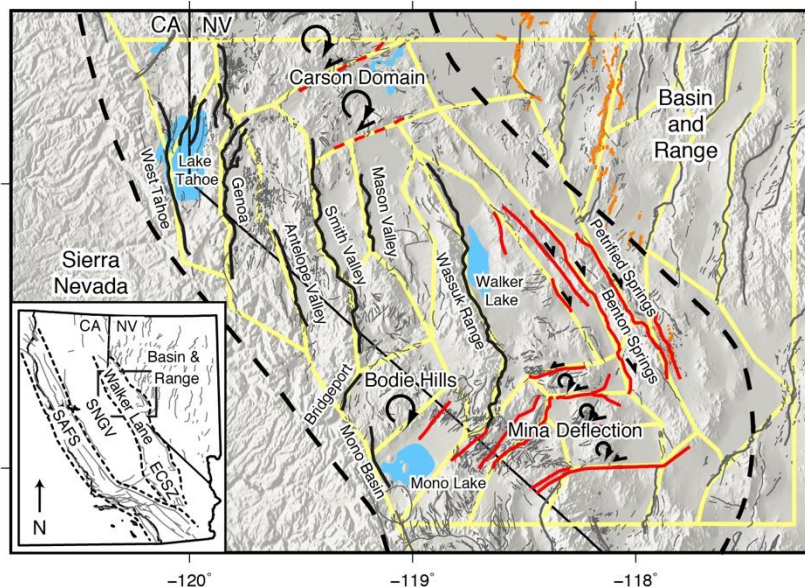
Figure 1: Regional map showing the block model boundaries (yellow lines) in relation to the topography and faults of the CWL. The CWL (region within the dashed black lines) lies between the northeast striking normal faults of the Basin and Range and the Sierra Nevada microplate. Black lines delineate CWL major normal faults, and red lines delineate strike slip faults. Paleomagnetic observations indicate that crustal blocks in the Carson Domain, Bodie Hills, and Mina deflection accommodate dextral shear through clockwise vertical axis rotations [*Cashman and Fontaine*, 2000; *Petronis et al*, 2009; *Rood et al.*, 2011]. Orange lines mark Central Nevada Seismic Belt historic ruptures. Faults traces modified from the USGS Quaternary Fault and Fold database [*U.S. Geological Survey, California Geological Survey, and Nevada Bureau of Mines and Geology,* 2006]. Inset map shows the location of the study area in relation to other elements of the Pacific/North America Plate boundary zone.

Figure 2: Interseismic GPS velocities in the NA12 North America reference frame. (Top) GPS velocities across the Basin and Range, Central Walker Lane, and Sierra Nevada transition. Velocity magnitude is indicated by the length and color of the arrows. Dashed box marks the location of the velocity profile shown below. Selected GPS sites within the profile are labeled with the site names. (Bottom) Magnitude of the GPS velocity for a 50-km-wide transect of sites that is perpendicular to the trend of the Central Walker Lane. Gray circles are the observed rates, and the yellow (MAGNET stations) and green (continuous stations) circles with 2 sigma error bars are the interseismic rates corrected for the effects of viscoelastic postseismic relaxation following historic earthquakes in the Central Nevada Seismic Belt [*Hammond et al.*, 2009]. Blue dashed lines indicate eastern and western bounds of Walker Lane.
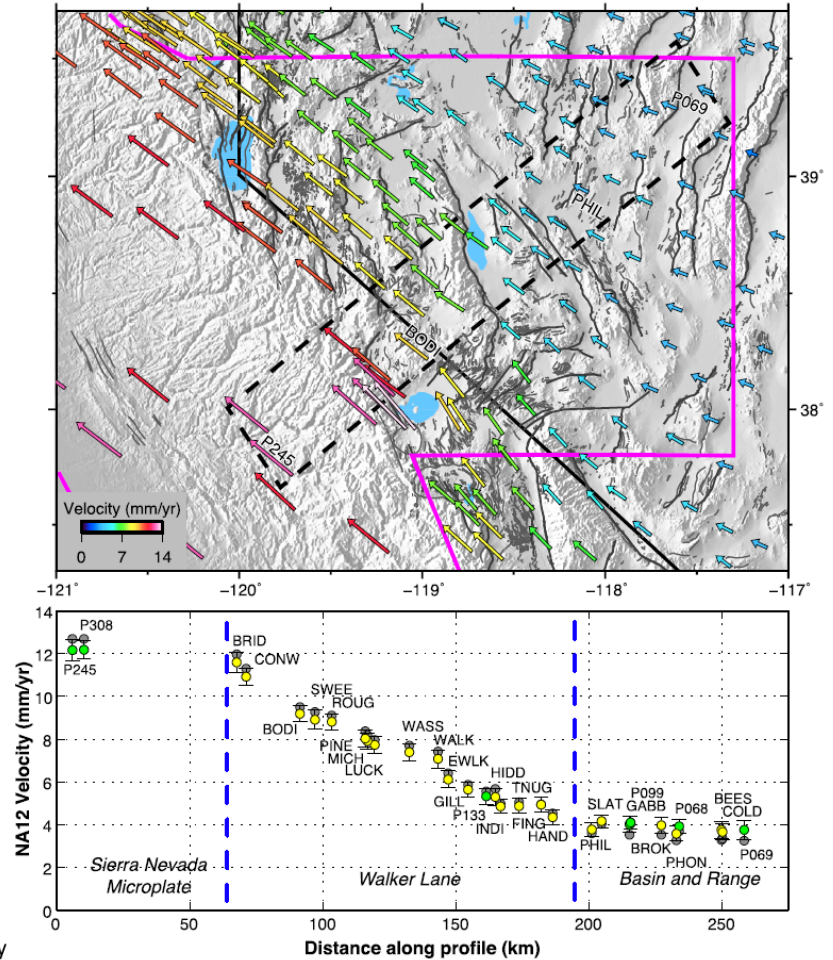
Elastic Block Models:

Goal: Estimate slip rates on faults over a geologically significant period of time

"Long Term" Velocity = Interseismic + Coseismic Velocity

$$\vec{v}_{LT} = \vec{v}_{Int} + \vec{v}_{Cos}$$

$$\vec{v}_{Int} = \vec{v}_{LT} - \vec{v}_{Cos}$$

Assumptions:

1) Velocity data are representative of interseismic motion
2) The crust is composed of distinct elastic blocks bounded by faults.
3) Faults are locked at surface and slipping at depth
4) Block geometries must be right, i.e. interiors are rigid over 'long-term' and deformation on faults occurs during earthquakes

after Savage and Burford (1973), modified from Meade and Hagar (2005) and Segall (2010)
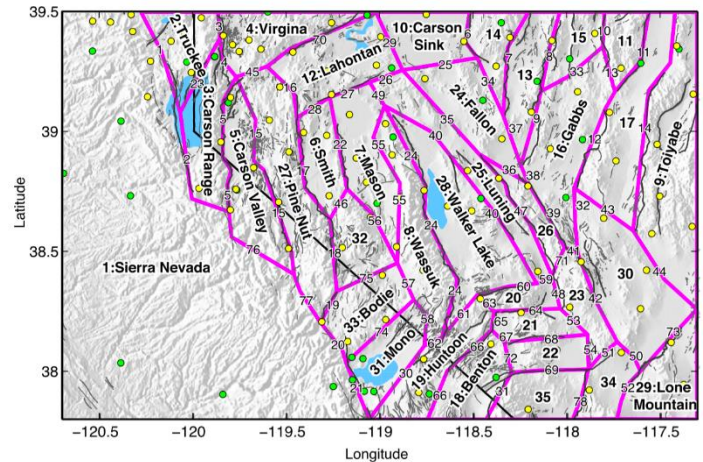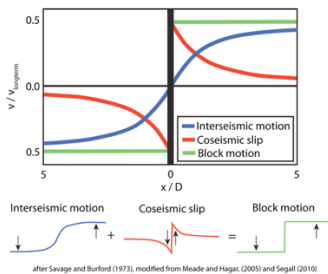
Figure 3: Block boundaries used for the deformation analysis with block name and fault train legend. Magenta lines illustrate block model geometry with faults, topography, and GPS station locations. Yellow circles represent MAGNET stations, and green circles represent continuous stations.
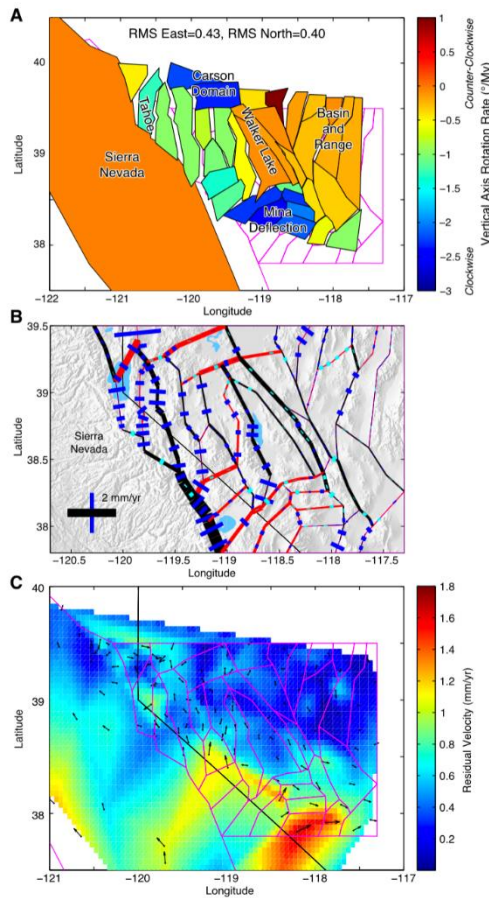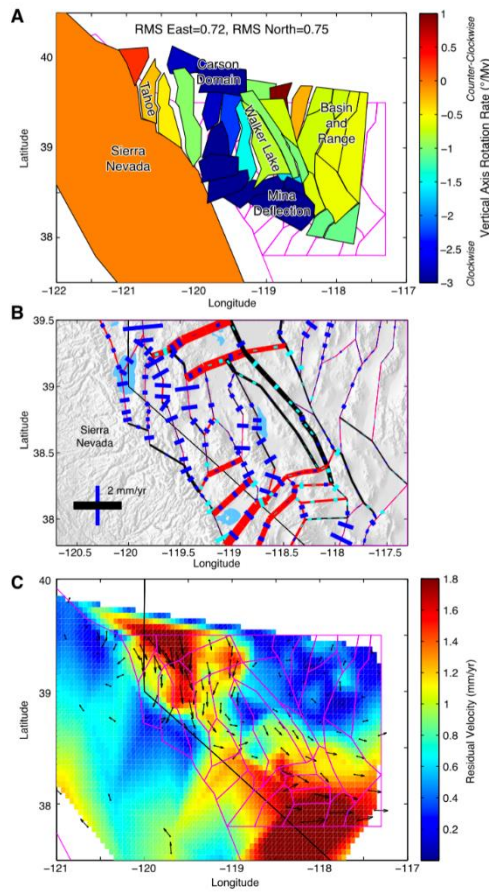
Figure 4   **Figure 5**

Figure 4: Block motions, slip rates, and velocity residuals for the best fitting GPS model. (A) Rigid block rotation and translation exaggerated by a factor of 10^7 (representing 10 million years of deformation). Color of block indicates vertical axis rotation rate. (B) Predicted fault slip rates represented by the thickness of black (red) line for dextral (sinistral) strike-slip motion and the length of blue (cyan) bar for fault normal extension (compression). (C) Residual GPS velocities (black arrows) after subtracting the model predictions. The colored surface represents an interpolation of the residual magnitude, with warm colors indicating the regions of greatest misfit. **Figure 5:** Same as Fig. 4, except that the model is constrained to be consistent with the geologic observations that preclude oblique dextral slip on Central Walker Lane normal faults.

Table 2

Geologic and geodetic estimates of fault slip rates for the en-echelon, normal fault-bounded basins.

Fault[a]	Basin	Block model fault train[b]	Geologic horizontal extension rate (mm/yr)[c]	GPS fault perpendicular extension (mm/yr)[d]	GPS fault parallel shear (mm/yr)[d,e]	Block model horizontal extension rate (mm/yr)	Block model strike-slip rate (mm/yr)[e]
West Tahoe		2				0.5 ± 0.4	0.2 ± 0.4
Stateline Incline Village	Tahoe	23	0.5–1.7	0.6–0.8	0.5–0.7	0.6 ± 0.5	**1.6** ± 0.5
Genoa Central	Carson	5	0.7–1.7	1.0–1.3	~0.1	0.6 ± 0.5	**0.2** ± 0.5
Genoa South	Carson		0.1–0.5	0.6–0.9	~0.3		
Smith Valley	Smith	17	0.1–0.3	0.7–1.2	1.0–1.2	0.4 ± 0.5	0.5 ± 0.4
Singatse Range	Mason	22	0.2–0.3	0.7–0.9	**0.1**–0.2	0.6 ± 0.5	0.4 ± 0.4
Antelope Valley	Antelope	15	0.35	0.9–1.1	0.6–1.1	0.7 ± 0.5	1.1 ± 0.4
Robinson Creek	Bridgeport	19	0.1–0.3	~0.2	0.0–**0.1**	$1.2 + 0.5$	**1.3** ± 0.6
Wassuk Central	Walker Central	24	0.5–0.8	0.4–0.7	1.2–1.6	0.6 ± 0.4	0.7 ± 0.3
Wassuk North[f,g]	Walker North		0.5–1.3	0.9–1.0	0.7–1.3		

[a] Geologic fault slip rates from Wesnousky et al. (2012) and references therein, with the exception of recently published rates for the northern Wassuk Range fault zone.
[b] See Fig. 5 for fault train legend.
[c] Rates calculated in Wesnousky et al. (2012) and this study (Wassuk North site) from originally reported vertical and dip-slip rates by assuming a fault dip of 45–60°.
[d] Rates calculated by Wesnousky et al. (2012).
[e] Bold slip rates indicate left-lateral motion.
[f] Dong et al. (2014).
[g] Surpless and Kroeger (2015).

1.1.3   The Eastern Carson Valley Fault System

Craig M dePolo, Nevada Bureau of Mines and Geology

The Eastern Carson Valley fault system (**ECVFS**, fig. 1) is a prominent set of Quaternary faults extending 21 to 26 km in length in eastern Carson Valley. The system is made up of over 200 fault traces and is 8-10 km wide, about a third of the width of the valley. The ECVFS is a complex zone of subparallel, anastomosing, nested, and generally east-dipping faults (although there are some west-dipping faults). Individual faults are commonly 1 to 2 km long, but some are as much as 4 km long. Cross-strike distances between the fault traces are commonly 50 to 300 m, and as much as 1 km. The fault system has normal dip-slip displacement and probable right-lateral strike-slip movement as well (oblique slip or bi-slip – alternating preference).

During the summer of 1988 John Bell of NBMG was informed that a fault within the ECVFS (the Fish Springs Flat fault zone) had a 1-km-long crack along it (fig. 2). Upon inspection it was observed that the crack was along what looked to be the youngest rupture on a compound fault scarp (an inflection in the scarp slope). The crack was 0.6- to 4.5-cm wide. The northern 2/3rds was northerly striking whereas the southern third had a NNW strike. The indicated extension direction across the crack was 90° to 101°. John Bell trenched the crack and found it was directly connected to the fault forming the scarp (fig. 2), found openings as wide as 3 cm along the fault and splay faults, found evidence of prior cracks, and found evidence of discrete displacement deposits, including the most recent event. We could not detect progressive slip with time on the crack, although one of our paint stripes across the fault showed 1-2 cm of right slip in March 1989. Three main hypotheses were entertained at the time for the 1-km-long crack: 1) the crack was related to a small earthquake, 2) the crack was related to local groundwater withdrawal, or 3) the crack was related to aseismic movement of the fault. A seismometer from the Nevada Seismological Laboratory was located in Buffalo Canyon at the south end of the ECVFS. We were able to examine helicorder records from this station for a month prior to the report of the cracking (discovered by local residents shortly after it formed) and there were no local earthquakes that could be related to the crack (see also fig. 2). Don Helm, a hydrologist for the NBMG, modeled the hydrology of Fish Springs Flat and noted that groundwater levels had been constant over five years prior to the crack formation – thus, a hydrologic origin seemed unlikely. That left the aseismic movement hypothesis for the formation of the crack. Sympathetic cracking occurred in 1994 along this fault as well. The fault appears to have two modes of displacement, minor aseismic slip and larger offsets likely formed during earthquakes.

There are two main geomorphic expressions of paleoseismic activity along the ECVFS: young scarps and inflection on hillslopes, and tectonically offset stream terraces. The youngest rupture showed up distinctly on low-sun-angle photography taken by Dr. Burt Slemmons (University of Nevada, Reno) and was visible to us in Fish Springs Flat when we studied the aseismic crack. Using the fault map created by dePolo and others (2000), Alan Ramelli and I mapped out the extent of the youngest rupture (fig. 1). Although there is a central rupture in the middle, there are numerous young breaks off to the sides that also appear to be young ruptures and they all appear to all be about the same age. Young ruptures were also discovered just south of Hot Springs Mountain. The age of these ruptures can be constrained by radiocarbon dates to be between 302-921 cal YBP (2 sigma), but the event(s?) were likely around 450 to 750 years ago.

Tom Sawyer and I had three trenches excavated in the area of tectonically offset stream channels, one on each terrace (fig. 5). We chose this location because of the strong geomorphic expression of paleoearthquakes, but also because this was a first order fault in the system (Fish Springs Flat fault zone) and the site included the youngest rupture. The fault zone was clearly exposed in all three trenches and the geologic units were distinct.

Figure 1. East Carson Valley fault system (ECVFS) and other faults mapped in the Carson Valley area. Orange faults have moved in the last 15 ka, yellow in the last 130 ka, and green and blue are earlier Quaternary. Note the younger rupture crossing through the ECVFS. Also indicated are STOP 1, the location of the aseismic cracks, the location of the trenches, and the location of the 1994 Double Spring Flat earthquake (Mw 5.8) cracks. Hot Springs Mountain is immediately north of the "J" in Johnson Lane.

Trench 1 (fig. 3, 5) exposed a fault zone that offset alluvium vertically by 82 to 90 cm. The faults all strike N10°E, which is 5° more easterly than the fault scarp; this indicates the faults were in a left-stepping echelon pattern, suggestive of a strike-slip component. **Trench 2** (fig. 4) was across a 2-m-high fault scarp in the face of the second highest stream terrace remnant, about 30 m south of Trench 1 (fig. 5). The scarp trends N15°E. Trench 2 exposed a 3-m-thick stack of colluvial, alluvial, and fluvial deposits in the hanging wall, and mostly Plio-Pleistocene alluvium in the footwall. A 17-m-wide fault zone was exposed in Trench 2. The main fault between the Plio-Pleistocene sediments and the colluvium has a N15°E strike, the same orientation as the fault scarp. The zone has an anastomosing character and dips 88° to the west. Within about 4 m of the main fault, faults are parallel to the scarp as well. In contrast, most faults that are greater than 4 m away from the main fault have 15° to 20° more easterly strikes, consistent with a left-stepping, wrenching pattern of faulting. **Trench 3** (fig. 6) was 50 m south of Trench 2 (fig. 5) and exposed stratigraphy that was similar. The excavation was across a large 6-m-high compound fault scarp in the highest terrace remnant. Fourteen different units were identified in Trench 3. The trench exposed a 25-m-wide zone of faulting. Most are simple faults with limited offset, and all have more easterly strikes than the main fault. There is evidence for at least three paleoearthquakes in Trenches 2 and 3, and the possibility additional events that have weaker evidence. Paleoearthquakes 1, 2, and 3 are all evidenced by colluvial deposits induced by scarp formation. Paleoearthquake 4(?) also seems likely with probable colluvial deposit and fissure fill. Only the most recent event could be confidently dated at the trench site using bulk radiocarbon dating; it occurred between 520 and 921 cal ybp.
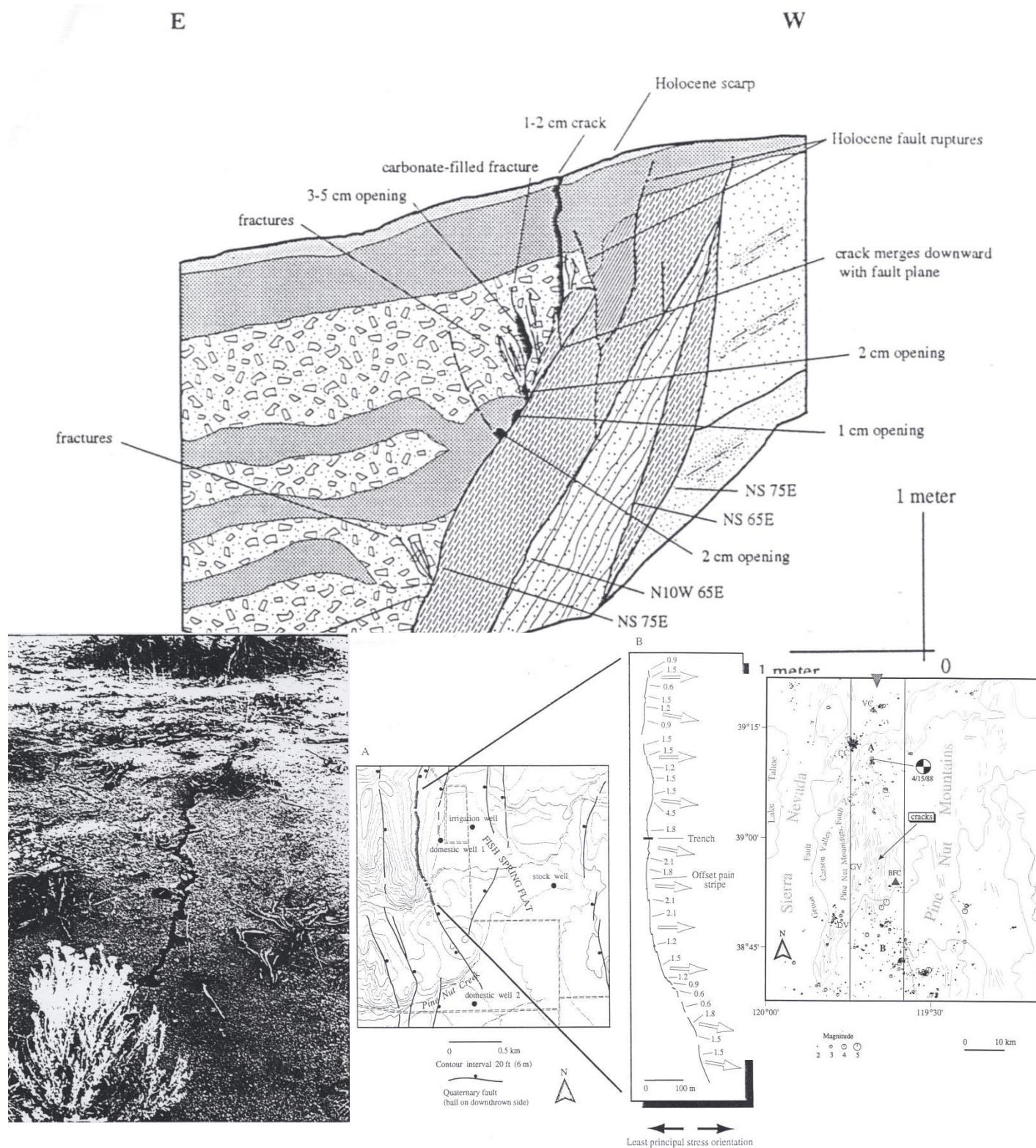
Figure 2. All figures are from John Bell and others (1993, unpublished; Aseismic slip on an extensional. BRP fault: evidence for tectonic creep). Above is the cross-crack trench. Lower left is photo of crack. Lower middle are extension directions. Lower right is local seismicity, 1983-1992.
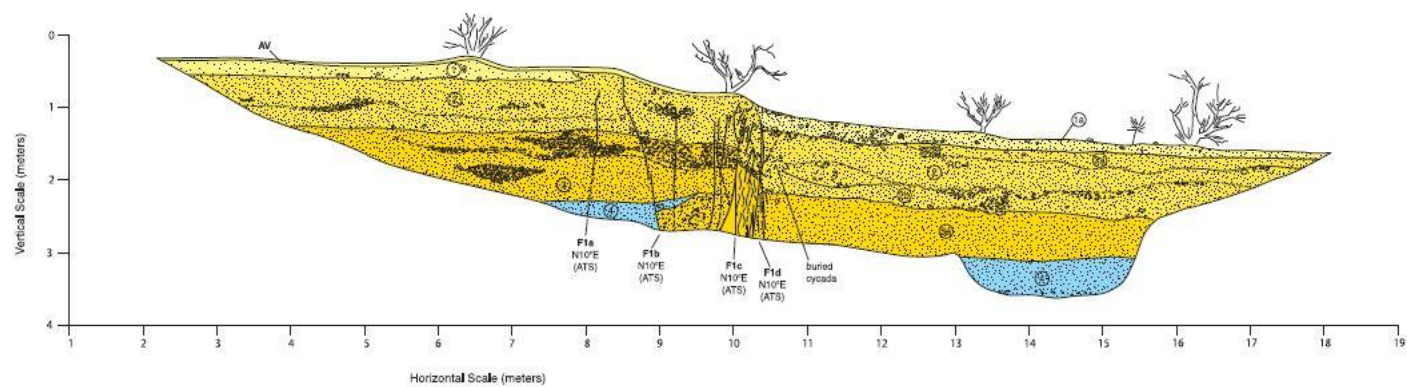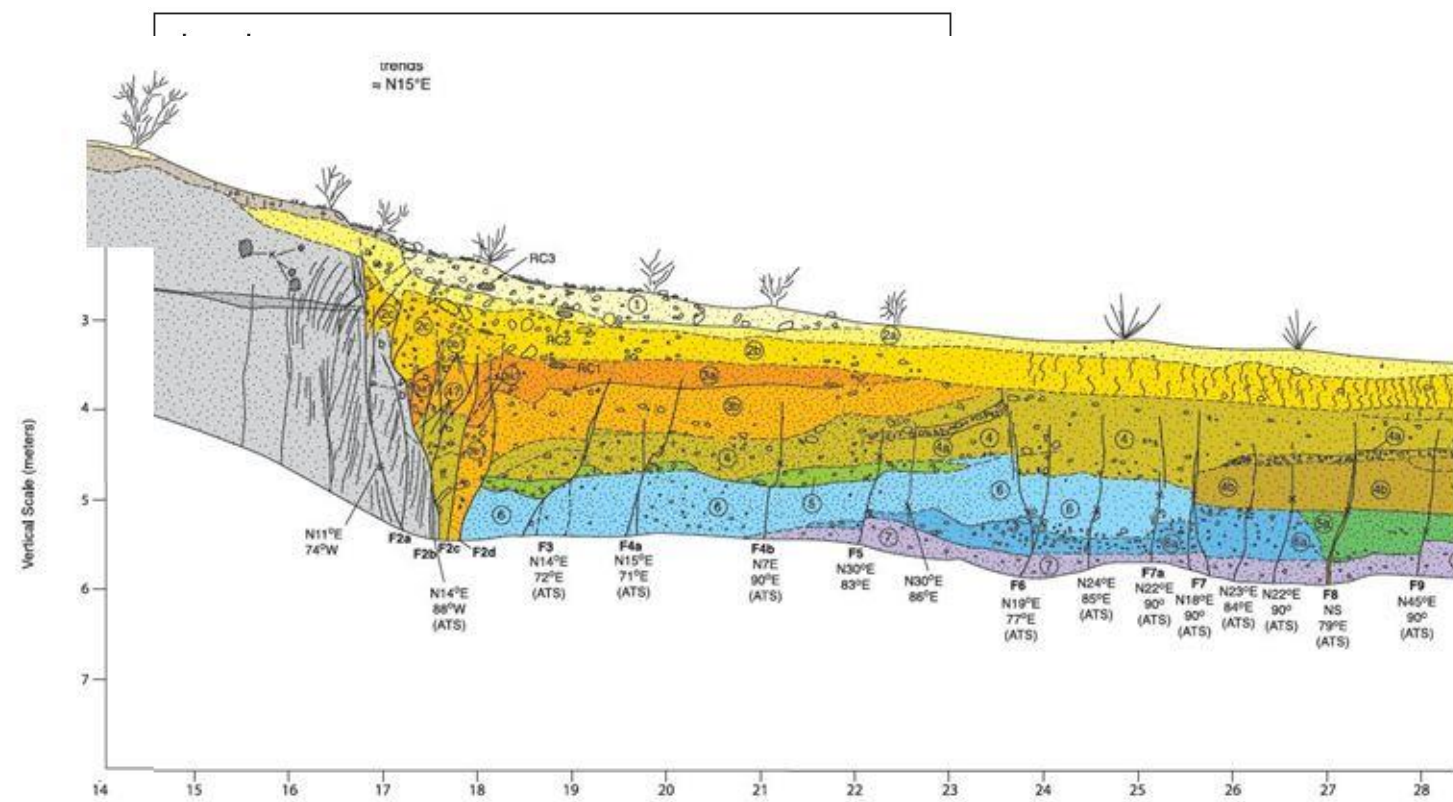
Figure 3. Trench 1. dePolo and Sawyer (2005)

Figure 4. Partial log of Trench 2. dePolo and Sawyer (2005).

Figure 5. Trench location map

Figure made by Tom Sawyer with robotic total station and mountain bike.
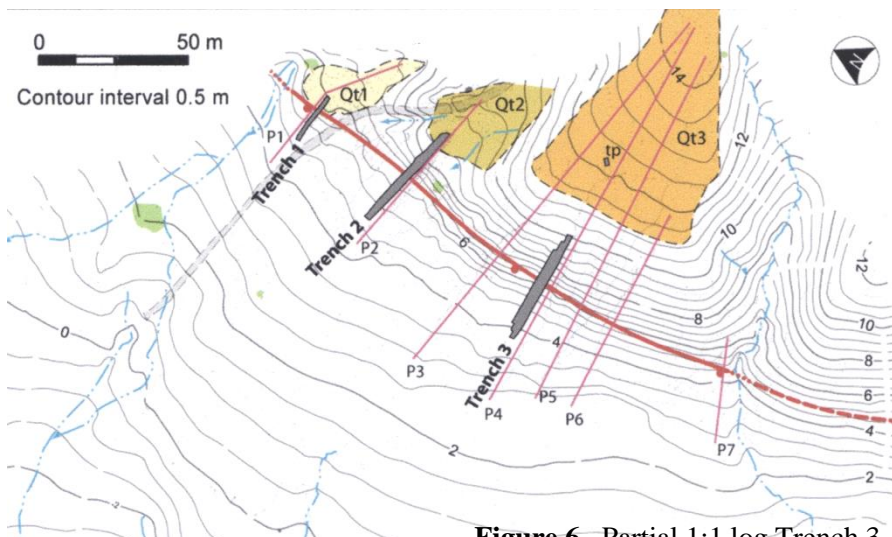
Figure 6. Partial 1:1 log Trench 3. dePolo and Sawyer (2005) Paleoseis studies ECVFS, USGS NEHRP FTR.
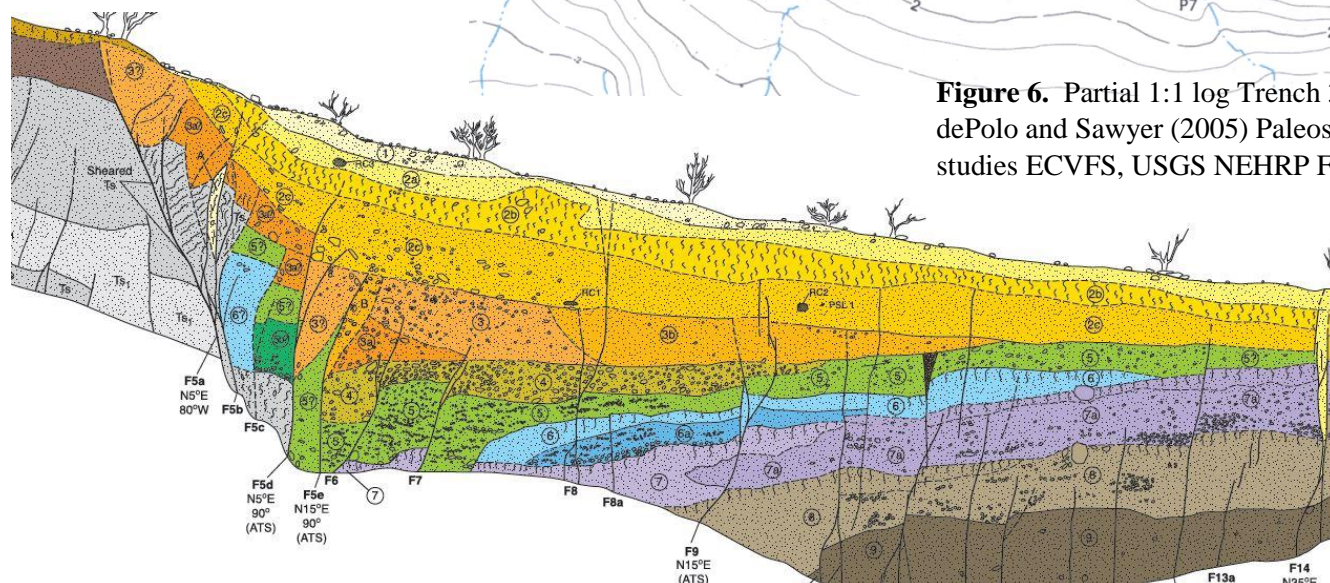
Legend

① Gravelly, silty, coarse to fine sand colluvium	⑧ Gravelly coarse to fine sand colluvial and alluvial
② Gravelly, clayey medium to fine sand and pebbly sandy clay colluvium	⑨ Gravelly coarse to fine sandy colluvium and alluvium
③ Gravelly coarse to fine sand colluvium	⑩ Gravelly sandy clayey argillic horizon
④ Gravelly fine sandy alluvium	⑪ Gravelly coarse to medium sandy colluvium
⑤ Gravelly medium to coarse sand alluvium	⑫ Gravelly fine sand alluvium
⑥ Fine to very fine sand with pebble gravel lenses - alluvium	⑬ Gravelly coarse to medium sand alluvium
⑦ Clayey fine to very fine sand with pebble gravel lenses - alluvium and colluvium	Ts Tertiary medium to fine sand and very fine sand with minor pebble stringers

1.2 Artesia Fan

1.2.1   Overview of Smith Valley

Ian Pierce

Smith Valley is a half-graben with a NNW-striking active rangefront fault bounding the Pine Nut Range to the west. The half graben is ~50-km-long, and 15-km-across at its widest. The total vertical relief from the valley floor to the crest of the Pine Nut Range is over 1400 m. The West Fork of the Walker River enters Smith Valley through a narrow canyon near the town of Wellington. It bends northeastward here and meanders across the basin through a canyon of increasing depth before it exits the valley on the eastern side, cutting through the Singatse Range. This canyon is cut into lacustrine and fluvial deposits, likely deposited by Pluvial Lake Wellington, which reached a highstand of 1477 m above sea level (asl) between 60 and 80 ka (Stauffer, 2003; Wesnousky and Caffee, 2011). In the central part of the basin, just north of the Walker River, there are a pair of left-stepping, north striking, en-echelon fault strands that form 1–2-m-high scarps in stabilized aeolian/dune deposits. The faults do not cut any of the younger floodplain deposits closer to Walker River. Artesia Lake, a small playa remnant of pluvial Lake Wellington (Stauffer, 2003), is present in the northern part of Smith Valley, and is hydrologically isolated from the Walker River.

The range bounding fault in Smith Valley forms an abrupt rangefront with triangular facets, scarps in young alluvial fans, and uplifted alluvial terraces. The rangefront fault generally strikes northwest and makes several northeast-striking right steps separating otherwise long, northwest striking linear sections. When the strike of the fault changes from north-northwest to northeast within these right-steps, both the frequency of scarps and their heights increase dramatically from less frequent ~6–8-m-high scarps in the linear NNW sections to >20-m-scarps along the largest of these northeast striking step overs near the Artesia Fan. The fault primarily exhibits down to the east/southeast vertical displacement, and nowhere did we observe laterally displaced stream channels recording right-lateral strike-slip motion. The faulting in the southernmost portion of the basin near the Wellington Hills forms a horsetail splay of numerous large (~5–10-m-high) scarps. These scarps are generally sub-parallel to the northward drainage of the basin in this area and thus may be modified by fluvial processes. The northern portion of Smith Valley is occupied by the Buckskin Range, which is bounded by an active fault on its east flanks. This fault forms a fairly continuous north-northeast striking scarp in young, intermediate, and older alluvial fan deposits. To the west of the Buckskin Range, there is a continuation of the Smith Valley rangefront fault, and here we observe frequent grabens, en-echelon fault scarps, and vertically displaced Holocene Qy alluvial deposits.
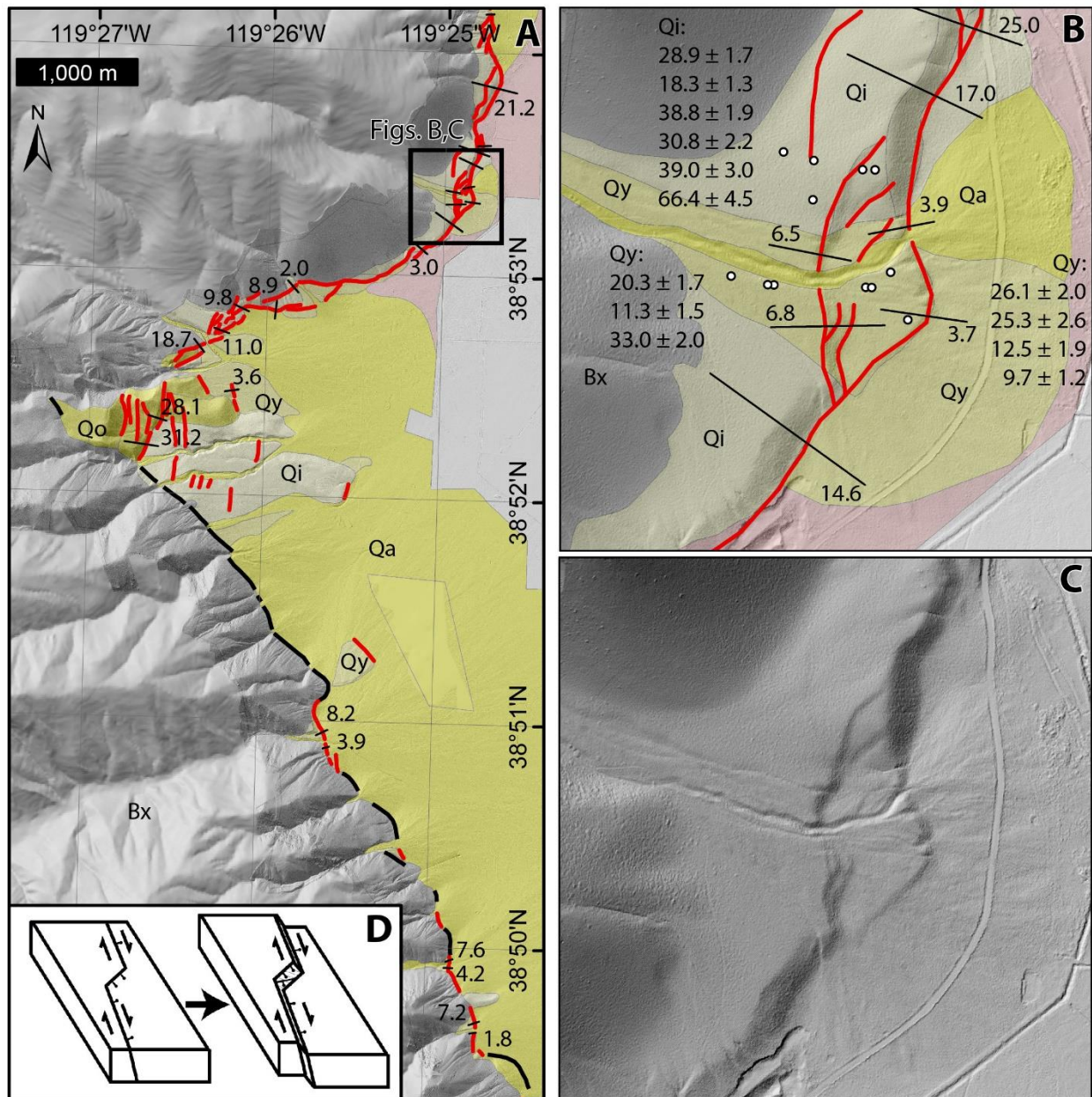
Figure 1 Section of Smith Valley rangefront showing geometry of large right step (a) and location of Artesia fan slip rate site (b, c). Black faults are bedrock-alluvial fault contacts, while red faults are fault scarps in alluvial deposits. Values in (a) are scarp heights (in m). Artesia fan rate site interpreted (b) and bare lidar hillshade (c). Scarp profiles, heights (in m), and ages (ka) of boulder samples (white dots) are shown in (b). (d) Simplified block diagram of a right-bend in a right-lateral oblique fault system provided to explain relatively larger vertical displacements in the step.

1.2.2   Artesia Fan slip rate site

At the eastern edge of a ~1.4-km-long right-step over in the north-northwest striking rangefront fault **(Figure 1)**, older fan surfaces exhibit progressively larger vertical scarps than younger surfaces. Three alluvial fan surfaces are mapped in **Figure 1b:** Qa are the active alluvial fan deposits, forming a narrow active channel cut into young Qy deposits, and on the basin floor form a small fan overtopping Qy deposits. These Qy deposits form an alluvial fan on the hanging wall of the fault as well as on the margins of the main Qa channel on the footwall, and are composed of light gray, rounded, unweathered granitic boulders in a poorly-sorted matrix. Intermediate Qi deposits are only found on the footwall of the fault and are redder in color, with a smoother, less bouldery surface than Qy. The fault has an anastomosing pattern in **Figure 5b** that, from south to north, starts as a single strand, splits into two, then three strands, before coalescing into a single strand again. A maximum age of the Qi fan here is constrained by a 60–80 ka tephra exposed in a road cut in the fault scarp (Stauffer, 2003; Wesnousky and Caffee, 2011). We collected 10 boulder samples for ^{10}Be analysis on the Qi and Qy displaced alluvial fan units and combined these with 3 recalculated ^{10}Be boulder ages at this site from Wesnousky and Caffee (2011) (**Figure 1b**). Six boulder samples were collected from the footwall of the intermediate unit (Qi, **Figure 1b**), and range in age from 18 to 66 ka (mean age of 37.0 ± 16.3 ka), and seven samples from both the hanging and footwalls of a younger aged alluvial fan unit (Qy, **Figure 1b**) range in age from 10 to 33 ka (mean age of 19.7 ± 8.9 ka). While these ages are scattered, the mean ages of the young surface are roughly half of that from the intermediate surface. The average of four profiles measured from the available lidar data (**Figure 5**) show that scarp height in the single strand that cuts the intermediate unit is 19.5 ± 4.5 m, while two profiles of each of the two scarps in the younger unit measure 3.8 ± 0.1 and 6.6 ± 0.2 m, respectively, or 10.5 ± 0.1 m combined (**Figure 2**). Dividing these scarp heights by the ages of the boulder samples from each surface leads to a vertical separation rate of 0.6 $^{+0.8}$/$_{-0.2}$ mm/yr for the intermediate surface and 0.5 $^{+0.7}$/$_{-0.2}$ mm/yr for the young surface **(Figure 2)**. The two rates over different timescales generally agree.

Both the linearity and strike of the long northwest striking segments of the rangefront in Smith Valley suggest that a component of strike-slip is accommodated along the rangefront fault. The Artesia fan is located on the edge of the largest right-step in the Smith Valley rangefront, where scarps are both more frequent and larger than elsewhere along the rangefront (**Figure 1**), and the strike in this step is nearly perpendicular to the primary northwest strike of the rangefront. In a right-lateral fault system, right-steps produce extension parallel to the trace of the right-lateral fault (**Figure 1d**). The vertical displacement at the Artesia Fan is attributed to the kinematics of a right-step in a northwest striking fault with a large component of right-lateral strike-slip. For an obliquely slipping rangefront like Smith Valley, a low rate of lateral-slip may lead to the burial/obfuscation of possible geomorphic indicators of discrete lateral earthquake offsets.
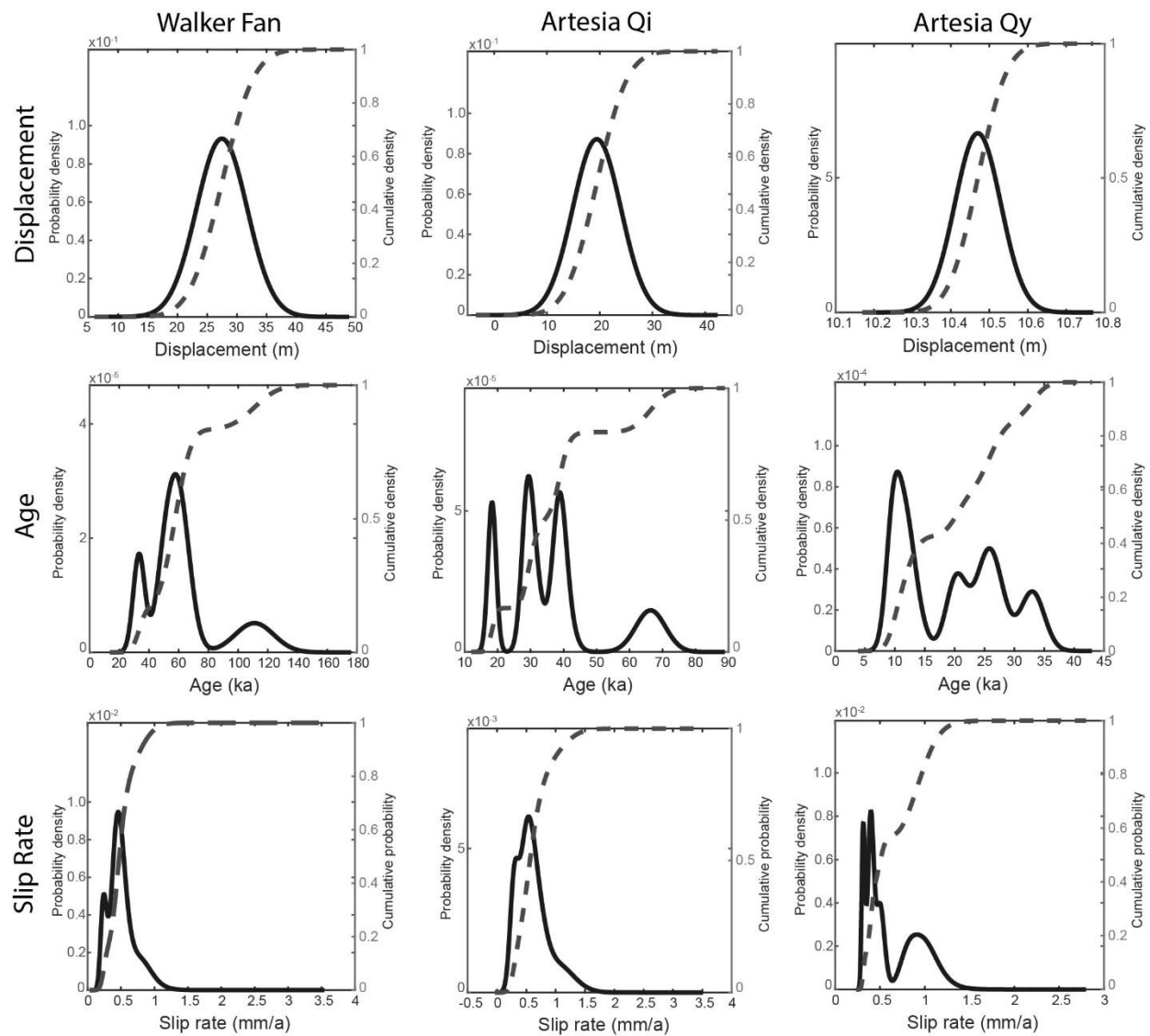
Figure 2 Displacement, age, and vertical slip rate probability distributions for the Antelope Valley and Smith Valley (Artesia) range bounding faults. For each plot, probability densities are the solid lines (left axis), while cumulative probabilities are the dashed lines (right axis).
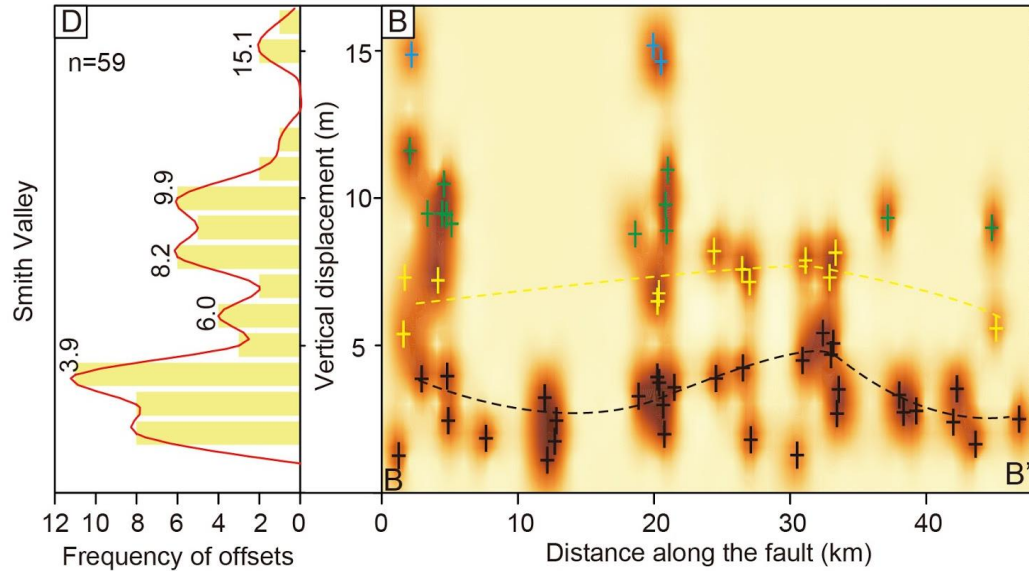
Figure 3 (above) along strike scarp height distribution of the Smith Valley rangefront fault. See figure 4 for reference line B-B'
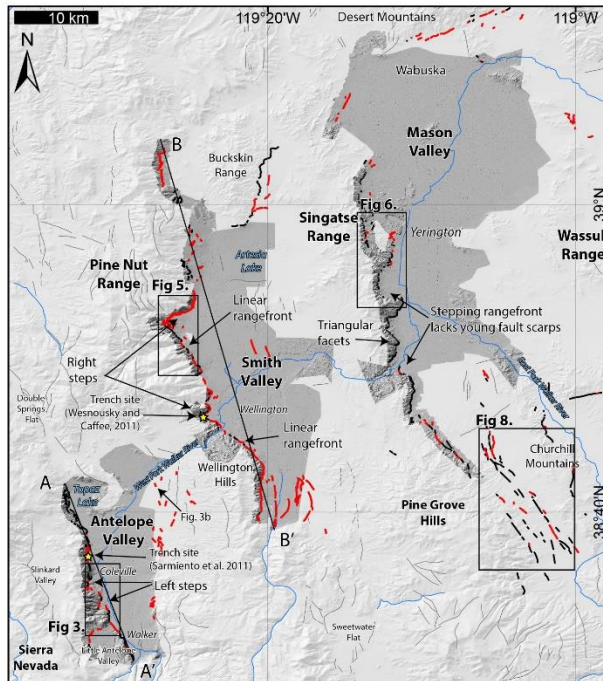
Figure 4 (left): overview of CWL – line B-B' in Figure 3 shown for reference

Table 1 (below): comparison of results from slip distribution (Fig 3) to trench (Wesnousky & Caffee, 2011), and resulting magnitude based on empirical relations of Wesnousky (2008). Recurrence based on dividing slip rate by displacement as well as trench result.

	Most Recent	Penultimate
Trench	3.5 m	-
Slip Distribution	3.9 m	2.1 m
Length	45 km	
Magnitude	6.9-7.3	
Recurrence	3.5-6.5 kyr	

1.2.3 Artesia Fan and Lake Wellington

Marith Reheis

The roadcut at the north edge of the Artesia fan exposes yellowish lacustrine sediments interbedded with colluvium. Descriptions of this site by different people disagree. Stauffer (2003) described this section (see measured section below) and sampled an ash layer (unit 3C) exposed near the base. The same ash bed was sampled by Wesnousky and Caffee (2011), who reported a correlated age of ~75-80 ka (see below). M. Reheis first described this roadcut in 1995 (unpublished field notes; it will be interesting to see if this still holds water!) and at that time interpreted two units of fault-scarp-derived colluvium interbedded with the lake sediments (see annotated photos below). The upper colluvium (shown in measured section) was deposited when the lake had dropped below the elevation of the exposure, as indicated by mudcracks at the top of the lake sediment. The older colluvial unit, about 25 cm thick, fell into water or wet sediment, as indicated by dropstones impressed into lake sediment about 1 m above the ash bed (shown in photos).
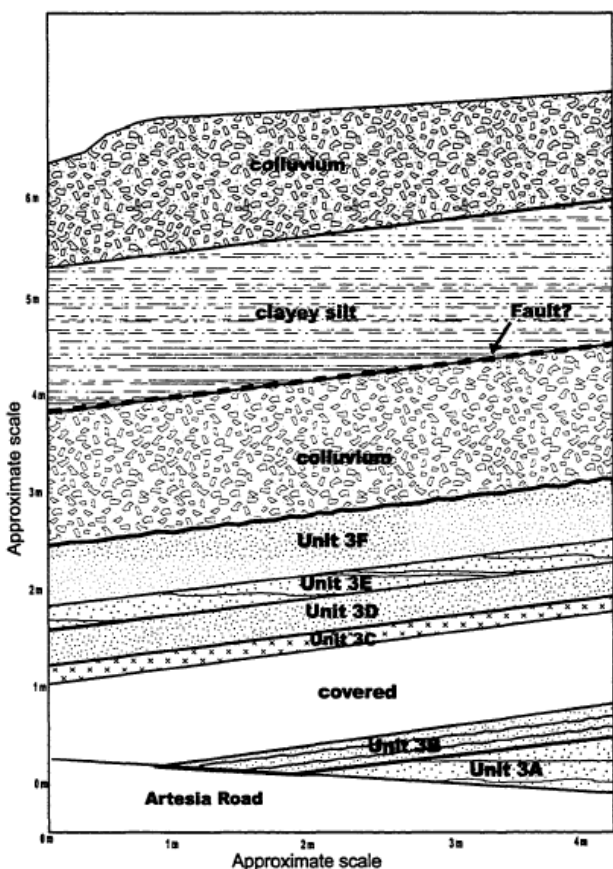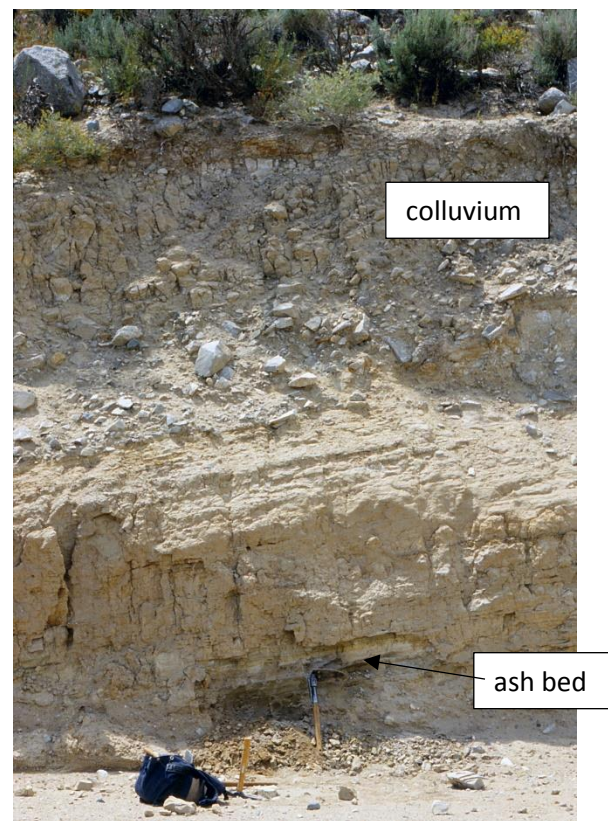

Figure 23. Schematic diagram of east-facing roadcut exposure at Section #3 (Fig. 9) along Artesia Road. Roadcut is a little more than 6 m high.

Above figure taken from Stauffer (2003).
Photos to right taken by M. Reheis, 2002.

Pluvial Lake Wellington occupied Smith Valley during the early part of the late Pleistocene, and possibly at earlier times (Mifflin and Wheat, 1979; Stauffer, 2003). Today, the valley is traversed by the West Walker River, which exits via Wilson Canyon to Mason Valley and there joins the East Walker River to feed Walker Lake. A remnant of Lake Wellington is preserved as Artesia Lake, a few km northeast of the Artesia fan, separated from the West Walker River by a low divide. The most prominent shoreline features, including wave-cut scarps on the north and east and a well-preserved beach barrier at the north end of the valley, define a highstand at about 1477 masl (meters above sea level) (Stauffer, 2003). Two ash-bed localities in lacustrine sediment, one near Nordyke Pass southeast of Artesia Lake and one at this field trip stop, yielded correlations to ash beds in cores from Owens Lake and Walker Lake with estimated ages between about 80 ka and 60 ka (Stauffer, 2003; Wesnousky and Caffee, 2011). Relict soils on the northern barrier (stop 6, day 2, 2010 FOP guidebook) and elsewhere, combined with the ash bed ages, are interpreted to indicate that the last highstand of Lake Wellington occurred during marine isotope stage (MIS) 4 (Stauffer, 2003). No evidence to date supports a lake during MIS 2. However, reconnaissance studies by M. Reheis (field notes, 1995, and Reheis et al., 2003, stop 1-2A) and by S. Wesnousky (2010 FOP guidebook, stop 8) suggest that a higher, and probably older, lake occupied the valley and may have reached a highstand of about 1487 masl. Wesnousky noted the presence of beach rock and rounded gravels around the west end of Wilson Canyon at about 1480 masl, and Reheis observed tufa-cemented sandy pebble gravel at ~1487 masl north of the river. In addition, cobble-boulder gravel is preserved on benches at about 1485 masl (see photos below), high on the canyon walls about 1.5 km southwest of the mouth of Wilson Canyon (Reheis et al., 2003, stop 1-2A). Wesnousky (2010 guidebook) speculated that a landslide may have blocked the canyon to create the MIS-4 highstand. As noted by Stauffer (2003), further work is needed to elaborate the history of Lake Wellington and its relation to the West Walker River.

View east of flood (?) boulders (left) deposited on bedrock, and closeup of boulders with daypack for scale (right), N side Wilson Canyon (photos by M. Reheis, 2002).

Mifflin, M. D., and Wheat, M. M., 1979, Pluvial lakes and estimated pluvial climates of Nevada: Nevada Bureau of Mines and Geology Bulletin 94, 57 p.

Reheis, M., Redwine, J., Adams, K., Stine, S., Parker, K., Negrini, R., Burke, R., Kurth, G., McGeehin, J., Paces, J., Phillips, F., Sarna-Wojcicki, A., and Smoot, J., 2003, Pliocene to Holocene lakes in the western Great Basin: New perspectives on paleoclimate, landscape dynamics, tectonics, and paleodistribution of aquatic species, *in* Easterbrook, D., ed., Quaternary Geology of the United States: Reno, Desert Research Institute, p. 155-194.

Stauffer, H. L., 2003, Timing of the last highstand of Pluvial Lake Wellington, Smith Valley, Nevada: M.S. Thesis, San Jose State University, San Jose, 120 pp.

Wesnousky, S.G., and Caffee, M., 2011, Range-bounding normal fault of Smith Valley, Nevada: Limits on age of last surface-rupture earthquake and late Pleistocene rate of displacement: Bulletin of the Seismological Society of America, Vol. 101, p. 1431–1437.

1.3 Mason Valley Overview

1.3.1   Mason Valley

Mason Valley is a 55-km-long by 20-km-wide half-graben bounded by active faults separating the basin from the Singatse Range to the west and the Pine Grove Hills to the southwest. The Desert Mountains bound the northern margin of Mason Valley where the northeast-striking left-lateral Wabuska fault is located (Li et al., 2017). The Singatse Range is considerably smaller in topographic expression than the other ranges in this region, forming only ~700 m of relief above the valley floor. The northern portion of the basin was occupied by pluvial Lake Lahontan during its high stand ~14.5 ka (Adams and Wesnousky, 1998; Reheis, 1999), and prominent wave-cut shoreline benches and beach deposits are preserved on Qy deposits that are below the ~1332 m elevation of the high stand. Evidence for any pre-Holocene faulting in much of the northern portion of the basin may be obscured by lacustrine processes associated with Lake Lahontan and evidence of more recent faulting in the central portion of the basin may be obscured by agricultural activity.

The region to the east/southeast of Mason Valley, and east of the Churchill Mountains, forms a series of complicated small basins and mountain ranges composed of incised Qi aged and older fan/pediment surfaces, short discontinuous faults, and disrupted bedrock **(Plate 1)** (Gilbert and Reynolds, 1973). These basins are both oriented north-south and east-west. The faults in this part of the basin strike both north-northwest and east-northeast, and are generally only traceable for a maximum of ~5 km.

The fault at the base of the Singatse Range forms a sinuous trace with frequent left and right steps and bends from ~5 km south of where the west fork of the Walker River enters the basin for ~35 km northward. The Singatse range front is composed of prominent triangular facets, suggestive of active normal faulting, however the fault along the Singatse Range is almost always only expressed as a bedrock alluvium contact, except for the site described in the following section, and forms a sharp contrast with other major range bounding faults in the area that often exhibit scarps in young alluvial deposits. In several places along the rangefront small antithetic grabens are observed, yet there is a dearth of uplifted fan surfaces.

The character of rangefront faulting in Mason Valley abruptly changes ~5 km south of where the west fork of the Walker River enters the southwestern margin of the basin. The southern part of the basin is bound by the Pine Grove Hills, and instead of forming a rangefront composed of sharp triangular facets, the rangefront is subdued and is composed of a series of uplifted old alluvial fans and pediments. Here, satellite imagery and lidar data show a discontinuous series of linear, northwest-striking faults and lineaments that extend for ~22 km until the southernmost extent of the basin. Generally these faults have a northeast down sense of motion, and locally right-laterally displace fan deposits and channels.

Yerington Slip Rate Site
Adjacent to the Yerington Pit (**Figure 1**) a northwest striking fault scarp merges with a northeast striking fault scarp to form a large northeast striking graben cutting intermediate age alluvial fan deposits (**Figure 1**). The alluvial fan is incised up to ~6 m by channels and forms broad smooth interfluve surfaces with infrequent highly weathered granitic and volcanic boulders. Depending on where fault profiles are measured (**Figure 1**), vertical separation varies from as little as 1.4 m across the graben at the northeastern extent of the fault scarp to as much as 10.8 m, with an average of 6.5 ± 3.6 m for the 6 profiles. Here, we collected a depth profile of 4 samples as well as 4 surficial boulder samples for cosmogenic ^{10}Be analysis to constrain the age of the faulted surface. Boulder ages sampled from the Qo surface here range from 90.5 ± 6.9 ka to 451.1 ± 37.2 ka with a mean of 204.6 ± 169.9 ka, and modeling the depth profile results in an age of 173.1 $^{+38.7}$/$_{-32.5}$ ka. The well-developed soil, with a thick Bt horizon, is consistent with the modeled age of the depth profile. Combining the 173.1 $^{+38.7}$/$_{-32.5}$ ka age of the depth profile with the 6.5 ± 3.6 m average displacement of the surface results in a vertical slip rate of <0.04 mm/yr. The geometry of the linear northwest striking fault segment associated with a large northeast

striking graben is consistent with northwest-directed dextral motion, however the measured slip rate is very low and thus this fault does not likely accommodate a significant amount of the regional strain.
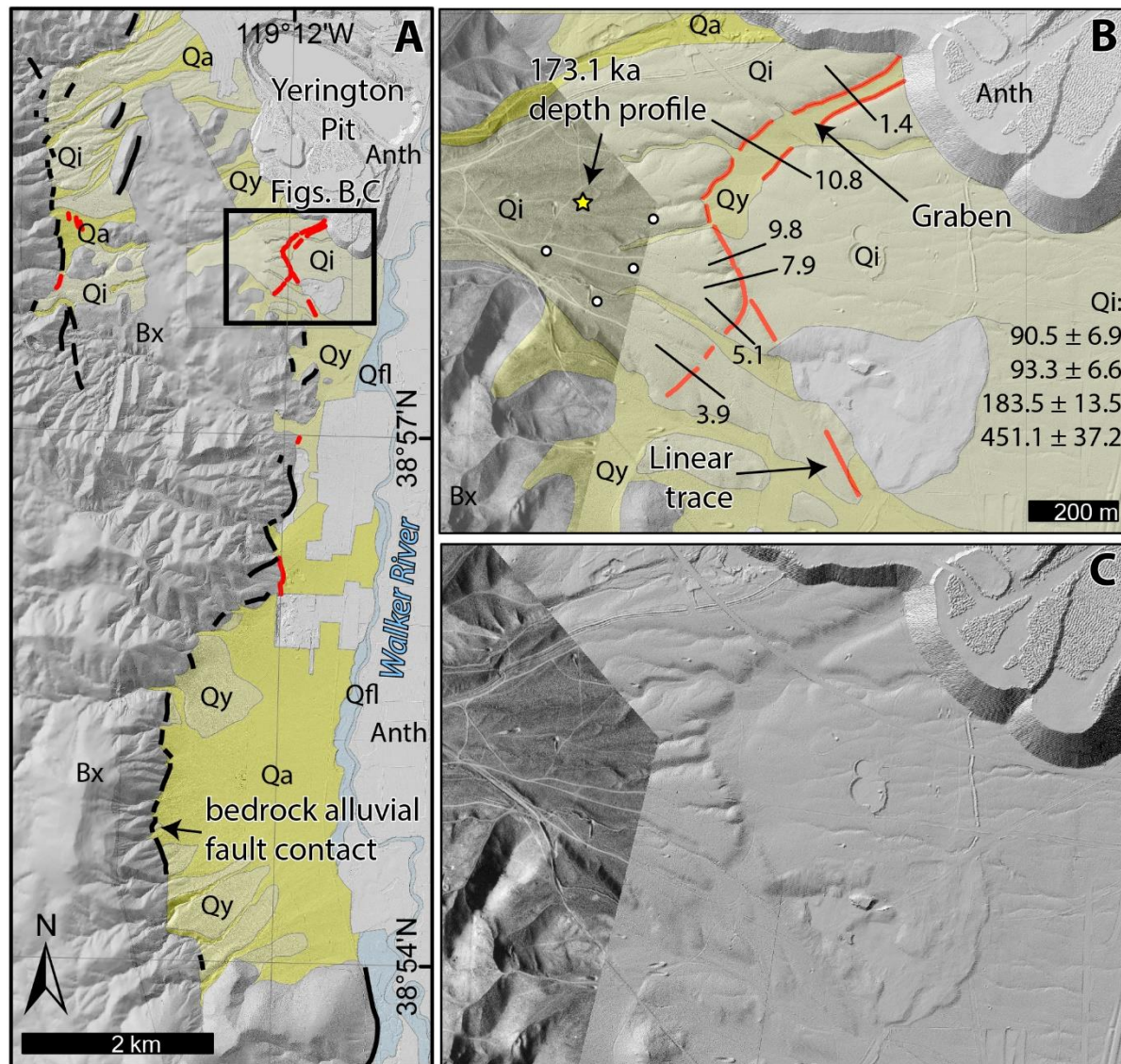

Figure 1 *Section of Mason Valley rangefront (a) showing lack of fault scarps preserved in alluvium (red) and location of Yerington fan slip rate site (b). Yerington fan rate site interpreted (b) and bare lidar hillshade / low sun angle aerial photo composite (c). Scarp profiles, heights (in m), and ages (ka) of boulder samples (white dots) are shown in (b), while the age and location of the depth profile (Figure 7) is indicated by the star.*

1.3.2   Wabuska Lineament and Left Lateral faulting in the Carson Domain

Characterizing the Quaternary expression of active faulting along the Olinghouse, Carson, and Wabuska lineaments of the Walker Lane

Xinnan Li[1,2], Weiliang Huang[2,3,*], Ian K.D. Pierce[2,4,*], Stephen J. Angster[2,4,*], and Steven G. Wesnousky[2,4,*]
[1]State Key Laboratory of Earthquake Dynamics, Institute of Geology, China Earthquake Administration, No. 1, Huayanli, Chaoyang District, Beijing 100029, China
[2]Center for Neotectonics Studies, University of Nevada, Reno, MS 169, 1664 N Virginia Street, Reno, Nevada 89557, USA
[3]College of Geologic Engineering and Surveying of Chang'an University, 126 Yanta Avenue, Yanta District, Xi'an, Shaanxi Province, China
[4]Nevada Seismological Laboratory, University of Nevada, Reno, MS 169, 1664 N. Virginia Street, Reno, Nevada 89557, USA

The northwest trend of major right-lateral faults in the Walker Lane is interrupted by the presence of northeast-striking left-lateral faults within the Carson and Excelsior domains. Previous studies in the Carson domain have suggested that left-lateral slip on the northeast-striking Olinghouse, Carson, and Wabuska lineaments accommodates Walker Lane transtensional dextral shear through the clockwise rotation of intervening crustal blocks. Our observations confirm and document the presence of late Pleistocene–Holocene faulting along each of these lineaments. Fault scarps along the Carson and Wabuska lineaments are discontinuous and sparse, and show evidence for left-lateral faulting, locally including linear fault traces, alternating scarp face directions, and lateral offsets of small gullies and ridges. The trends of scarps that define these lineaments link at their western ends with north-trending active normal faults. In this manner, it appears that the 5–7 mm/yr of right slip taking place across the northern Walker Lane is being accommodated by the combined processes of basin opening in the west and block rotation to the east. This mode of slip transfer differs from the Excelsior domain, where active left-slip faults and clockwise rotation of crustal blocks are confined to, and the result of, a distinct right step between right-lateral faults of the southern Walker Lane and central Walker Lane, respectively. The observation of these apparently diverse modes of development of left-slip faults and vertical axis rotations provides an example of the complexity that may be expected in the structural development of continental shear zones that have been characterized by transtension.

Wabuska Lineament:

The mapped traces of the discontinuous Quaternary faults are shown on a hillshade image and a simplified Quaternary map in Figure 9. Mapped fault traces are limited to the east of U.S. Route 95, are above the ca. 15.5 ka highstand of Lake Lahontan, and have a right-stepping en echelon pattern (Fig. 9). No Quaternary fault scarps are observed along the similar northeast-trending linear valley of Churchill Canyon on the west side of U.S. Route 95 (black arrows, Fig. 9), although we lack lidar data coverage for much of this lineation. The youngest alluvial units (Qy) are post-Lahontan fan and wash deposits; themapped intermediate-aged (Qi) fans are >1 m above the active channels and have shoreline scarps and deposits on their surfaces (Figs. 10A, 10B). We subdivide the youngest alluvial unit into Qy1 and Qy2, as fault scarps are present within Qy2 and not within Qy1.
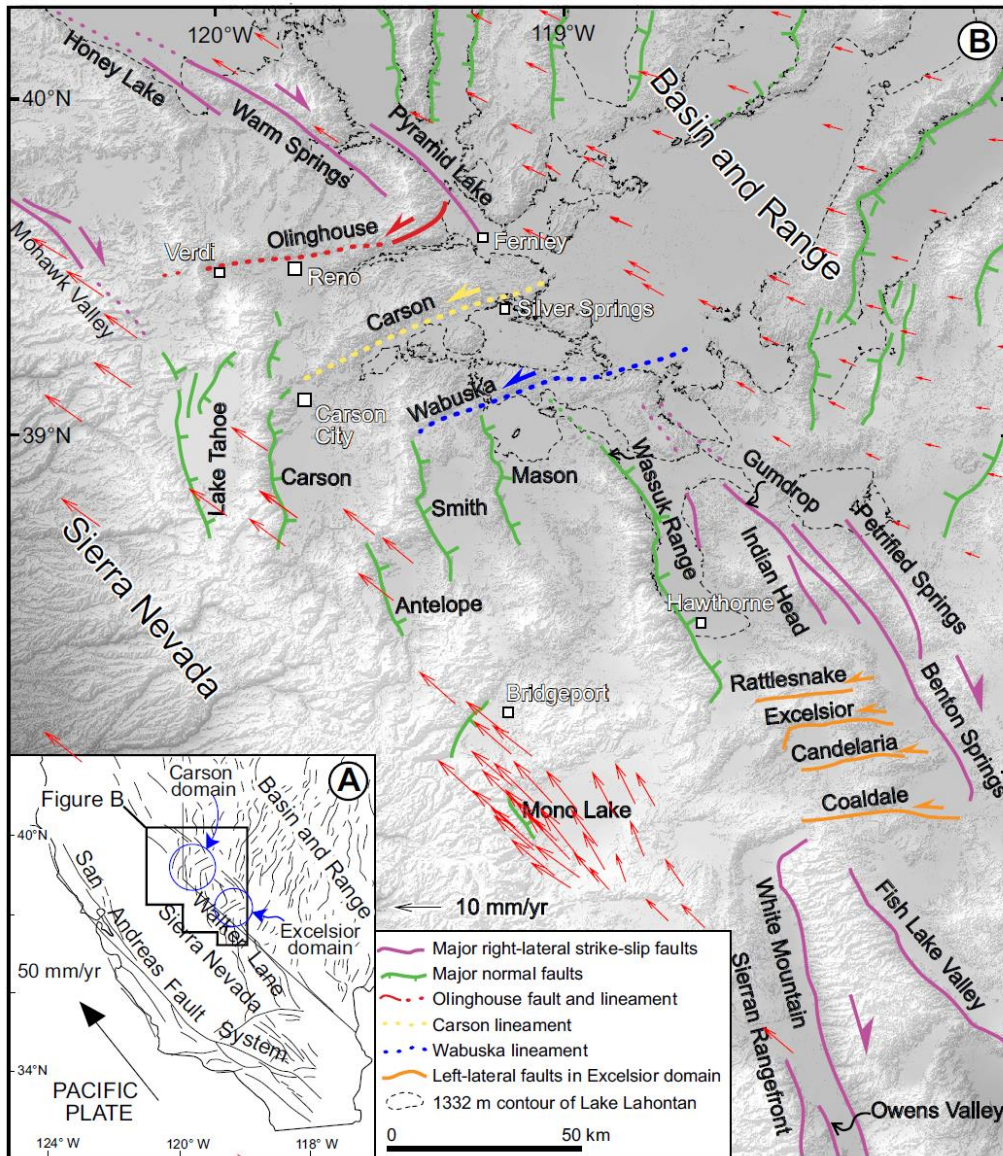
Figure 1. Tectonic setting of the study area. (A) Regional fault map showing faults of the San Andreas, Walker Lane, and Basin and Range. Locations of the Carson and Excelsior domains are outlined by blue circles. (B) Enlarged view of the Walker Lane displaying physiographic and fault trends. The northeast-trending Olinghouse (red), Carson (yellow), and Wabuska (blue) lineaments are the focus of this study. Normal faults (teeth on downthrown side) are green, right-lateral strike slip faults are magenta, and left-lateral strike-slip faults of Excelsior domain are orange. Thin dashed line is highstand contour (1332 m) of pluvial Lake Lahontan. Red arrows are global positioning system velocity vectors plotted with respect to stable North America adapted from Hammond and Thatcher (2007).
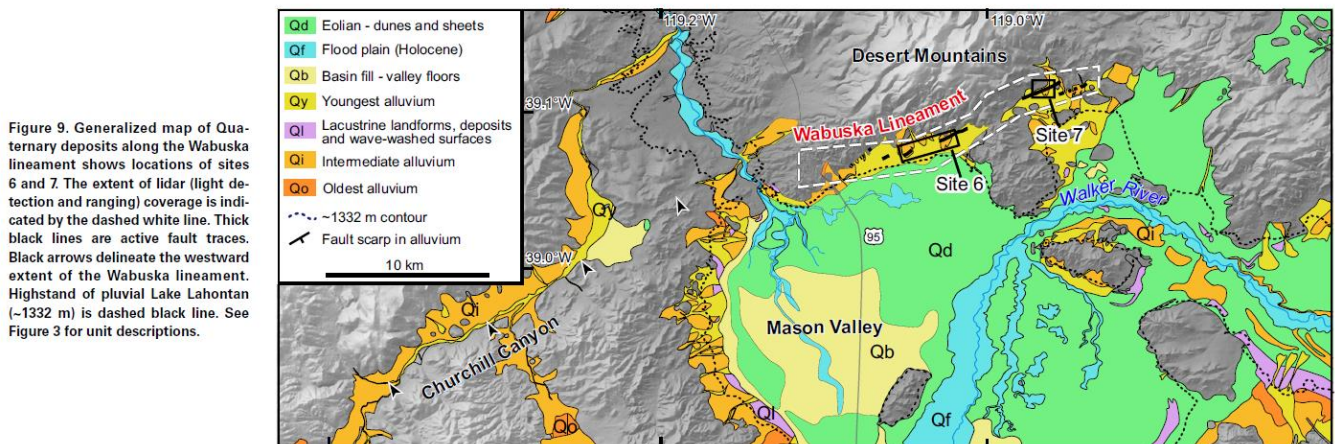

Figure 9. Generalized map of Quaternary deposits along the Wabuska lineament shows locations of sites 6 and 7. The extent of lidar (light detection and ranging) coverage is indicated by the dashed white line. Thick black lines are active fault traces. Black arrows delineate the westward extent of the Wabuska lineament. Highstand of pluvial Lake Lahontan (~1332 m) is dashed black line. See Figure 3 for unit descriptions.
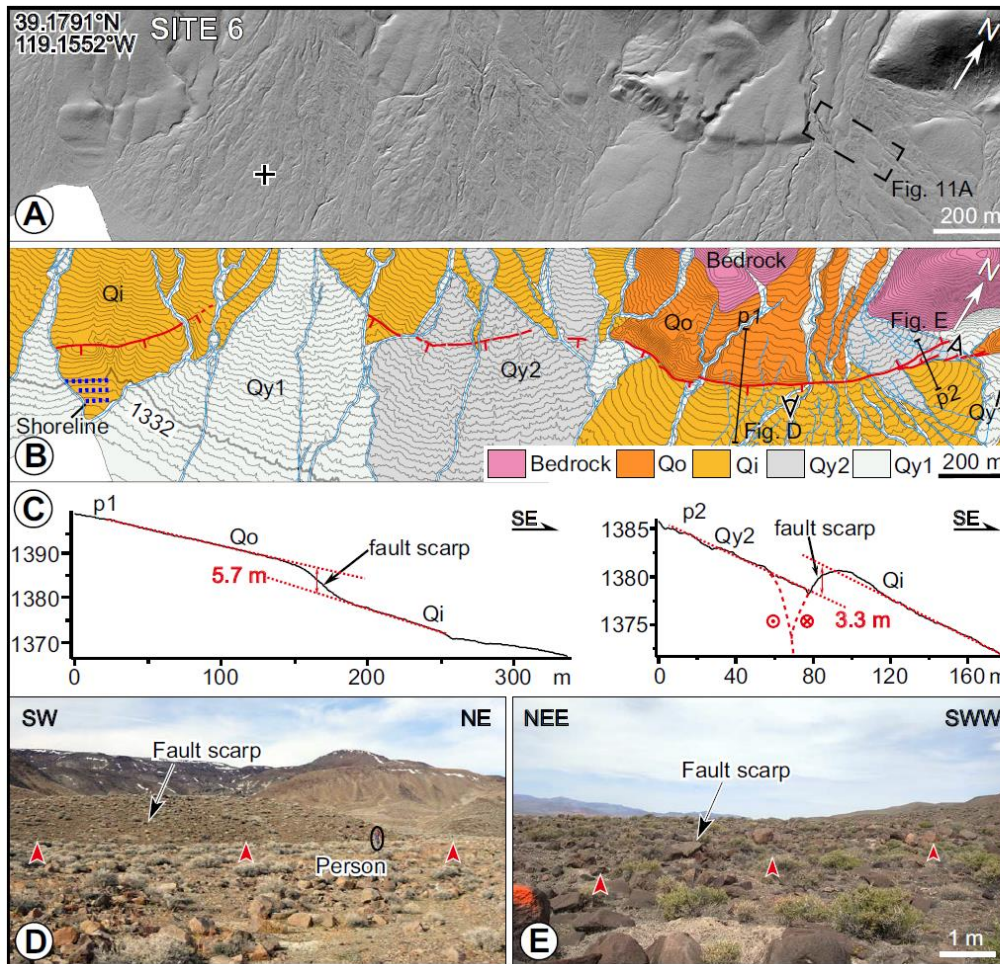
Figure 10. Displaced geomorphic features along the fault trace at site 6. (A) Lidar (light detection and ranging) hillshade image. (B) Quaternary map with active fault scarps shown as red lines (teeth on downthrown side) at the southeastern range front of the Desert Mountains (location outlined by box in Fig. 9). Contour interval is 2 m. See Figure 3 for unit descriptions. (C) Topographic profiles along lines p1 and p2 (shown in B) illustrate the height of scarps. The fault trace is characterized by both uphill- and downhill-facing fault scarps. (D) Field photograph showing fault scarp that forms southeast boundary of Qo surface. (E) Field photograph showing northwest-facing uphill fault scarp. Perspectives of photos in D and E are provided in B.

At site 6 (Figs. 9 and 10) we observe that the northeast-trending fault scarps cut predominantly through the intermediate-aged fan units and within Qy2 deposits (Figs. 10A, 10B). A larger scale lidar hillshade image (Fig. 10A) and photos Figures 10D and 10E provide a more detailed picture of the neotectonic and Quaternary characteristics of the fault morphology at site 6. At the western edge of site 6 (Fig. 10A), the Lahontan shorelines modify an intermediate-aged (Qi) fan deposit (Figs. 10A, 10B), allowing for a minimum age of the Lahontan highstand (ca. 15.5 ka) to be assigned to the intermediate (Qi) surface. Young fan units (Qy1 and Qy2) deposits cut or buried these intermediate (Qi) deposits and do not contain shoreline deposits. At site 6 (Fig. 10), a linear continuous fault scarp cuts across the front of an older fan (Qo) deposit and is expressed within the Qy2 alluvial deposits, which exhibit muted levee and channel topography and are younger than the Lahontan highstand (ca. 15.5 ka), based on the stratigraphic relations described here. Considering the intense damage from the reported 25 June 1933 Wabuska earthquake (~M6) (Reno Evening Gazette, 1933) and prior earthquakes recorded on other faults with similar magnitudes (M6 and M6.2) that have ruptured the ground surface (e.g., DeLong et al., 2015; Xu et al., 2015), one may speculate that the scarps were produced in 1933. Topographic profiles across the fault scarps show both uphill- and downhill-facing scarps with heights ranging from ~3 to 6 m (Fig. 10C). The linearity of the trace and reversal of scarp directions along strike indicate that the Wabuska lineament is a strike-slip fault.

1.4 Pine Grove Hills

1.4.1 Overview

      Figure 1a is a Google Earth satellite image of a portion of the southern part of Mason Valley. Here, several subparallel fault traces are well expressed as a series of linear bedrock ridges and scarps in different ages of alluvial fans (**Plate 1**). The linear bedrock ridges are primarily composed of Mio-Pliocene sedimentary and volcanic rocks, including the Morgan Valley and Coal Valley formations (Gilbert and Reynolds, 1973). **Figure 1b** is a Quaternary map based on a hillshade of a 0.25 m/pixel resolution structure-from-motion model of a part of one of these northwest striking fault-lineaments, where a linear fault trace right-laterally displaces Qy and Qi deposits. Two Qi terrace risers are displaced ~25 and ~18 m right-laterally, and a channel is dextrally offset ~20 m by this fault. Additionally along the strike of this fault are two beheaded channels, two right-laterally deflected channels, and a small shutter ridge (**Figure 1b).** Additionally, the direction of the scarp produced by the fault changes from west facing, to east facing, to west facing again along strike, demonstrating the strike-slip nature of this fault. The morphology of the Pine Grove Hills fault is similar to other active strike-slip faults in the region with slip rates ranging from ~0.5 to 1.5 mm/yr (e.g., Wesnousky, 2005; Angster et al., 2019). No age estimates of the offset surfaces are available to determine a slip rate for the Pine Grove Hills fault.
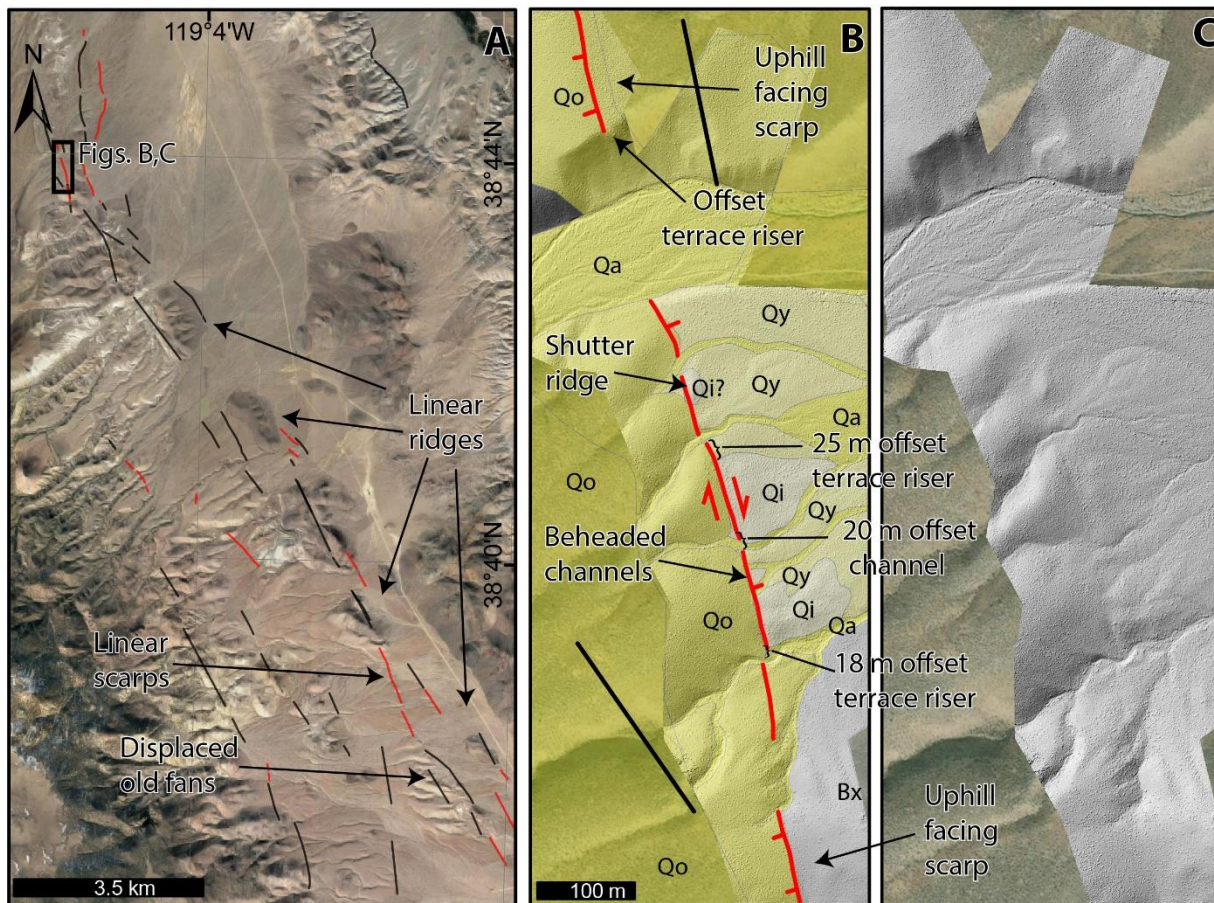

Figure 1 Satellite image of the Pine Grove Hills fault zone in southern Mason Valley (a). Red lines indicate faults in alluvial deposits, while black are fault traces in bedrock. (b) shows an interpreted SfM model (c) of a section of this fault zone that demonstrates right-lateral displacements.

Figure 2 Aerial view of stop – star denotes parking area. Several lineaments expressed as sharp contacts of older fans and bedrock popups extend from this area ~25 km to the north.

Figure 3: Google maps satellite view of this stop. Arrows highlight fault traces. Yellow arrow is stop location.

Figure 4: Satellite image of stop. Are any of these apparent lateral offsets (color coded arrows) real? How do you estimate a slip rate for a fault that lacks quality piercing points?

1.4.2   Comparison to 2019 Ridgecrest Sequence

Preservation of offsets in this type of environment – analogous to the July 4 2019 Mw 6.4 Ridgecrest earthquake

Figure 1: Image showing a ~1.3 m left lateral offset channel taken 10 weeks after the Ridgecrest earthquakes. These features will likely be destroyed after the first set of storms hits the region. Location in following images. The natural variability of fan channels, especially in proximity to faults makes this defining offsets difficult.

Figure 2: (Top) Pre-earthquake google maps image of the trace of the July 4, Mw 6.4 Ridgecrest event. Arrows highlight tectonic features along the trace of the surface rupture. These features are not dissimilar to the Pine Grove Hills fault, including a lack of pre-existing kinematic indicators/ piercing points. Star is location of lower image.

Figure 3: (Bottom) There is not an obvious pre-existing lateral displacement of any of these channels/surfaces. Arrows approximate fault trace and star is photo on preceding page.

2 DAY 2: Walker Lake Basin

2.1 Fletcher Valley

2.1.1 Fletcher Valley and Lake Russell overflow

Marith Reheis

Camp is at the north edge of Aurora Crater, Qb4 (andesite, 0.2-0.5 Ma; Silberman and McKee, 1972; Lange et al., 1993) in the air photo below. This morning we will be viewing a small part of the evidence for northward overflow of pluvial Lake Russell (Mono Lake) during the early Pleistocene. This episodic discharge via Mud Spring Canyon into the East Walker River occurred when lake levels were much higher (15-90 m higher) than at Lake Russell's last overflow southward via Adobe Valley into the Owens River (Reheis et al., 2002). The overflow pathway into and through Mud Spring Canyon was repeatedly blocked by basalt and andesite flows and then re-incised; for details see the appended pdf.

En route to this stop from our camp at Fletcher Spring, the road lies atop the north wall of a paleovalley (Mud Spring 1) cut into Pliocene(?) fan gravel and later filled by a 1.3–Ma basalt flow (Qb3) to the south. Note how the road is higher than the flow top to the west. The base of the flow is exposed to the south and, for the energetic, can also be accessed by a 2-km walk east from camp, where you can find fluvial gravel beneath the flow. Also note that Mud Spring Canyon is greatly overfit relative to its drainage area (Reheis et al., 2002, 2003). Continuing east on the graded gravel road, cross Mud Spring Canyon and ascend the pediment surface to the north. Note the roadcut exposure of latest Miocene deposits capped by gravel and intercalated paleosols.
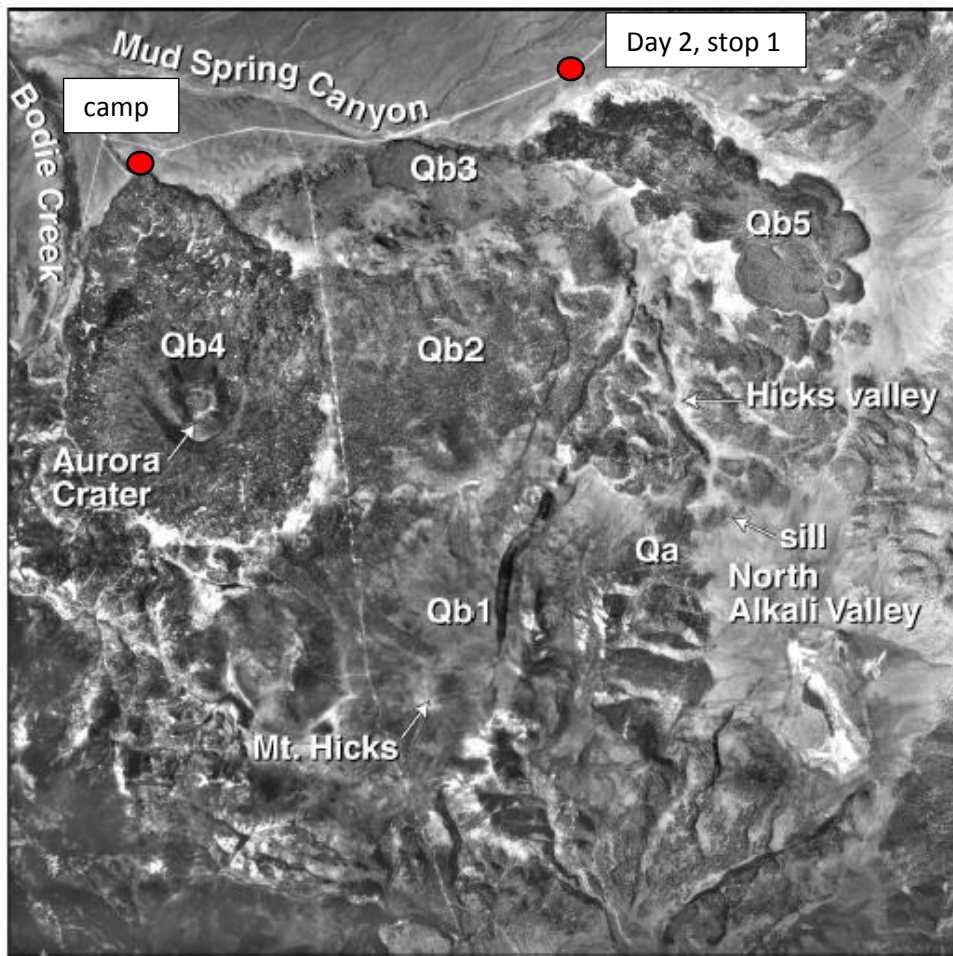
At the field trip stop, the view to the south shows the feather-edge of a young flow (Qb5, hornblende andesite, <0.04 Ma) that filled against, and lapped over, the north wall of a paleovalley (Mud Spring 2). Pale sediments visible below the basalt flow are 2–2.5 Ma, dated by correlation of tephra layers (Reheis et al., 2002). Mt. Hicks, the highest cone to the south, is the source of one flow (Qa, andesite, ~1.6 Ma) that filled and flowed down Mt. Hicks spillway. Mt. Hicks was a major source of obsidian for Native Americans. See schematic reconstruction of event history on next page.

Qb, basalt and andesite flows numbered oldest (Qb1) to youngest (Qb5). Qa, ~1.6-Ma andesite that flowed into the Mt. Hicks sill and down through Hicks Valley, later re-incised. Figure from Reheis et al. (2002).
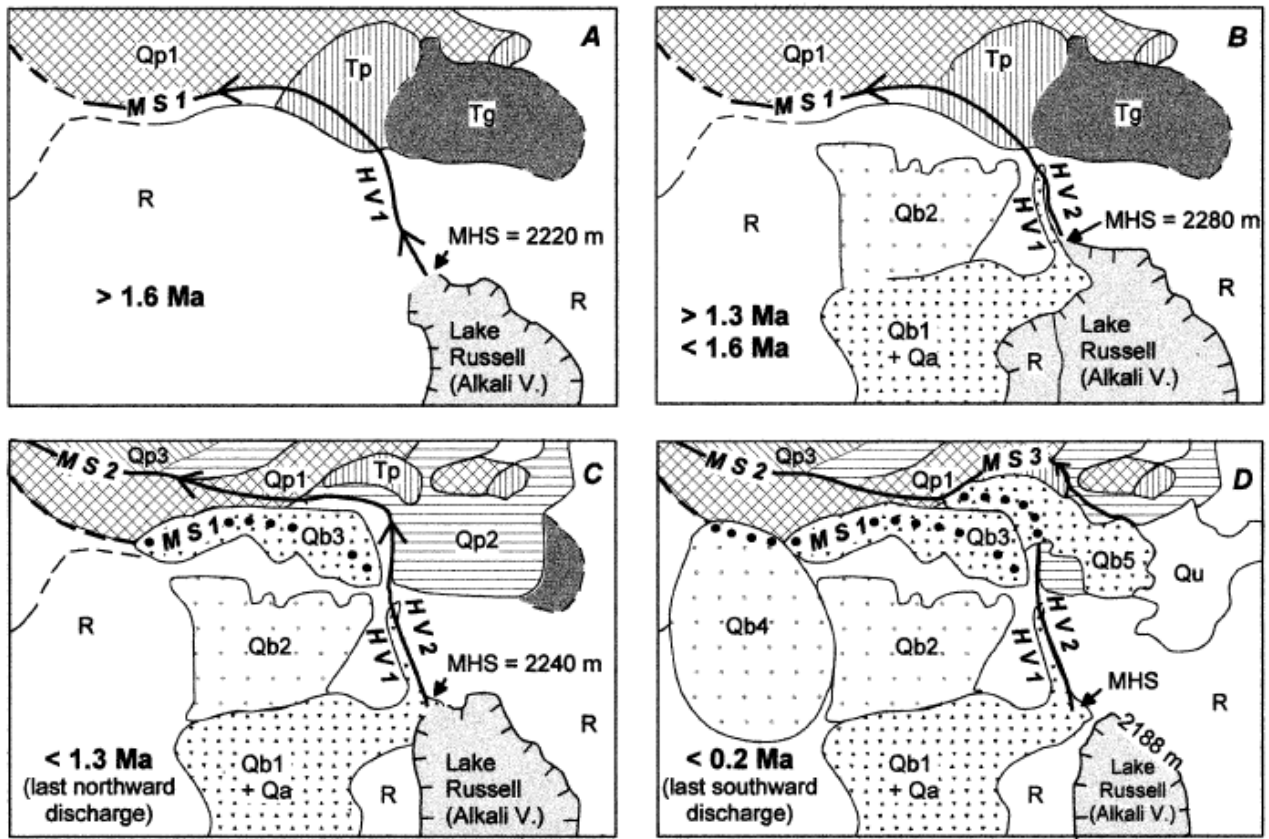
Schematic reconstruction of the sequence of valley incision and volcanic eruptions (A–D) in the area of Mount Hicks spillway (MHS) and Mud Spring Canyon (copied from Reheis et al., 2002). Heavy lines show drainageways of Hicks Valley (HV1, HV2) and Mud Spring Canyon (MS1, MS2, MS3); dashed where uncertain, dotted where buried by volcanic flows. Numbers in meters are estimated altitudes of the spillway and coeval lake levels. Qb and Qa, volcanic flows; Qp and Tp, Quaternary and Tertiary pediment gravel, respectively; Tg, late Pliocene tuffaceous alluvium; R, older volcanics and granitic bedrock; Qu, undifferentiated Quaternary deposits (mostly alluvium).

Lange, R. A., Carmichael, I. S. E., and Renne, P. R., 1993, Potassic volcanism near Mono basin, California: Evidence for high water and oxygen fugacities inherited from subduction: Geology, v. 21, p. 949-9952.

Reheis, M. C., Stine, S., and Sarna-Wojcicki, A. M., 2002, Drainage reversals in Mono Basin during the late Pliocene and Pleistocene: Geological Society of America Bulletin, v. 114, p. 991-1006.

Reheis, M., Redwine, J., Adams, K., Stine, S., Parker, K., Negrini, R., Burke, R., Kurth, G., McGeehin, J., Paces, J., Phillips, F., Sarna-Wojcicki, A., and Smoot, J., 2003, Pliocene to Holocene lakes in the western Great Basin: New perspectives on paleoclimate, landscape dynamics, tectonics, and paleodistribution of aquatic species, in Easterbrook, D. J., ed., Quaternary Geology of the United States (INQUA 2003 Field Guide Volume): Reno, Desert Research Institute, p. 155-194.

Silberman, M. L., and McKee, E. H., 1972, A summary of radiometric age determinations on Tertiary volcanic rocks from Nevada and eastern California: Part II, Western Nevada: Isochron/West, no. 4, p. 7

2.1.2 The Nine Mile Ranch Sequence (3 M$_w$ 5.4-5.6) from 2016-2019: Relocations, Tectonic Implications, and Comparisons to Recent Sequences

Rachel Hatch[1], Kenneth Smith[1], Rachel Abercrombie[1,2], Christine Ruhl[3], Bill Hammond[1,4], Ian Pierce[1,5]

[1] Nevada Seismological Laboratory, University of Nevada, Reno, NV 89557

[2] Department of Earth and Environment, Boston University, Boston, MA 02215

[3] Department of Geosciences, University of Tulsa, Tulsa, OK 74104

[4] Nevada Geodetic Laboratory, University of Nevada Reno, Reno, NV, USA

[5] Center for Neotectonics Studies, University of Nevada, Reno, NV 89557

Introduction

On Dec. 28th, 2016 three moderate sized earthquakes occurred within one hour of each other in the Walker Lane, southwest of Hawthorne, NV in Fletcher Valley, NE of Bodie Hills and North of Mono Lake (Figure 1). The sequence began with a Mw 5.6 at 08:18 UTC and was followed 4 minutes later by an Mw 5.4. The third large event, a Mw 5.5, occurred at 09:13 UTC, 55 minutes after the initial earthquake. The total Mw of all three events ~Mw 5.9. These events damaged historical 1800's URMs at Nine Mile Ranch as well as caused liquefaction and surface cracks. The sequence takes place in close proximity to Aurora Crater and other local volcanic centers, with the most recent volcanism estimated at 250 Ka. Additionally, the sequence occurs in the northwest corner of the Mina Deflection, a major structural right step within the Walker Lane, characterized by ENE-trending normal and sinistral faults (Figure 1).

Our study aims to detect structures, characterize the spatio-temporal evolution of the seismicity, and place our observations within the context of the active tectonics in the region, which are poorly understood. These events give us the opportunity to investigate the area, in addition to compare to other recent sequences. We update relocations, gather focal mechanisms and moment tensor solutions, and add a stress tensor inversion, and GPS analysis to understand the aspects of the sequence. We hope to provide insight into triggering processes, geometric relationships, and potential hazard implications.

The Nine Mile Ranch (NMR) sequence takes place within the Walker Lane Tectonic region. This region accommodates 10-12 mm/yr of right-lateral shear (Hammond and Thatcher, 2004); however, it remains unclear how and what percentage of this shear is accommodated on mapped active fault structures (Wesnousky et al., 2012). Possible mechanisms that could be contributing at this latitude include (1) left-lateral faulting and clockwise block rotations, (2) right-lateral slip on northwest trending strike slip faults in the east, and (3) extension and clockwise block rotations across a left-stepping series of en-echelon normal fault-bounded basins (Bormann et al., 2016). The NMR sequence was only moderate in size, and therefore not large enough to significantly contribute to the tectonic movement of the Walker Lane; however, we hope to use this study for extrapolating characteristics of sequences and swarms observed in the area to understand potentially damaging events in the future (i.e. Ridgecrest).

Nine Mile Ranch Sequence Results

The Nevada Seismological Lab has located 7345 events in the NMR sequence to date. Using both absolute and relative relocation techniques, we relocate 87% of events, with depths ranging from 3-12 km, illustrating unmapped fault structures, and sub-structures, including conjugate faulting (Figure 2). The largest structure detected strikes ~N57W, and dips ~60° to the NE. Two conjugate SW-striking, vertical fault planes lie at both ends of the larger fault. The three main events are located near one another at the intersection of the NW-striking fault plane and the southern-most SW-striking conjugate structure. Moment tensor solutions of the main events show high-angle strike-slip faulting, with focal mechanisms of smaller events showing strike-slip and normal ruptures (Figure 3). Using the relocations, we approximate the first event as occurring on the SW-striking left-lateral plane, with the second occurring on the dipping NW-striking right-lateral fault plane, and the third event occurring more shallow on the SW-striking left-lateral plane. The first event in sequence is the Mw 5.6 event with no detectable foreshocks prior. Moment tensor solutions show nearly pure double-couple solutions. Besides the 3 M 5+ events, this sequence generally behaves similar to a mainshock-aftershock type sequence. Additionally, we detect no migration of events.

We attempt a basic coulomb stress analysis to test our claim that the initial event occurred on the left-lateral fault plane. Using the Coulomb3 software, we input the fault geometry based on the relocated hypocenters, and the parameters based on the moment tensor magnitudes of the events. We tested the model with the initial event (Mw 5.6) on the left-lateral plane. This model showed the coulomb stress increase on the right-lateral fault plane, enhancing the stress prerequisite for failure. When tested for the initial event on the right-lateral plane, the model leads to a coulomb stress decrease onto the left-lateral plane, therefore deterring failure on the left-lateral plane. This basic model assists us in determining that the sequence initiated with the Mw 5.6 event on the left-lateral structure, and the subsequence event (Mw 5.4) was likely the direct reaction to the increase in static stress onto the right-lateral fault.

Additional analyses include a stress tensor inversion using the first motion focal mechanisms, a long-term GPS strain tensor, and a GPS measures time-series strain rate of the area prior and after the NMR sequence. The stress inversion shows the extension direction at ~N85E, which correlates well with moment tensor solutions. Interestingly, the GPS time-series analysis shows at the time of the NMR events, the dilatational strain rate was in a local minimum and shear strain rate was at a local maximum, resulting in favorable conditions for an event to occur. Further analysis and testing must be completed to determine the validity of the preliminary results.

Our long-term GPS strain tensor and analysis of the coseismic offsets suggest right and left-lateral faulting; with focal mechanisms showing oblique and normal events, the NMR sequence likely included dip-slip motion as well. Mechanisms, fault plane orientations, GPS, and stress inversion results are consistent with a transtensional environment.

Hawthorne 2011 Swarm

In 2011, ~20 km to the east of the Nine Mile Ranch sequence, a swarm occurred with 50 earthquakes M ≥ 3.0 with the largest event at Mw 4.6. Out of 1973 total events in the Hawthorne 2011 sequence, we relocate 1859

events using both absolute and relative relocation processes. Two fault structures are identified at shallow depths (0-3 km), striking NNE dipping ~NW (Figure 3). Prior to temporary station installation, event depths were poorly constrained.

The Hawthorne 2011 is a swarm-like sequence, and occurred in the footwall of the westward tilted normal fault of the Wassuk Range (southern end). We detect a migration of events going from east to west, and slightly south to north over several months. Recent work by Zha et al. (2018) shows that the deformation is characterized by normal faulting, in a tensile stress environment. Their spatio-temporal temporal observations suggest aseismic slip may play a role in the swarm within the regional tectonic stress.

Ridgecrest 2019 Comparison

The Ridgecrest sequence (July 2019, M6.4 and M7.1) in the southern Walker Lane, is the focus of much ongoing work, and shows some similarities and differences to the NMR sequence. A fault orientation similar to NMR appears in the Ridgecrest sequence prior to the occurrence of the M7.1, but the right-lateral plane for NMR is dipping. The Ridgecrest sequence also initiated on a SW-trending left-lateral fault plane. We observe differences in spatio-temporal evolution of both sequences: NMR main events ruptured within an hour of the initiation, while the Ridgecrest main events were ~36 hours apart. Additionally, the tectonic regime of both sequences is just north of significant left-lateral step overs, with Ridgecrest occurring in close proximity to the Garlock fault.

We calculate a long-term strain tensor for Ridgecrest. Both Ridgecrest and NMR have similar preliminary strain tensor directions and values; the shear strain rate at both are also very similar; however, the dilatational strain rate is lower at Ridgecrest. This could be a feature that caused one sequence to be much larger than the other.

Key Points

Our investigation shows that the Nine Mile Ranch sequence occurred on an unmapped fault including, at least, three separate structures; strike-slip, normal, and oblique events correlate well with established structures and sub-structures. Hypocenter relocations and a basic coulomb analysis indicate the first event initiated on the left-lateral fault plane, with the second event on the right-lateral, dipping fault plane, located in the increased coulomb stress region. Mechanisms, fault plane orientations, GPS analyses, and stress inversion results are consistent with a transtensional environment.

The NMR sequence and the Hawthorne 2011 sequence highlight the variable drivers of seismicity within this area of the Walker Lane. Understanding these drivers can assist in future hazard assessment, in terms of defining what the aftershock characteristics we may see during a sequence. Additionally, relocating the seismicity can assist with unknown structures and geometry at depth.

Further analysis of the Ridgecrest sequence is required for a more complete comparison to NMR, but first order observations indicate similarity in geometry. Conjugate-type structures and sequences are common in the Walker Lane region, and should be taken into account for hazard analysis.
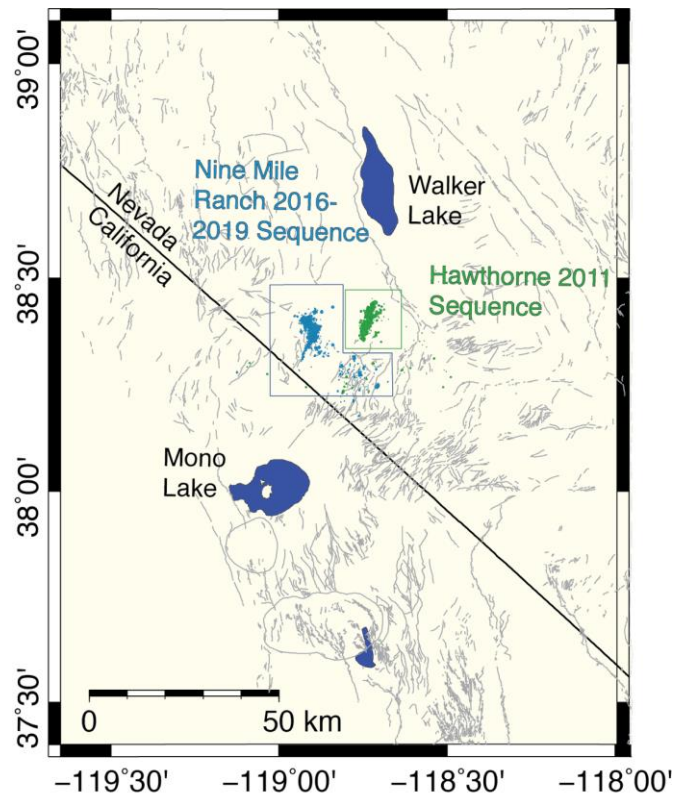
Figure 1: Overall region of the Nine Mile Ranch Sequence (blue) and Hawthorne 2011 sequence (green). California and Nevada boarder shown with the USGS Faults and Folds in grey and major nearby lakes in blue.
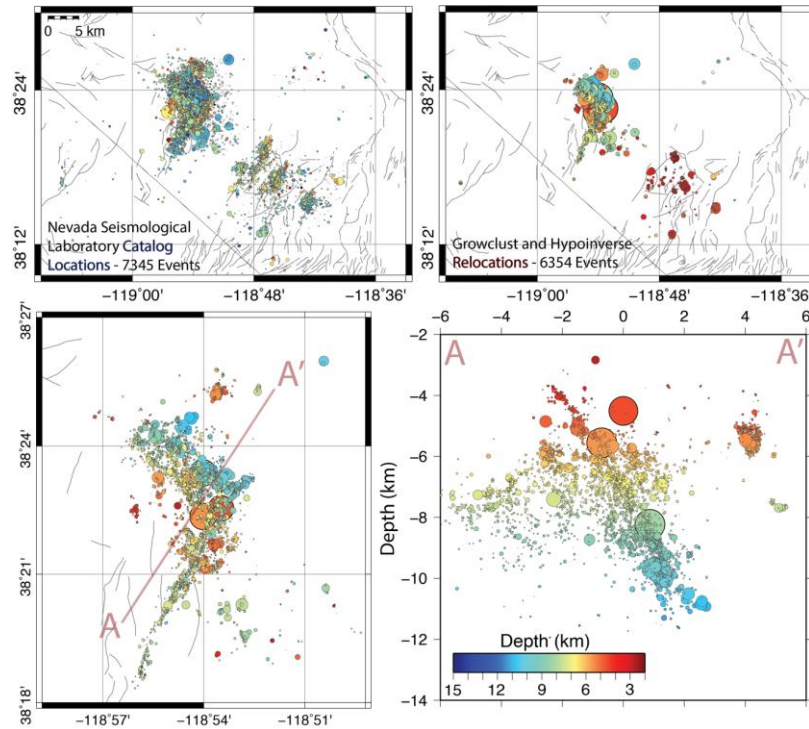
Figure 2: Above - Nine Mile Ranch catalog and relocated events colored by depth, and sized by magnitude. Below - Zoomed in set of relocations, sized by magnitude, colored by depth and cross section view at depth.
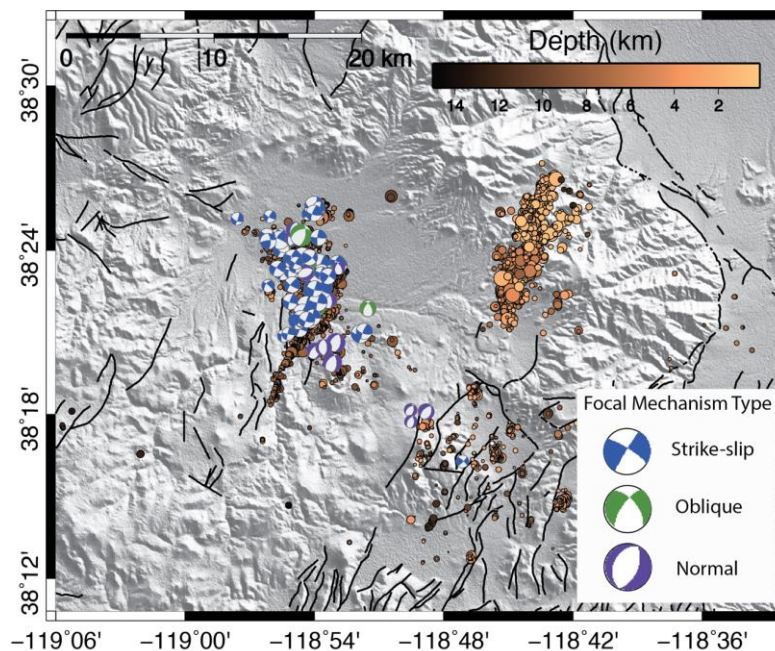

Figure 3: Shaded relief map of relocated Nine Mile Ranch events and Hawthorne 2011 events, sized by magnitude and colored by depth. For Nine Mile Ranch, focal mechanisms, colored by type, show predominately strike-slip with some oblique and normal motion. USGS Faults and Folds shown in black.

2.2 Walker Lake Overview

2.2.1   Walker Lake introduction

Pierce

The Walker Lake basin (**Figure 2**) is the largest basin of those examined and is ~100-km-long by 20-km-wide. The western margin of the basin is bound by the Wassuk range, which hosts a prominent active east-dipping normal fault, forming more than 2200 m of vertical relief. The vertical slip rate (>0.3–0.4 mm/yr) and paleoseismic history of this fault zone are described by Bormann et al. (2012). Here observations are focused on additional evidence of strike-slip faulting and fault geometry (**Figure 2**).

Directly west of Hawthorne (**Figure 2c**) is a northwest-trending, linear, uphill-facing fault scarp that right laterally displaces two terrace risers as well as a series of gullies. From this area south to Lucky Boy Pass (**Figure 2d**), the fault forms a right-stepping pattern of north and northeast trending normal fault scarps and northwest trending linear scarps.

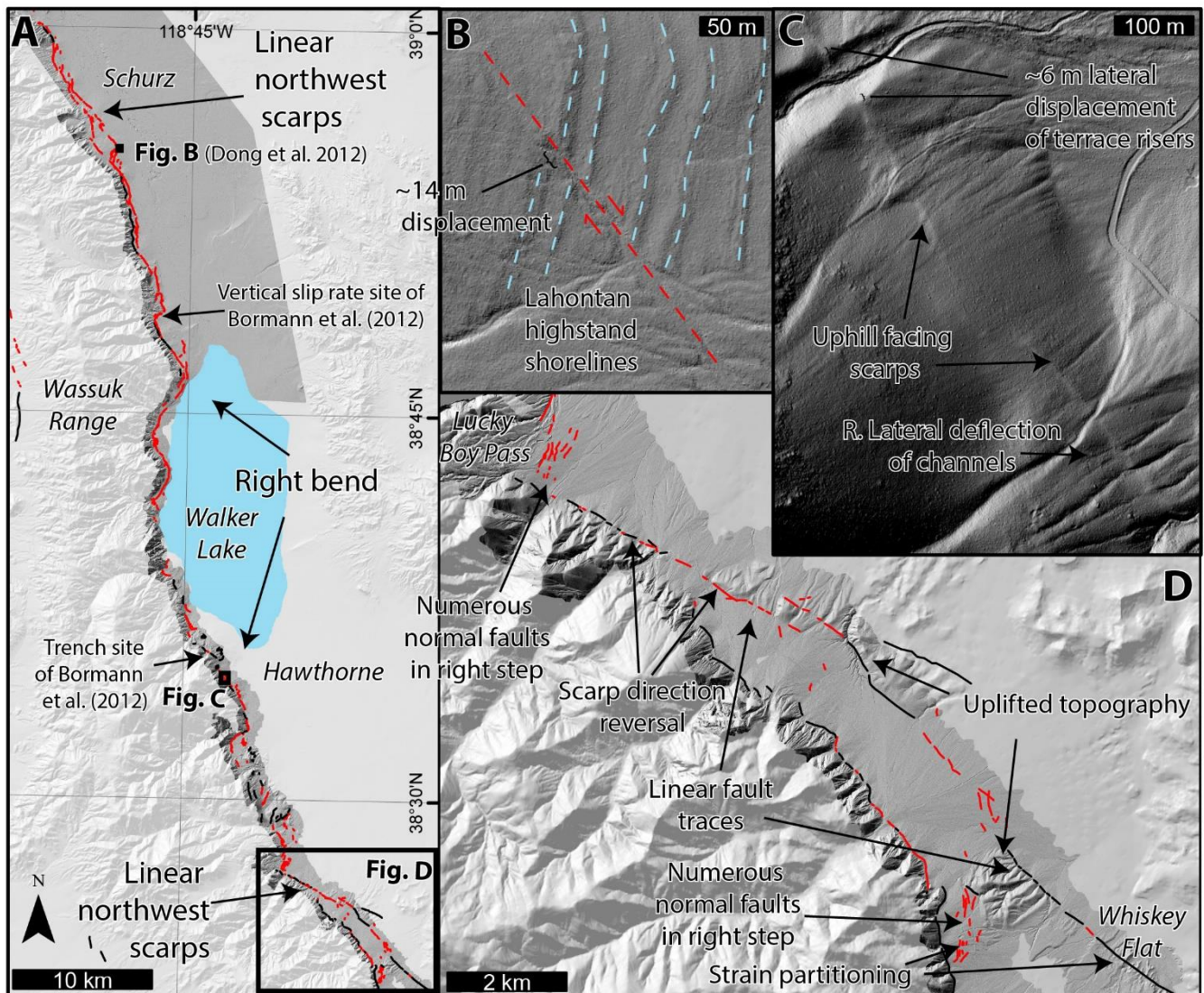Fig 1. Gullies laterally offset by an uphill facing scarp along the Wassuk Rangefront visible from this site.

A

118°45'W   39°0'N

Schurz

Linear
northwest
scarps

Fig. B (Dong et al. 2012)

Vertical slip rate site of
Bormann et al. (2012)

*Wassuk
Range*

38°45'N

Right bend

*Walker
Lake*

Trench site
of Bormann
et al. (2012)   **Fig. C**

Hawthorne

38°30'N

Linear
northwest
scarps

N

Fig. D

10 km

B   50 m

~14 m
displacement

Lahontan
highstand
shorelines

C   100 m

~6 m lateral
displacement
of terrace risers

Uphill facing
scarps

R. Lateral deflection
of channels

D

*Lucky
Boy Pass*

Numerous
normal faults
in right step

Scarp direction
reversal

Linear fault
traces

Numerous
normal faults
in right step

Strain partitioning

Uplifted topography
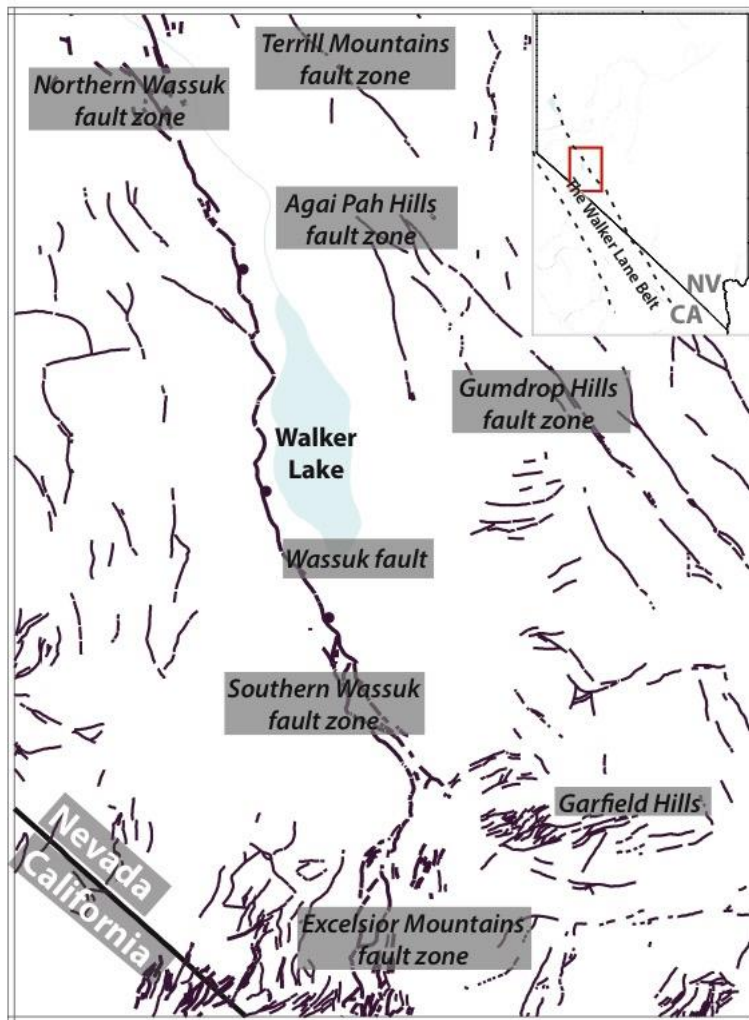
*Whiskey
Flat*

2 km

Fig 2   C shows a lidar hillshade of the gullies in the preceding photo, demonstrating the uphill facing scarp, laterally displaced gullies, and laterally offset terrace risers.

2.2.2   Offshore Walker Lake

Annie Kell, Nevada Seismological Lab
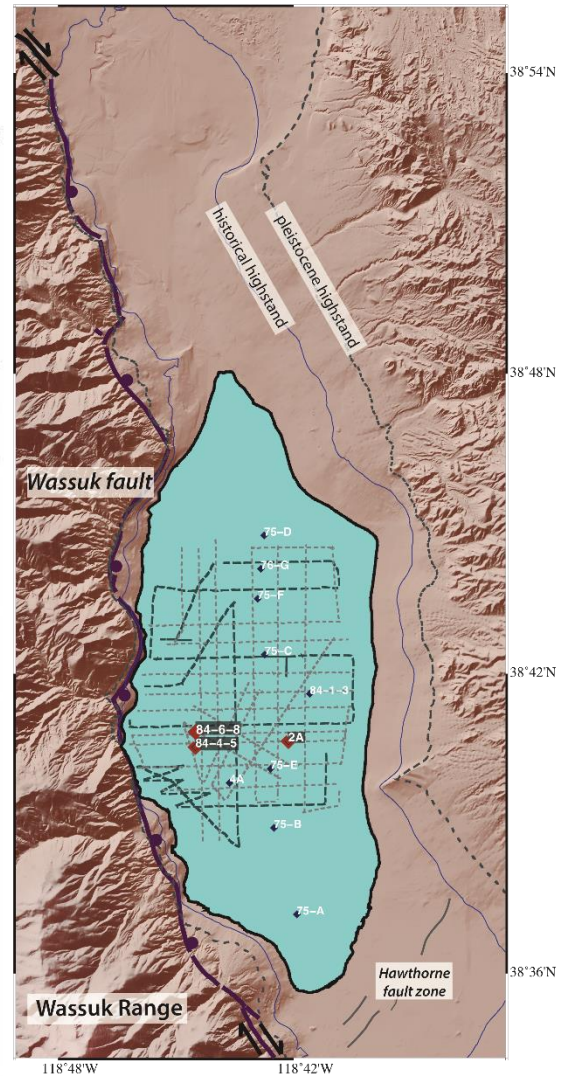
Walker Lake is located in the depocenter of a terminal basin within an arid region of Central Nevada, along the eastern corridor of the central Walker Lane. Like many basins within the Walker Lane Belt and across the Great Basin, Walker Lake is a fault-controlled lake basin, bounded to the west by the ~100 km-long Wassuk fault. Combining the findings from lake core studies within Walker Lake (e.g., Benson et al., 1991; Mensing et al., 2004) and existing land based seismic studies (Bormann et al., 2102; Surpless and Kroeger, 2015; Dong et al., 2014), we present a more detailed understanding of the fault structure and stress regime within Walker Lake and within the Wassuk fault zone.
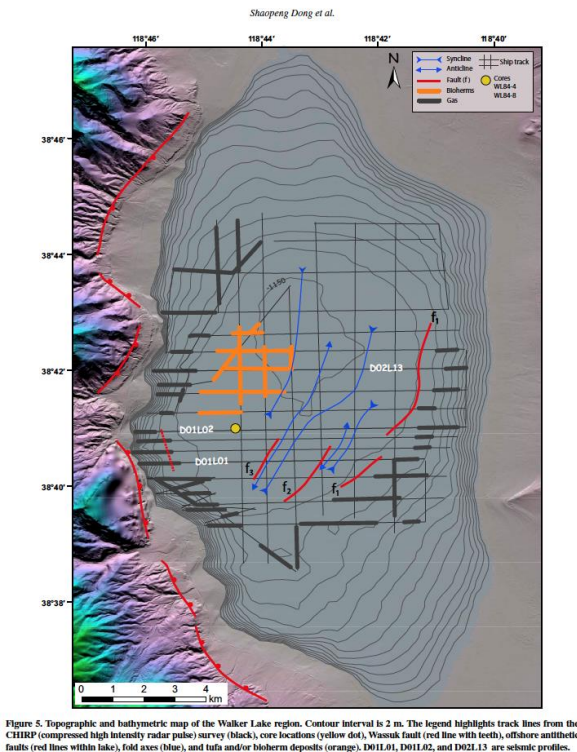
Figure 5. Topographic and bathymetric map of the Walker Lake region. Contour interval is 2 m. The legend highlights track lines from the CHIRP (compressed high intensity radar pulse) survey (black), core locations (yellow dot), Wassuk fault (red line with teeth), offshore antithetic faults (red lines within lake), fold axes (blue), and tufa and/or bioherm deposits (orange). D01L01, D01L02, and D02L13 are seismic profiles.

Figure from Dong et al., 2014 showing the locations for northeast striking faults within Walker Lake.
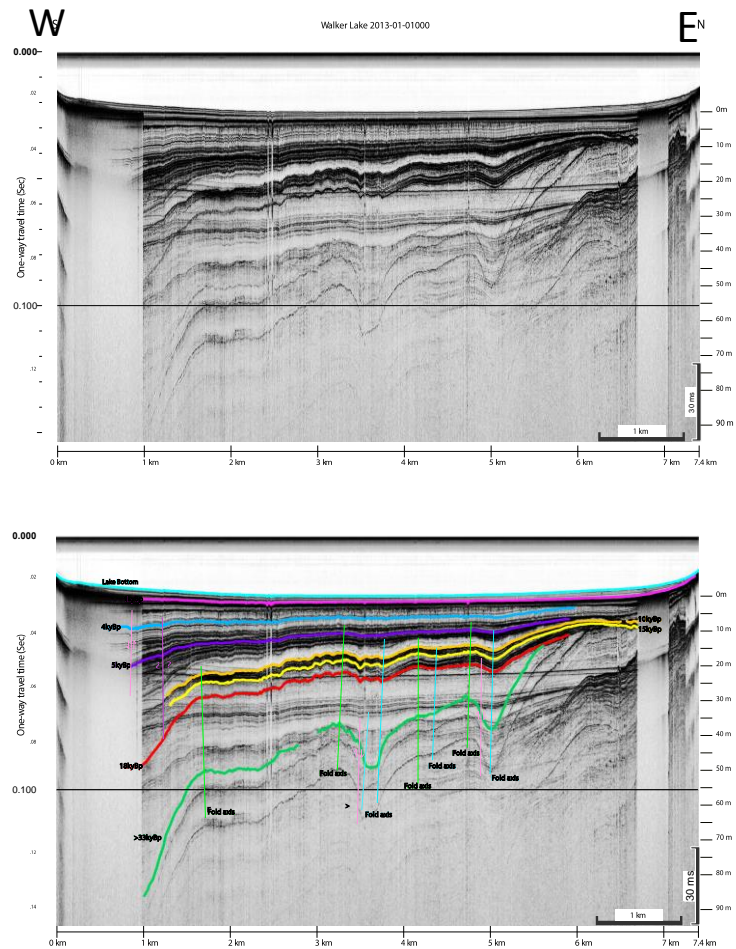
The location figure shows the track of where seismic CHIRP data were collected in relation to previously collected cores (Benson et al. 1991, for example). The seismic data image the deformation from the Wassuk fault within the lake sediments, and image a network of northeast striking faults within the middle and eastern portions of the lake. The high-resolution seismic data can be correlated to desiccation and flood events to help resolve discrepancies in the timing of these events. A masters student from the University of Nevada, Reno is currently working on these data to determine slip rate and the axes for the folds seen in the seismic data. For the 2019 FOP we will show some of the preliminary findings, namely the complex fault architecture within the lake and how the observed horizons match with notable core depths.

2.3 Offset Shorelines near Schurz

Modified after: Strike-slip faulting along the Wassuk Range of the northern Walker Lane, Nevada

by Dong et al. (2014); *Presented by Ian Pierce*

An enlarged portion of a 1:40,000-scale Nevada Bureau of Mines and Geology lowsun- angle photo of the fault trace where it cuts recessional shorelines of Lake Lahontan is shown in Figure 1A. The fault trace cuts from northwest to southeast across the central portion of the image. Several of the tonal bands resulting from shadows cast by the recessional beach ridges are offset right laterally across the trace. To measure the amount of offset, the photo was georeferenced to existing U.S. Geological Surveydigital raster graphics and orthophotoquads encompassing the site. The dashed line pairs in Figure 1B are along interpreted piercing point lines that follow the three most distinct tonal contrasts. The right-lateral offset of the tonal lineaments across the fault range from 11.7 to 15.2 m with an average of 13.5 m. In addition, we used a backpack global positioning system (GPS) to survey along our interpretation by eye of the crests and swales of a number of beach ridges. The range of 4 offsets measured in this way range from 12.3 m to 14.3 m, with an average of 13.9 m.

The offset shorelines postdate the highstand of pluvial Lake Lahontan (15,475 ± 720 yr B.P.). Dividing the ~14 m offset of the shorelines by the age of the highstand yields a minimum fault slip rate equal to ~0.9 mm/yr. The approximate fault slip rate assumes the total offset is due to multiple earthquakes.
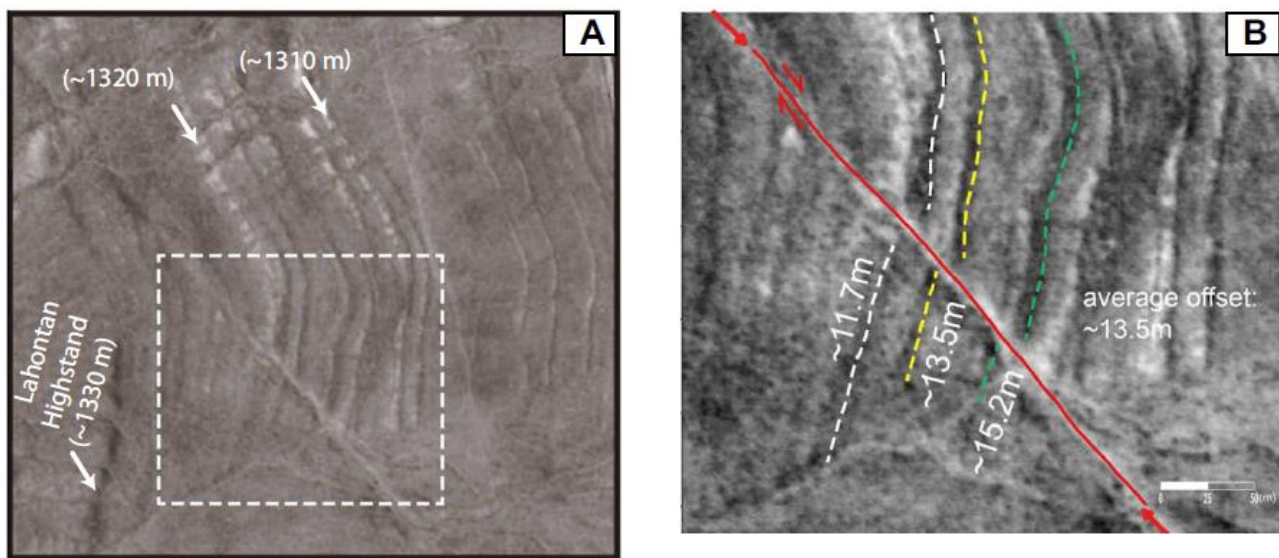

Figure 1. (Copied from Dong et al., 2014) (A) Fault trace cuts from northwest to southeast across the enlarged portion of low-sun-angle photograph and
shows right-lateral offset of tonal bands (shadows) that trend along the orientation of preserved recessional beach berms
and bars of pluvial Lake Lahontan (Nevada Bureau and Mines and Geology Project Bell Photo NJ11–1, 1–836, 1:40K,
4–30–80). Location is shown by small box in Figure 3B. (B) Enlarged portion within dashed box of A shows different
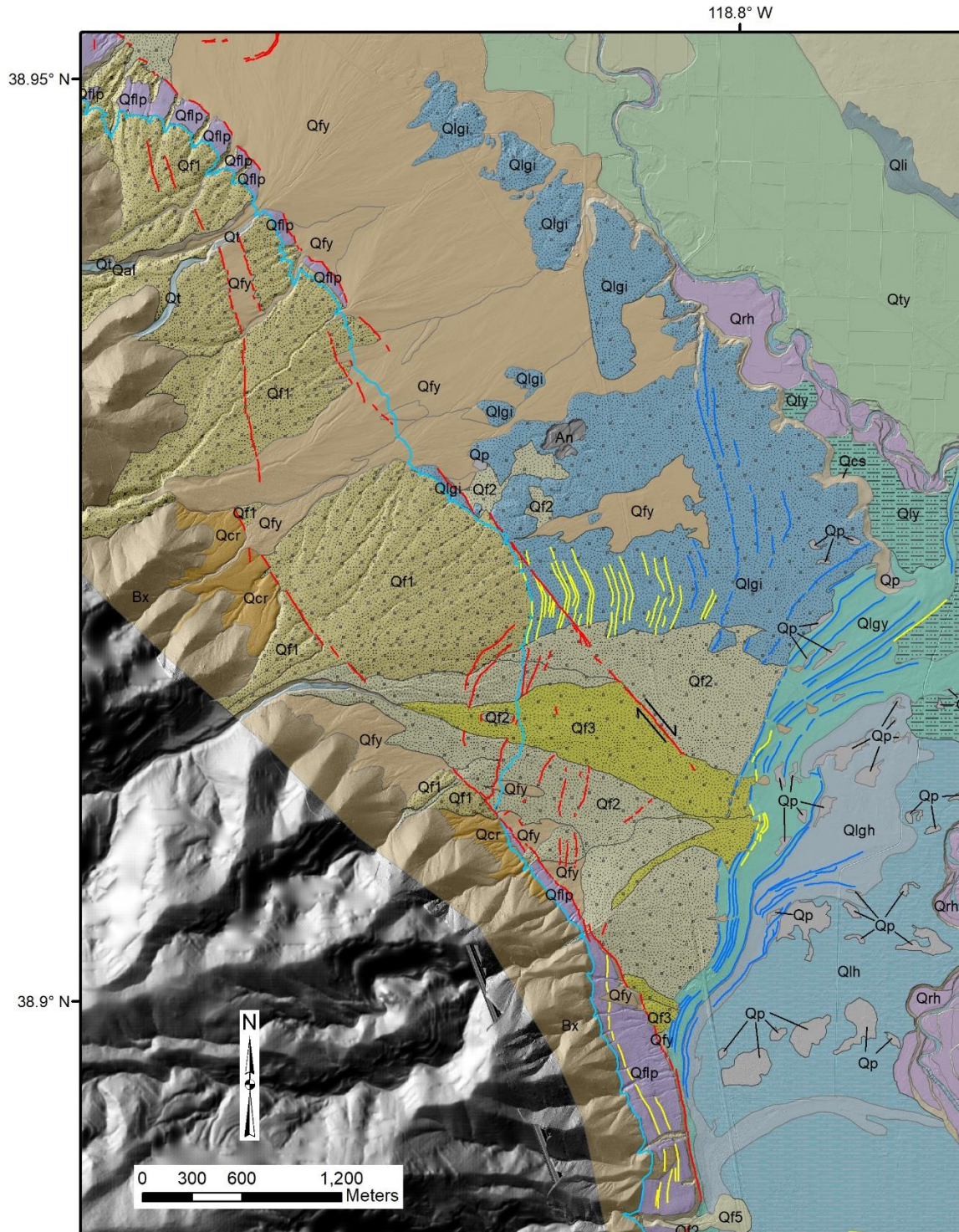piercing lines defi ned by tonal contrasts (dashed lines) used to estimate fault offset.

Figure 2 (Adams) Geomorphic map of the region surrounding stop 3.

2.4 Copper Canyon

2.4.1 Holocene Lake-Level Fluctuations, Alluvial Fan Activity, and Active Faulting at Walker Lake, NV

Kenneth D. Adams, Desert Research Institute

At this stop in the Copper Canyon embayment, we will look at the interactions between late Holocene shorelines, alluvial fans, and active faults. More specifically, dated shorelines at Walker Lake (Adams and Rhodes, 2019b) provide basin-wide horizontal chronostratigraphic timelines that were used to constrain the timing and distribution of alluvial fan activity around the basin through detailed mapping (1:5000-scale) on LiDAR basemaps, primarily using the concept of cross-cutting relations. The ages of the alluvial fans were then used to place constraints on the timing of active faulting along the Wassuk Range front. This study is part of a larger effort to determine the frequency and spatial distribution of Holocene alluvial fan activity along a 500 km-long north-south transect extending from Pyramid and Winnemucca lakes in the north (Adams and Rhodes, 2019a), Walker Lake in the middle (Adams and Rhodes, 2019b), and Owens Lake at the south end of the transect (Bacon et al., 2018).

Figure 1 presents the late Holocene Walker Lake-level curve of Adams and Rhodes (2019b), which updated the curve of Adams (2007) through additional luminescence dating of the late Holocene suite of shorelines. These shorelines are found between 1253 – 1262 m, or just above the 1868 CE highstand at 1252 m. The 1253 m shoreline dates to about 1000 cal yr BP, the 1257 m shoreline dates to about 2700 cal yr BP, and the 1262 m shoreline dates to about 3600 cal yr BP, representing the Neopluvial highstand (Adams and Rhodes, 2019b). The Lake Lahontan highstand shoreline is located upslope at an elevation of about 1332 m and dates from about 15,500 cal yr BP (Adams and Wesnousky, 1998).

Based on their cross-cutting relations with the shorelines, alluvial fans in the basin date from the historical period (post-1868 CE) (Qf5), 82 – 2700 cal yr BP (Qf4), 2700 – 3600 cal yr BP (Qf3), 3600 – 15,500 cal yr BP (Qf2), and >15,500 cal yr BP (Qf1). Where the age of young alluvial fans could not be determined because of their lack of direct interaction with young shorelines, they have been designated Qfy in Figure 2.
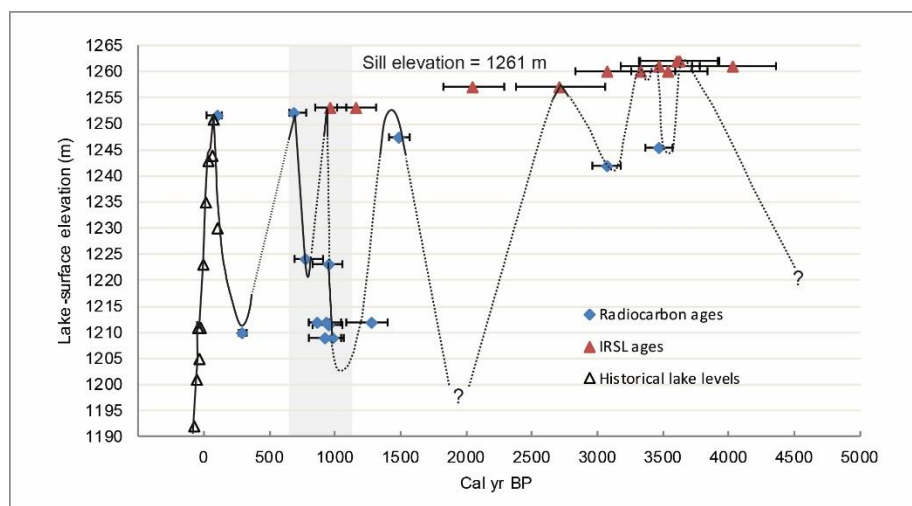

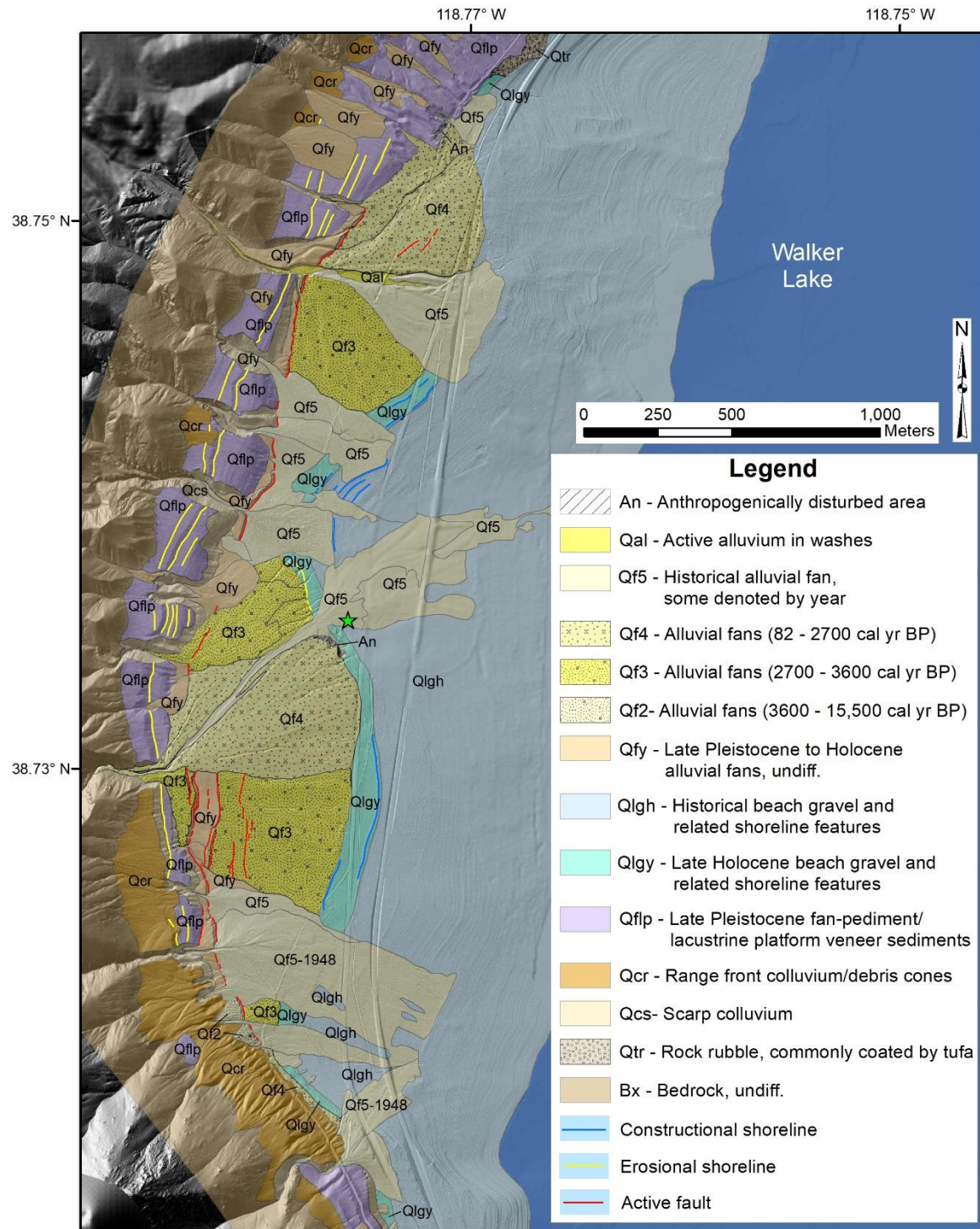Figure 1. Late Holocene Walker Lake-level curve. Modified from Adams and Rhodes (2019b).

Figure 2. Geologic map of the Copper Canyon embayment showing the relations between shorelines, alluvial fans, and faults. The green star is where the stop will start.

Here in the Copper Canyon embayment, the 1257 m shoreline represents the highest visible late Holocene shoreline because Qf3 fans have completely wiped out or buried any shorelines that had formed between 1257 – 1262 m (Figure 2). Mapping the spatial distribution of alluvial fans surrounding Walker Lake indicates that alluvial fan activity was not only widespread in this embayment between about 2700 – 3600 cal yr BP, but that Qf3 fans cover a greater percentage of the piedmont within the mapping area than any other fan unit, including Qf2 fans that were deposited over a much longer period of time between 3600 – 15,500 cal yr BP (Adams, 2019).

Sporadic alluvial fan activity has continued up to the present with notable debris flow events emanating from Copper Canyon in 1982, 1990, and as recently as 2014. In the latter event, about 40 – 50 mm of rain fell in about 1.5 hours in the headwaters of Copper Canyon, triggering the hyperconcentrated flow deposit that is still visible along the main channel of the Copper Canyon fan. It is reasonable to assume that the coarser, more bouldery young fans in this embayment were caused by more intense precipitation events.

Faulting in the embayment is expressed by primarily north-south striking discontinuous scarps of the east-dipping Wassuk Range front fault system (Figure 2). A series of antithetic faults define a relatively small graben on the south side of the Copper Canyon fan (Qf3). A younger lobe of a Qf4 fan, however, has buried or otherwise obliterated the graben to the north. A radiocarbon sample that returned an age of 675 ± 30 ^{14}C yr BP (560 – 678 cal yr BP) was collected from fine-grained strata here in the gravel pit at the distal end of the Copper Canyon fan. This organic carbon sample was from a fine-grained silty unit that may have been ponded behind the 1257 m shoreline. The fine-grained unit overlies a relatively thick tephra unit that probably represents one of the Mono Crater tephras (Adams, 2007) but was subsequently buried by at least two debris flow units, the upper of which represents the Qf4 fan surface. Therefore, the Qf4 unit is less than about 650 cal yr BP at this location. Based on the age constraints of the Qf4 and Qf3 fan units here, the age of the most recent ruptures on the Copper Canyon fan is older than about 650 cal yr BP but younger than 3600 cal yr BP. Two small scarps were mapped on a Qf4 fan about 2 km north of Copper Canyon, suggesting a younger event may have occurred between 82 – 2700 cal yr BP. These results are broadly consistent with those of Wesnousky (2005) and Bormann et al. (2012).

An important point to make here about the mapping of this embayment is that the bases of several scarps are buried by historical alluvial fans (Qf5), deposited during a time when there were no ground-rupturing earthquakes. These historical fans are in depositional contact through buttress unconformities with the scarps and do not necessarily provide tightly constrained estimates of the timing of the most recent event. These types of relations may be more difficult to assess on other piedmonts across the Great Basin, particularly where there are no dated shorelines to guide one's efforts.

References

Adams, K.D., 2007, Late Holocene sedimentary environments and lake-level fluctuations at Walker Lake, Nevada, USA: Geological Society of America Bulletin v. 119, no. 1 and 2, p. 126-139.

Adams, K.D., 2019, Constraining the timing, magnitude, and spatial distribution of Holocene alluvial fan activity at Walker Lake, NV using dated shorelines: Geological Society of America Abstracts with Programs, v. ?, no. ?, p. ?, presented in Phoenix, AZ.

Adams, K.D., and Wesnousky, S.G., 1998. Shoreline processes and the age of the Lake Lahontan highstand in the Jessup embayment, Nevada: Geological Society of America Bulletin v. 110, p. 1318–1332.

Adams, K.D., and Rhodes, E.J., 2019a, Late Pleistocene to present lake-level fluctuations at Pyramid and Winnemucca lakes, Nevada, USA: Quaternary Research, v. 92, p. 146-164.

Adams, K.D., and Rhodes, E.J., 2019b, Late Holocene paleohydrology of Walker Lake and the Carson Sink in the western Great Basin, Nevada, USA: Quaternary Research, v. 92, p. 165-182.

Bacon, S.N., Lancaster, N., Stine, S., Rhodes, E.J., McCarley Holder, G.A., 2018, A continuous 4000-year lake-level record of Owens Lake, south-central Sierra Nevada, California, USA: Quaternary Research, v. 90, no. 2, p. 276-302.

Bormann, J.B., Surpless, B.E., Caffee, M.W., and Wesnousky, S.G., 2012, Holocene earthquakes and late Pleistocene slip-rate estimates on the Wassuk Range fault zone, Nevada: Bulletin of the Seismological Society of America, v. 102, no. 4, p. 1884-1891.

Wesnousky, S.G., 2005, Active faulting in the Walker Lane: Tectonics, v. 24 TC3009, doi:10.1029/2004TC001645, 35 p.

2.4.2 Time Scales and Processes of Shoreline Formation at Walker Lake, Nevada

Noah Abramson[1] and Kenneth D. Adams[2]

[1]Graduated MS Student, Department of Geological Sciences and Engineering, University of Nevada, Reno

[2]Desert Research Institute, 2215 Raggio parkway, Reno, Nevada 89512-1095, USA

Past lake levels in pluvial lakes are often recorded in the form of distinct shoreline deposits, these features have been used for over a century to document paleoclimatic fluctuations, paleohydrology, and tectonic deformation in the western U.S. (e.g., Russell, 1885; Mifflin and Wheat 1979; Adams et al., 1999; Oviatt, 2015). Despite the prominence and marked geomorphic characteristics of shoreline deposits formed in pluvial lakes, little to no research has been done to quantify the rate at which these features form. A variety of time scales are often suggested for shoreline formation from months to years (e.g., Adams and Wesnousky, 1998), decades (e.g., Thompson and Baedke, 1995), to hundreds or even thousands of years (e.g., Oviatt, 2015), however much of this evidence is more qualitative quantitative.

At Walker Lake, a sequence of well- developed shoreline deposits has formed during the historical lake-level regression (Figure 1). The unique hydrologic setting of Walker Lake, high resolution imagery, and detailed lake level records from the region allows us to examine the relationship between beach ridge volume and the time of formation. The volume vs. time of formation relationship observed on historical shorelines is then applied to estimate the duration of time that the 1262 m Late Holocene highstand persisted at Walker Lake.
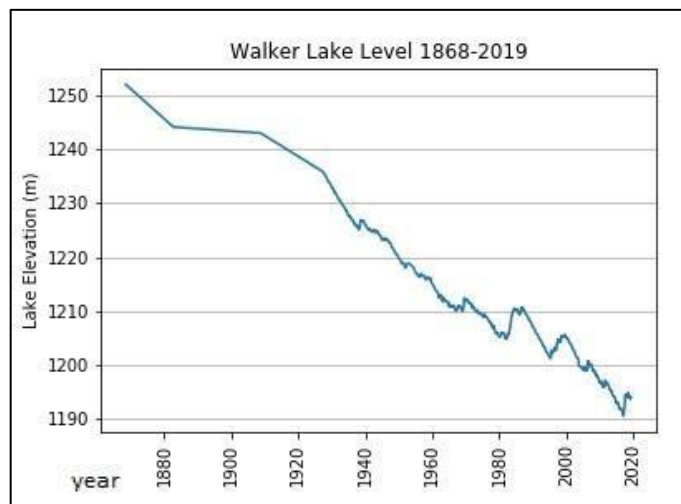

Figure 1: Lake surface elevation of Walker Lake from 1868-2019. Data from Walker Lake USGS gauge near Hawthorne, NV.

Regional Hydrology and Historical Shorelines

Since the late 19th century, upstream anthropogenic water diversions from the Walker River as well as regional droughts have caused a dramatic decrease in lake levels at Walker Lake (Figure 1). As lake surface elevation regressed from the 1252 m historical highstand, a suite of prominent shoreline features were formed and subsequently abandoned as lake level continued to drop to its current elevation of ~1194 m (start of the 2019 water year). The historical lake-level record in Walker Lake consists of sporadic documentation beginning in 1868 (Russell, 1885) which ultimately became monthly in 1928 (Figure 1). For this study, we focus on a suite of well-developed historical beach ridges located at the NW corner of Walker Lake between 1244-1202 m elevation.

Estimated Volumes and Rates of Shoreline Formation

Individual beach ridges were mapped in ArcGIS by determining the shoreward and landward base of each beach ridge, and then a high-resolution Digital Elevation Model (DEM) was clipped to the individual polygons. The various base and crestal elevations of a single beach ridge were measured along strike and averaged along its entire length, than the volume above average base elevation was calculated. The length of the beach ridge was measured along strike and the total volume was then divided by total length to estimate the average volume per unit length (m^3/m) for an individual feature. As validation for the modeled volumetric values, measurement of several beach ridge profiles was performed at Walker Lake with a stadia rod and hand level. Mean variance between field-estimated values and modeled values is 0.2 m^2, which is consistent with the natural variability of shoreline features as well as the horizontal and vertical accuracy of the DEMs used.

Observations made at Sand Harbor Beach, Lake Tahoe during a ~10 m/s wind event sustained for 7 hours in March of 2019 showed fresh pine needles and gravel to have washed to the crestal limit of the active beach ridge, supporting previous studies who have proposed the height of beach ridges represents the uppermost limit of wave swash for a given beach (e.g., Tamura et al., 2018; Wang et al., 2018).

Average beach ridge height and total wave runup modeled for NW Walker Lake are ~ 0.5 m, indicating typical wave swash elevations during beach ridge formation achieve 0.5 m in height above still water lake-level. Since the geomorphic work that creates these features is done during periods where lake-level is temporarily superelevated, the still-water lake elevation does not correspond directly to the same elevation range of the beach ridge feature. To compensate for this in the lake-level residency time estimates, we placed the range of still water lake-levels associated with a beach ridge between the base elevation to 0.5 m below crestal height. Using data obtained from the Walker Lake USGS gauge near Hawthorne, NV we summed the number of days that fell within this range of elevations. This method of relating still water lake-levels and beach ridge height is based on observed wave events, modeled wave environments from regional wind data, and beach ridge morphology, therefore, most likely reflecting the underlying process that leads to beach ridge genesis.

Using the methods described above, twenty-six individual beach ridges were analyzed within the elevation range of 1244 - 1202 m along the NW shore of Walker Lake. Based on the historical lake-level curve, these features are estimated to have formed between the years ~1920 - 2000. Volumes estimated in this suite of beach ridges ranges from 0.3 - 6 m^3/m with an average beach ridge volume of 2.5 m^3/m (Figure 2). The time scales under which these features formed ranges from ~120 - 1000 days (Figure 2).
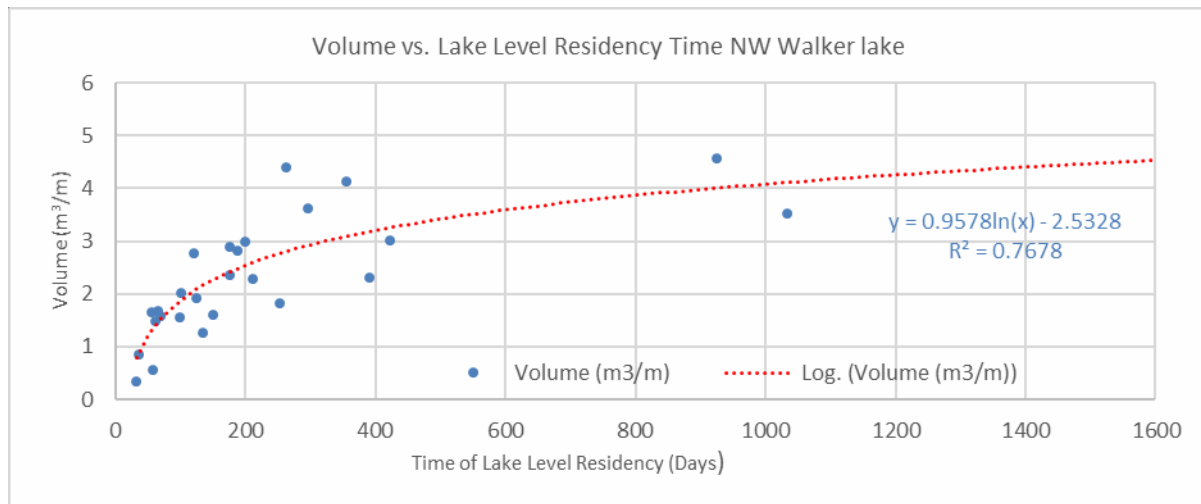
Figure 2: Results of volume of beach ridges vs. time of lake-level residency at their corresponding elevations along the NW margins of Walker Lake

Estimated rates of accumulation ranged from ~1 - 5 m^3/m of beach ridge material per year. Differences in rates of development can largely be attributed to annual flux in wave energy (related to number of large wind events), or differences in sediment supply (e.g. locations of deltas or active washes). At Walker Lake, the increase in shoreline volume appears to stabilize within ~3 years (Figure 2). This suggests an equilibrium state of development may be achieved in that time, given the wave energy regime and sediment supply at the locations studied.

Several of the historical beach ridges at Walker Lake contain ~ 2 m wide stream channel cuts exposing the internal stratigraphy of these features. In cross-sectional view these features display faint horizontal, even, parallel, and continuous alignment of dark minerals interpreted to be bedding features. Tamura et al. (2018) demonstrated on marine coasts that beach ridges formed over multiple storm surge events spanning several decades would commonly display erosive sedimentary structures such as hummocky-cross bedding. Therefore, the intact bedding features at Walker Lake are interpreted to indicate the beach ridges were formed during the most recent lake-level cycle.

The beach ridges found at the NW Walker Lake site are commonly composed of sand-gravel sized grains with abundant pebble-cobble sized clasts 3-5 cm in diameter. The coarse nature and absence of dune or asymmetrical ripple features suggests aeolian contributions to these features are minimal; therefore, it is reasonable to assume the volume of material measured was emplaced by wave energy expended on the shoreline.
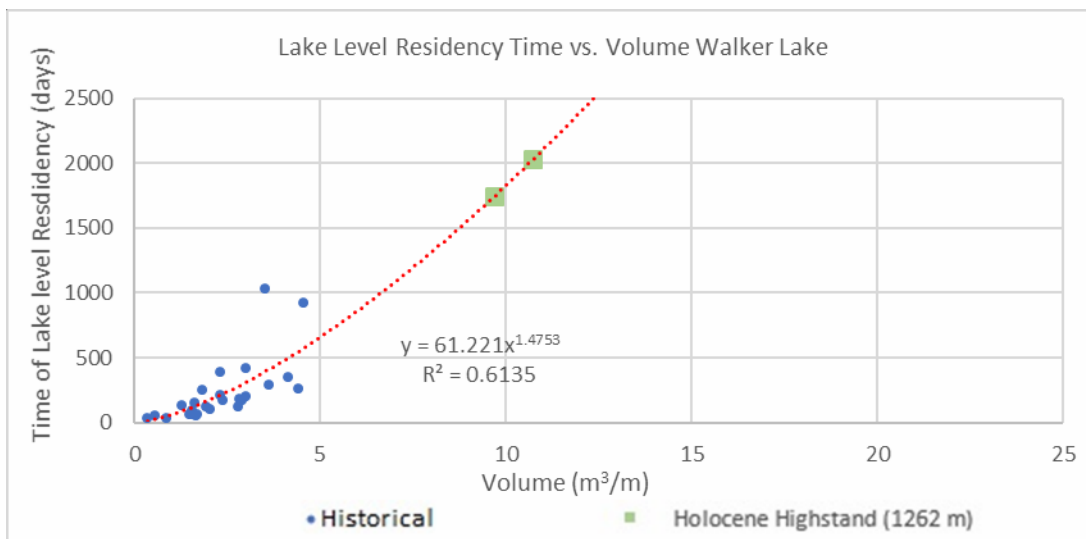
Figure 3: Estimates of times of formation for Late Holocene beach ridges (Green) based on volume vs. time relationship developed on historical beach ridges at Walker Lake (Blue). Note: power law function used to estimate times of lake-level residency for the late Holocene highstand.

Applying Volumetric Analysis to Paleoshorelines: Late Holocene Highstand at Walker Lake

Beach ridges representing the late Holocene highstand at Walker Lake are located at ~1262 m elevation. IRSL dates by Adams and Rhodes 2019b indicate an age ~3620 $\pm$ 300 cal yr BP for these features. The volume of the 1262 m beach ridge was measured at three different locations at the North end of Walker Lake. Large variability was observed in beach ridge volume along strike of the 1262 m highstand with values ranging from 9.67-33.44 m^3/m with a prominent increase in volume to the NE.

The strong correlation between time of formation and increased volume observed on the historical beach ridges indicates the volumes of beach ridges maybe used as an indicator to infer relative durations of lake-level stability. A logarithmic equation was fit to the observations made on historical shorelines at Walker Lake (Figure 2) and applied to observed volumes of the Late Holocene Highstand beach ridge at Walker Lake. When applied to the Late Holocene shorelines, the original shoreline growth model yielded lake-level residency estimates from. ~937 - 2823 years. These estimates disagree with IRSL ages placed on a 1241 m shoreline ~3000 cal yr BP by Adams and Rhodes (2019b).

Fetch distances are considerably larger for Walker Lake at a lake surface elevation of 1262 m (~43 km fetch) than they are where the historical shorelines are measured (~17-18 km fetch), this would result in significantly larger waves affecting the shoreline during the late Holocene. Additionally, due to its proximity to the mouth of the Walker River it is suspected that the location studied had a much larger sediment budget than the historical site. Therefore, the ~3-year shoreline equilibrium observed in the historical beach ridges at Walker Lake likely does not reflect the development rates that would have occurred in late Holocene Walker Lake. As a result, a power law equation was fit to the data collected at the historical beach ridges (Figure 3). This equation does not result in a relatively quick equilibrium state for rates of shoreline development and is believed to better represent the rates of development that would have occurred at the Holocene highstand beach ridge. Using this relationship and the observed volumes, the estimates for duration of a sustained 1262 m lake level are ~4 - 29

years, with two estimates suggesting a lake-level residency time of ~4 - 5 years (Figure 3). It is likely the 29 year estimate is skewed by an anomalously large portion of the beach ridge located in close proximity to the Walker River.

It is important to acknowledge that an equilibrium state of beach ridge development could have been achieved during the formation of the 1262 m beach ridge, and lake levels could have been sustained for longer periods of time than our current estimate suggests. Therefore, the 4 - 29 year estimate may only represent a minimum duration estimation of the late Holocene highstand at Walker Lake.

Conclusion

The volumetric analysis of historical beach ridges at Walker Lake showed a strong correlation between time of formation and increased volume, which indicates at minimum, the individual volumes of beach ridges may be used as an indicator to infer relative durations of lake-level stability. Furthermore, when used to estimate durations of time of lake-level stability, this presents a new technique to refine pre- historic lake-level curves on an annual-decadal scale. Importantly, given large variability in shoreline volumes along strike and across basins it is imperative to acknowledge differences in sediment supply, wind conditions, wave energy, shoreline equilibrium, and other parameters relating to beach ridge formation before applying volumetric relationships from one lake to another or across different lake stages.
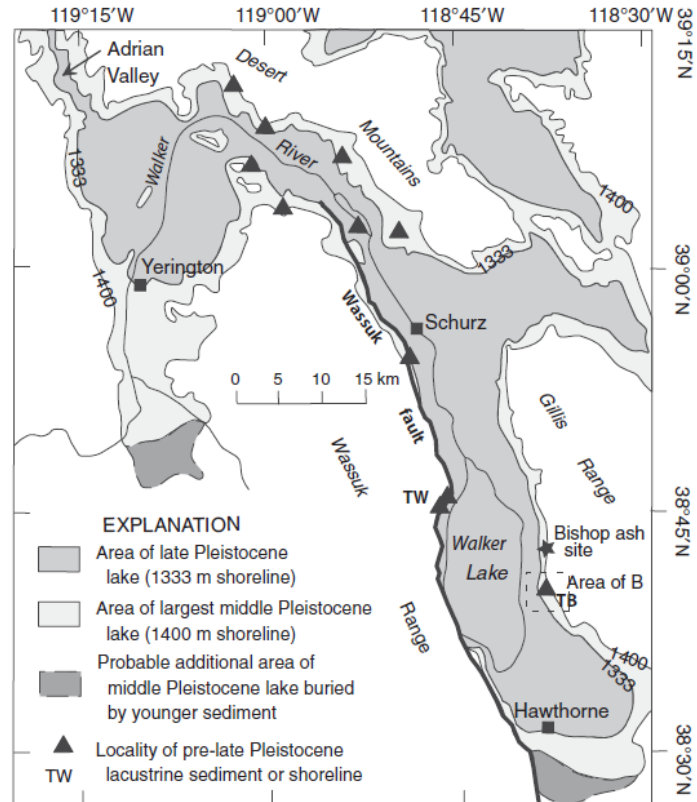
References

Adams, K. D., Rhodes, E. J., 2019b, Late Holocene paleohydrology of Walker Lake and the Carson Sink in the western Great Basin, Nevada, USA. Quaternary Research, 1–18. https://doi.org/10.1017/qua.2018.151

Adams, K. D, Wesnousky, S. G., 1998. Shoreline Processes and the age of the Lake Lahontan highstand in the Jessup embayment, Nevada. Geological Society of America Bulletin, (110)10, p. 1318-1332.

Adams, K. D, Wesnousky, S. G., & Bills, B. G., 1999. Isostatic rebound, active faulting, and potential geomorphic effects in the Lake Lahontan basin, Nevada and California.   Geological Society of America Bulletin, (111)12, p. 1739–1756.

Mifflin, M.D., Wheat, M.M., 1979, Pluvial lakes and estimated pluvial climates of Nevada. Bulletin- Nevada Bureau of Mines and Geology, (94), 57 p.

Oviatt, C. G. 2015, Chronology of Lake Bonneville, 30,000 to 10,000 yr BP. Quaternary Science

Reviews, 110, 166–171. https://doi.org/10.1016/j.quascirev.2014.12.016

Russell, I.C., 1885, Geological history of Lake Lahontan, a Quaternary lake in northwestern Nevada, U.S. Geological Survey Monograph 11, 288 p.

Tamura, T., Nicholas, W. A., Oliver, T. S. N., & Brooke, B. P., 2018, Coarse-sand beach ridges   at Cowley Beach, north-eastern Australia: Their formative processes and potential as records of tropical cyclone history. Sedimentology, 65(3), 721–744. https://doi.org/10.1111/sed.12402

Thompson, T. A., & Baedke, S. J., 1995, Beach-ridge development in Lake Michigan: shoreline behavior in response to quasi-periodic lake-level events. Marine Geology, 129(1–2), 163–174. https://doi.org/10.1016/0025-3227(95)00110-7

Wang, J., Jiang, Z., Xian, B., Chen, J., Wang, X., Xu, W., & Liu, H. 2018. A method to define the palaeowind strength from lacustrine parameters

. Sedimentology, 65(2), 461–491. https://doi.org/10.1111/sed.12388

2.4.3   Uplifted beach gravel of Walker Lake (Lake Lahontan)

Marith Reheis

The Walker Lake basin is a subbasin of Lake Lahontan and preserves a >2-Myr record of lacustrine deposition (Morrison, 1991; Reheis et al., 2002; Kurth et al., 2011). At least two localities preserve pre-Sehoo (MIS 2) beach gravels along the Wassuk Range front (map below). These localities are at much higher altitudes than most other sites in the Walker Lake subbasin. The site that is visible from this field trip stop is about 1.5 km to the north, and due west of Twentymile Beach. It exposes four beds of beach gravel (gray) interbedded with fan gravel (oxidized) above the Sehoo shoreline; the highest beach gravel caps a ridge at 1475 m (photo below). The second site is 3 km north of 20-Mile Beach and has two levels of tufa-cemented beach gravel (photos on next page), both of which have been dated by U-series. The lower level is a moderately preserved wave-cut bench overlain by 1-2 m of tufa-cemented beach rock; it extends up to an altitude of about 1400 m and yielded ages of 147±2 ka and 133±5 ka. These ages are consistent with a U-series age of 128±6 ka and a ^{36}Cl depth profile age of 118 $^{+68}$/-18 ka on a well-preserved beach barrier at Thorne Bar (NE of Hawthorne, NV), which records a highstand at ~1450 m in a tectonically quiescent area. Assuming these two sites record the same highstand, they indicate ~50 m of relative uplift of the Wassuk footwall since about 130 ka (MIS 6). The upper level is an eroded remnant of beach


EXPLANATION

- Area of late Pleistocene lake (1333 m shoreline)
- Area of largest middle Pleistocene lake (1400 m shoreline)
- Probable additional area of middle Pleistocene lake buried by younger sediment
- ▲ Locality of pre-late Pleistocene lacustrine sediment or shoreline
- TW

Sketch map of Walker Lake subbasin of Lake Lahontan modified from Reheis et al. (2002). TW—site of dated tufa samples EL97–4 and EL97–5 on footwall block of Wassuk fault near Twentymile Beach. TB—area of Thorne Bar. Star showing 760-ka Bishop ash locality described in Reheis et al. (2002).

View to northwest of uplifted pre-Sehoo beach gravels ~1.5 km north of Copper Canyon.

rock with bright orange oxidation and with foreset beds overlying sheared granitic rocks; the highest outcrop of beach rock is at 1452 m. This elevation is 50 m higher than the highest known beach gravels at Thorne Bar and sites to the north, provisionally correlated with MIS 16 (660-620 ka). U-series ages from this site yielded problematic results that are interpreted to indicate loss of U by post-depositional leaching (Kurth et al., 2011).
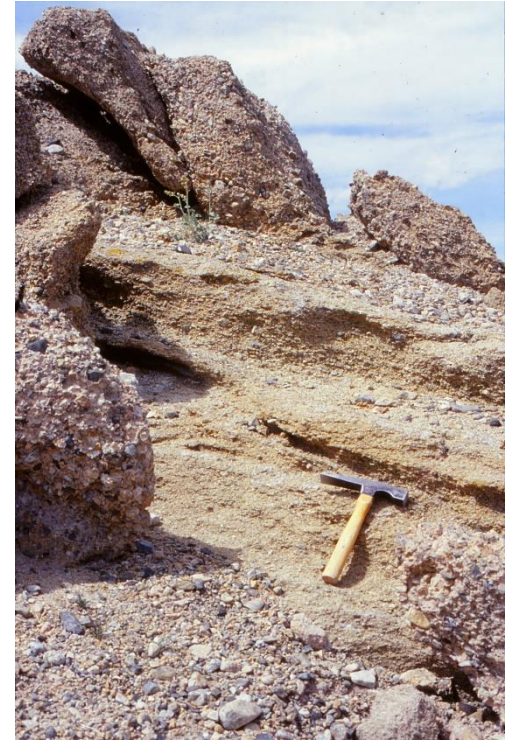
Photos of tufa-cemented beach gravel dated with U-series, 3 km north of Twentymile Beach. Above in foreground, MIS-6 beach uplifted 50 m (1400 masl, 50 m higher than same gravels at Thorne Bar). Background, older, eroded beach rock remnant extends up to 1452 masl. Photo to right is closeup of this older remnant showing beach foresets and oxidation.

Kurth, G., Phillips, F. M., Reheis, M. C., Redwine, J. L., and Paces, J. B., 2011, Cosmogenic nuclide and uranium-series dating of old, high shorelines in the western Great Basin, USA: Geological Society of America Bulletin, v. 123, no. 3-4, p. 744-768.

Morrison, R.B., 1991, Quaternary stratigraphic, hydrologic, and climatic history of the Great Basin, with emphasis on Lakes Lahontan, Bonneville, and Tecopa, in Morrison, R.B., ed., Quaternary Nonglacial Geology: Conterminous U.S.: Boulder, Colorado, Geological Society of America, The Geology of North America, v. K-2, p. 283–320.

Reheis, M. C., Sarna-Wojcicki, A. M., Reynolds, R. L., Repenning, C. A., and Mifflin, M. D., 2002, Pliocene to middle Pleistocene lakes in the western Great Basin: Ages and connections, in Hershler, R., Madsen, D. B., and Currey, D. R., eds., Great Basin Aquatic Systems History: Smithsonian Contributions to the Earth Sciences: Washington, D.C., Smithsonian Institution Press, p. 53-108.

2.5 North Canyon

2.5.1　North Canyon Overview

Ian Pierce

North of Lucky Boy pass are a series of north-striking grabens and prominent vertical fault scarps (**Figure 1d**). From Lucky Boy pass to the southeast is a linear northwest striking linear fault segment that extends for ~10 km. The first ~3 km of this fault segment forms a north facing fault scarp along the rangefront. The strike-slip fault trace then continues to the southeast linearly away from the rangefront forming subdued uphill-facing fault scarps. The remainder of this fault segment forms two fault traces that form south and north facing scarps and a prominent pop-up, pressure ridge-like feature of uplifted bedrock, fan, and pediment surfaces. South from here the fault bends to the southeast more and forms subdued scarps in a large distal fan, before again forming a second popup feature, similar in scale to the first. The rangefront southward from here is more northerly striking and forms a number of east facing scarps at canyon mouth drainages. The faulting mapped along a portion of the rangefront in **Figure 1d** is an example of strain partitioning: where a basin-ward strike-slip fault is separated from a rangefront normal fault.

This site (North Canyon) has an apparent right lateral offset of a large drainage, however a scarp that is outboard of the rangefront and head of the beheaded channel raises the question of whether this offset is tectonic or a result of normal alluvial fan processes. The beheaded channel is "offset" ~60 m from the active channel.

- Is this a suitable lateral slip rate site?
- Were the vertical scarp in the fan eroded flat or otherwise obscured, would you use this as a slip rate site?
- Are there any issues with dating this surface?
- If the ~1 mm/yr slip rate from near Schurz applies here, then the 60 m offset surface should be ~60 ka. Is this reasonable (based on soils exposed in the wash, weathering of boulders, appearance of surface, etc.)?
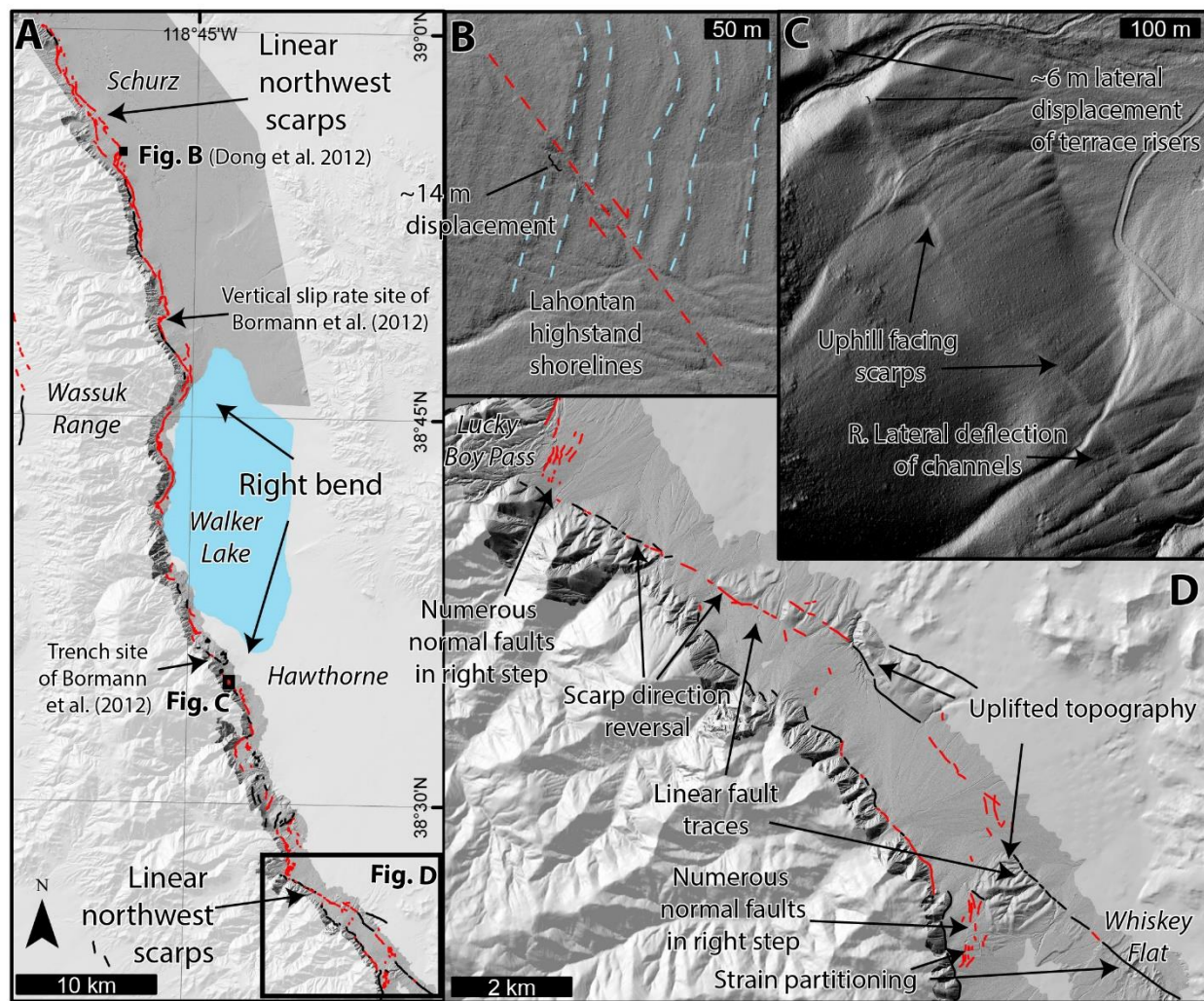
Figure 1 Fault map (a) of the Wassuk fault zone. Lidar hillshades are darker gray, light gray background is a hillshaded 10 m DEM. Red lines are fault scarps in alluvial deposits, black are inferred and/or bedrock-alluvial fault contacts. The fault geometry forms two northwest striking segments separated by a large right step coincident with Walker Lake and the deepest part of the basin. The northwest striking segments contain alternating scarp directions, linear scarps, and right-lateral displacements, all consistent with strike-slip faulting. Right-stepping segments locally exhibit greater degrees of normal faulting. Locations of (b-d) are indicated on (a). (b) Blowup of site from Dong et al. (2014) showing 14 m right-lateral displacement of ~14.5 ka Lahontan shorelines with slip rate of ~1 mm/yr. (c) Segment of fault near Hawthorne where an uphill facing linear scarp deflects a number of channels and offsets a pair of terrace risers ~6 m. (d) shows the southern portion of the Wassuk fault zone. Here strain is partitioned into a linear basin-ward strike-slip fault and a normal fault against the range.
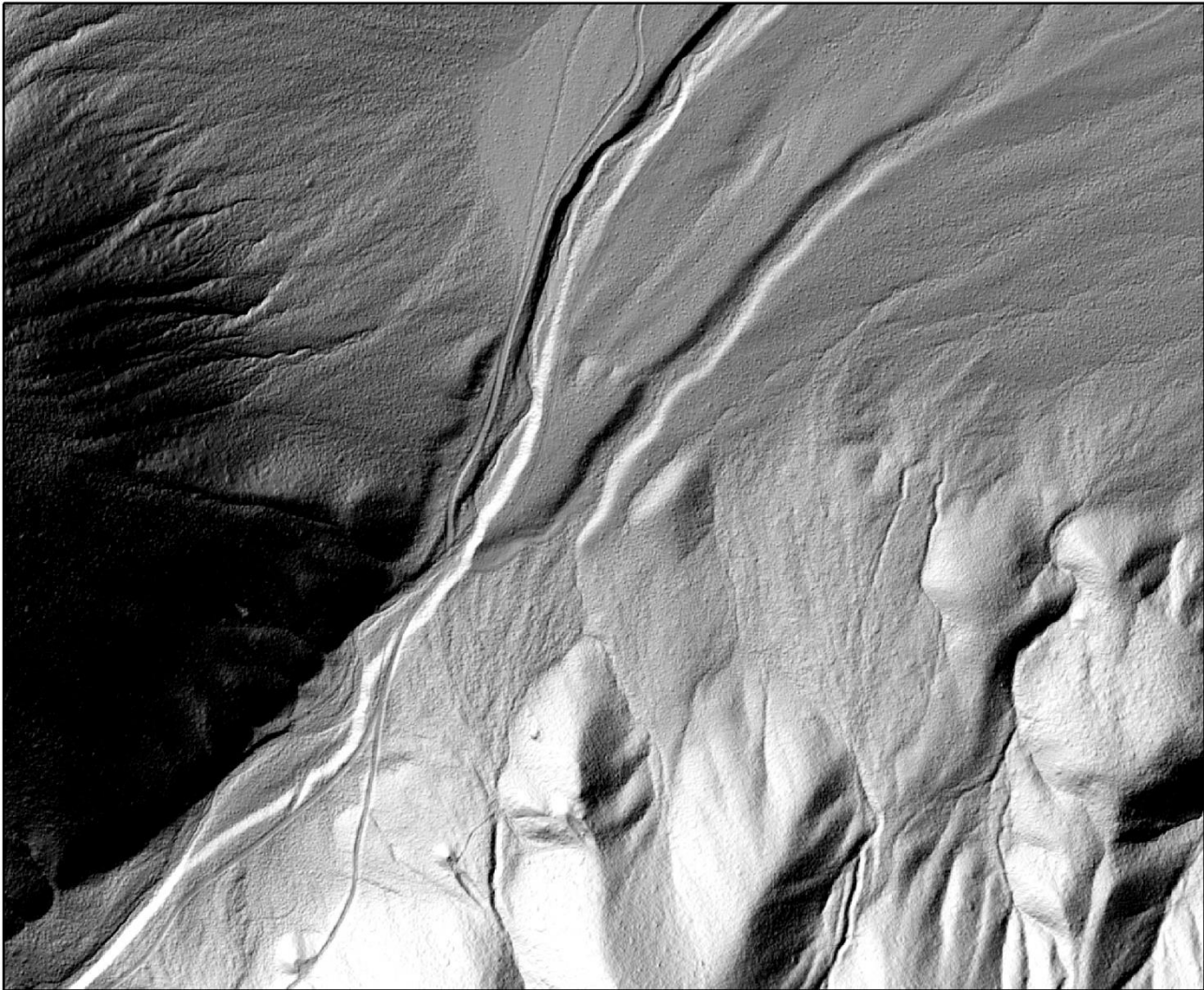
Figure 2 – blowup of North Canyon (this stop)

2.5.2 The Tectonic Revolution: Enigmatic Dextral Shear Accommodation within Regions of Vertical-Axis Rotating Crust, Western Central Walker Lane

Chad W. Carlson, Independent Geologic Consultant, Reno, NV, 89503

Introduction

A region of northerly-striking normal faults and asymmetric basins resides west of the central Walker Lane and south of the northern Walker Lane, where geodetic studies define northwest-directed dextral strain devoid of major strike-slip fault systems (Figure 1). Paleomagnetic study of Cenozoic rocks in parts of the central and northern Walker Lane have been used to: verify domains of translating crust associated to dextral fault systems (e.g., Faulds et al., 2004; Carlson, 2017); identify domains of crust undergoing clockwise (CW) vertical-axis rotation associated to sinistral fault systems (e.g., Cashman and Fontaine, 2000; Petronis et al., 2009); and more recently, identified similarly CW-rotated regions that are devoid of the prominent strike-slip faults indicative of the Walker Lane (e.g., King et al., 2007; Rood et al., 2011, Carlson et al., 2013, Carlson 2017). As part of the greater discussion of the extensive paleomagnetic data collected from the northern and central Walker Lane, a brief description of two enigmatic regions of documented CW vertical-axis rotations with different tectono-physiographic responses are presented below. This is followed by a comparison of geodetic and geologic data.

Mason Valley, NV

Positioned west of the dextral faults of the central Walker Lane are normal-faulted basins and highly extended terrain where geodetics (GPS station velocities) measure ~5-7 mm/yr of dextral shear (Wesnousky, et al., 2012). Paleomagnetic study of Oligocene ash-flow tuffs in Mason Valley has documented heterogeneous block rotations of up to ~30-40° CW in partial response to this regional dextral shear (Fig. 1; Carlson, 2017). Early, large-magnitude extension and basin development of Mason Valley likely set the stage for later transtensional deformation and dextral shear accommodation via vertical-axis rotation of crust (e.g., Proffett, 1977; Surpless, 2008). The multiple generations of normal faults across the valley produced fine-scale, relative to the basin-bounding ranges, tectonic blocks that responded favorably to rotation rather than translation. Additionally, finer-scale (<<10 km) blocks of crust are more accommodating of large-magnitudes of rotation than the regional-scale (>10 km) block models commonly invoked for kinematic interpretation of regions undergoing vertical-axis rotations (e.g., the Carson domain of sinistral faults in the northern Walker Lane and regions discussed below). Although CW vertical-axis rotations are indicative of dextral shear accommodation across Mason Valley, the highly extended and basin fill make it difficult to quantify the magnitude of relative motion.

Bridgeport and Antelope Valleys, CA (Sweetwater Mts. and Bodie Hills)

Unlike the CW rotations documented between the major ranges bounding Mason Valley (i.e., Singatse and Wassuk), sites of paleomagnetically-documented rotation are located within the Sweetwater Mts. and Bodie Hills physiographic blocks that bound Bridgeport and Antelope Valleys (Fig. 1; Carlson et al., 2013). Consistent with the asymmetric basin hypothesis of Wesnousky et al. (2012), the openings of the valleys appear to mimic the ~30 degrees of CW vertical-axis rotation averaged for the Sweetwater Mts. and Bodie Hills. Carlson et al. (2013) hypothesize that the wedge shapes of these asymmetrical depositional basins may have been controlled by differential slip along basin bounding faults in the transtensional tectonic regime.

Geodetic vs. Geologic Rotations

To compare geodetically-predicted to paleomagnetically-determined rotations the preferred model of Bormann et al. (2016) is overlain by new and previously-published paleomagnetic data (Figure 2). Although the geodetic data predict rates of vertical-axis rotation, paleomagnetically-determined magnitudes of rotation are spatially consistent to geodetic block translation vs. rotation with little modification to previously-defined boundaries of structural domains or regions. Those rotated localities that are inconsistent with geodetic block predictions are commonly positioned near block boundaries that back well-defined surface traces of regional faults.

References

Bormann, J., Hammond, W.C., Kreemer, C., and Blewitt, G., 2016, Accommodation of missing shear strain in the Central Walker Lane, western North America: Constraints from dense GPS measurements: Earth and Planetary Science Letters, v. 440, p. 169-177, doi:10.1016/j.epsl.2016.01.015.

Carlson, C.W., Pluhar, C.J., Glen, J.M.G, and Farner, M.J., 2013, Kinematics of the west-central Walker Lane: Spatially and temporally variable rotations evident in the late Miocene Stanislaus Group: Geosphere, v. 9; no. 6; p. 1-22; doi:10.1130/GES00955.1.

Carlson, C.W., 2017, Kinematics and Transfer Mechanisms of Strain Accommodation at the Transition between the Northern and Central Walker Lane, Western Nevada [Ph.D. dissertation]: University of Nevada, Reno, 220 p.

Cashman, P.H., and Fontaine, S.A., 2000, Strain partitioning in the northern Walker Lane, western Nevada and northeastern California: Tectonophysics, v. 326, p. 111-130.

Faulds, J.E., Henry, C.D., Hinz, N.H., Delwiche, B., and Cashman, P.H.,2004, Kinematic implications of new paleomagnetic data from the northern Walker Lane, western Nevada: Counterintuitive anticlockwise vertical-axis rotation in an incipient dextral shear zone: EOS, Transactions, American Geophysical Union, v. 85, no. 47, Abstract GP42A-08.

Ferranti, L., Oldow, J.S., Geissman, J.W., and Neil, M.M., 2009, Flattening strain during coordinated slip on a curved fault array, Rhodes Salt Marsh extensional basin, central Walker Lane, west-central Nevada, in Oldow, J.S., and Cashman, P.H., eds., Late Cenozoic structure and evolution of the Great Basin-Sierra Nevada transition: Boulder, Colorado, Geological Society of America Special Paper 447, p. 189-214.

Geissman, J.W, Van Der Voo, R., and Howard, K.L., Jr., 1982, A paleomagnetic study of the structural deformation in the Yerington district, Nevada: American Journal of Science, v. 282, p. 1042-1109.

King, N.M., Hillhouse, J.W., Gromme, S., Hausback, B.P., and Pluhar, C.J., 2007, Stratigraphy, paleomagnetism and anisotropy of magnetic susceptibility of the Miocene Stanislaus Group, central Sierra Nevada and Sweetwater Mountains, California and Nevada: Geosphere, v. 3, no. 6, p. 646–666, doi: 10.1130/GES00132.1.

Petronis, M. S., Geissman, J. W., Oldow, J. S., and McIntosh, W. C., 2009, Late Miocene to Pliocene vertical-axis rotation attending development of the Silver Peak-Lone Mountain displacement transfer zone, west-central Nevada, in Oldow, J. S., and Cashman, P. H., eds., Late Cenozoic structure and evolution of the Great Basin-Sierra Nevada transition: Boulder, CO, Geological Society of America Special Paper 447, p. 215-254.

Pluhar, C.J., Deino, A.L., King, N.M., Busby, C., Hausback, B.P., Wright, T., and Fisher, C., 2009, Lithostratigraphy, magnetostratigraphy, and radiometric dating of the Stanislaus Group, CA, and age of the Little Walker Caldera: International Geology Review, v. 51, p. 873–899, doi: 10.1080/00206810902945017.

Proffett, J.M., Jr., 1977, Cenozoic geology of the Yerington district, Nevada, and implications for the nature and origin of Basin and Range faulting: Geological Society of America Bulletin, v. 88, p. 247–266.

Rood, D.H., Burbank, D.W., Herman, S.W., and Bogue, S., 2011, Rates and timing of vertical-axis block rotations across the central Sierra Nevada-Walker Lane transition in the Bodie Hills, California/Nevada: Tectonics, v. 30, 23 p., doi: 10.1029/2010TC002754.

Surpless, B.E., 2008, Modern strain localization in the central Walker Lane, western United States: Implications for the evolution of intraplate deformation in transtensional settings: Tectonophysics, v. 457, p. 239–253, doi: 10.1016/j.tecto.2008.07.001.

Surpless, B.E., 2011, Cenozoic tectonic evolution of the central Wassuk Range, western Nevada, USA.: International Geology Review, v. 54, no. 5, p. 547–571, doi: 10.1080/00206814.2010.548117.

Wesnousky, S.G., Bormann, J.M., Kreemer, C., Hammond, W.C., and Brune, J.N., 2012, Neotectonics, geodesy, and seismic hazard in the northern Walker Lane of western North America: Thirty kilometers of crustal shear and no strike slip?: Earth and Planetary Science Letters, v. 329–330, p. 133–140, doi: 10.1016/j.epsl.2012.02.018.
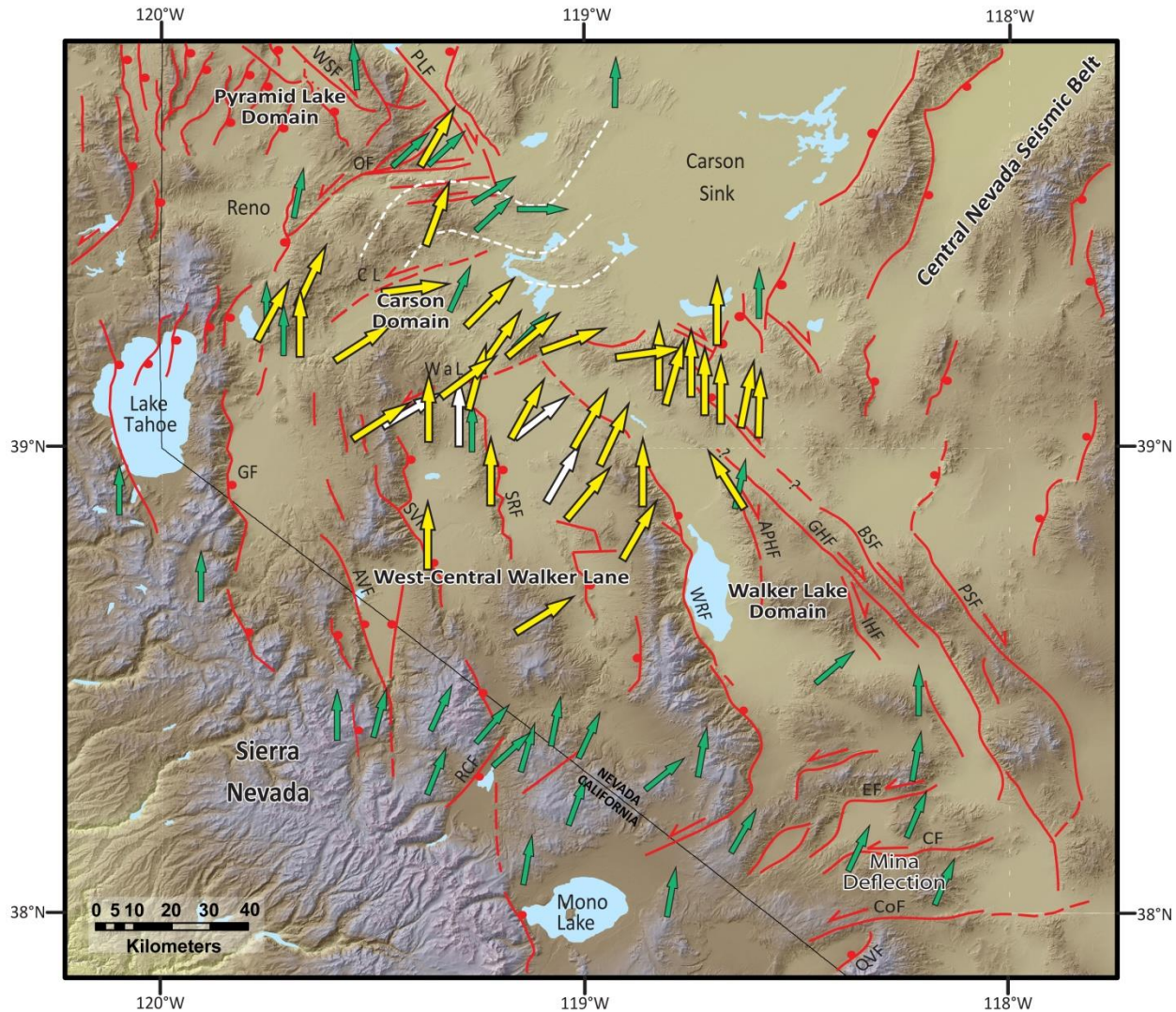
Figure 1. *Colored shaded-relief map of the transition region between the central and northern Walker Lane, modified from Carlson et al. (2013). Major faults and lineaments modified from Faulds and Henry (2008). Vertical-axis rotations are shown by arrows; due north orientation represents no rotation, with relative amounts of rotation indicated by arrow deflection from north. Rotations deduced in this study are shown by yellow arrows. Re-evaluated paleomagnetic site rotations from Geissman et al. (1982) are shown by white arrows. Rotations established by previous studies are shown by green arrows (e.g., Geissman et al., 1982, 1984; Cashman and Fontaine, 2000; Faulds et al., 2004; King et al., 2007; Petronis et al., 2009; Ferranti et al., 2009; Pluhar et al., 2009; Rood et al., 2011; Carlson et al., 2013). Regional faults (red): APHF, Agai Pah Hills fault; AVF, Antelope Valley fault; BSF, Benton Springs fault; CF, Candelaria fault; CL, Carson lineament; CoF, Coaldale fault; EF, Excelsior fault; GF, Genoa fault; GHF, Gumdrop Hills fault; GVF, Grizzly Valley fault; IHF, Indian Head fault; OF, Olinghouse fault; PSF, Petrified Springs fault; PLF, Pyramid Lake fault; QVF, Queen Valley fault; RCF, Robinson Creek fault; SRF, Singatse Range fault; SVF, Smith Valley fault; Wal, Wabuska lineament; WRF, Wassuk Range frontal fault; WSF, Warm Springs Valley fault. White dashed lines denote orocline of Faulds and Henry (2008).*
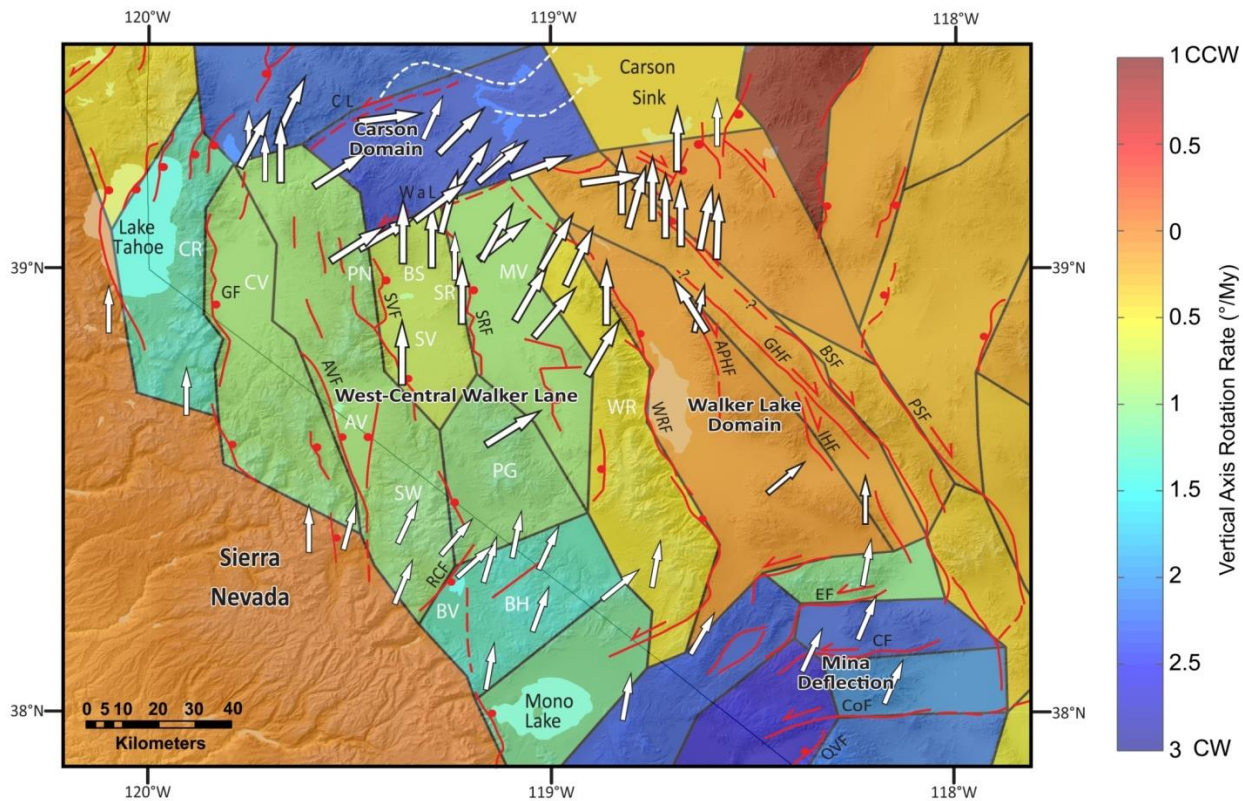
Figure 2. *Geodetic block model of vertical-axis rotation rates in the central Walker Lane and adjacent regions. Figure modified from preferred geodetic model of Bormann et al. (2016). White arrows: paleomagnetic rotation data from Figure 1. Physiographic regions of the west-central Walker Lane (white): AV, Antelope Valley; BH, Bodie Hills; BS, Buckskin Range; BV, Bridgeport Valley; CR, Carson Range; CV, Carson Valley; MV, Mason Valley; PG, Pine Grove Hills; PN, Pine Nut Mountains; SR, Singatse Range; SV, Smith Valley; SW, Sweetwater Mountains; WR, Wassuk Range. Major faults and lineaments are the same as those in Figure 1.*

2.5.3 Summary of observations of strike slip through the trip so far

Ian Pierce

- Well defined active strike-slip faults are observed in the Walker Lake basin (e.g. Dong et al., 2014), Truckee basin (Polaris fault; Hunter et al., 2011) and in the southern part of Mason Valley (**Figure 1a**). Despite the absence of discrete measurable offsets, the geometry of the Smith Valley range front fault allows that the rangefront fault accommodates a significant portion of right-lateral shear . DePolo and Sawyer (2005) report observing strike-slip faulting in the East Carson Valley fault zone (**Figure 1a**), though the rate of slip across this broad and complex zone of discontinuous faults remains undefined. The short, northeast-striking faults of the North Tahoe fault system (labeled North Tahoe in **Figure 1a**, including the Stateline, Incline Village, Little Valley, and Washoe Valley faults) form an en-echelon right stepping pattern (**Figure 1a**) and may be considered book-shelf faults (e.g., Tapponnier et al., 1990), accommodating northwest-directed dextral shear. Thus, while slip rate indicators are not consistently preserved or recognized along all rangefronts and adjacent valleys, the geometry and pattern of faulting along with the distribution of late Quaternary slip as a function of fault strike indicates that there is a significantly larger portion of shear being accommodated by active strike-slip fault displacements than we have yet been able to quantify.

- New geologic rates mostly agree with geodetic rates

- Evidence of strike-slip faulting absent along Mason & Antelope rangefronts

- Smith and Wassuk range accommodate oblique dextral slip

- Newly described strike-slip fault in Pine Grove Hills

- >4 mm/yr of unaccounted for dextral shear is likely accommodated as off-fault deformation and/or distributed shear.

SLIP RATES

	Vertical	Dip Parallel (55± 10° normal fault)	Extension	Strike-Slip	GPS Extension	GPS Strike-Slip
Artesia Qy	0.5 +0.7/-0.2	0.6 + 0.9/-0.2	0.4 +0.5/-0.1	0.4?	0.4 ± 0.5	0.5 ± 0.4
Artesia Qi	0.6 +0.8/-0.4	0.7 + 1.0/-0.5	0.4 +0.6/-0.3	0.4?	0.4 ± 0.5	0.5 ± 0.4
Antelope Valley	0.5 +0.5/-0.3	0.6 + 0.6/-0.4	0.4 +0.4/-0.2	-	0.7 ± 0.5	1.1 ± 0.4
Mason Valley (Singatse)	0.05 ± 0.01	0.06 ± 0.01	0.04 ± 0.01	-	0.6 ± 0.5	0.4 ± 0.4
Pine Grove Hills	-	-	-	0.5-1.0?	0.2 ± 0.6	0.6 ± 0.5
Wassuk/Walker Lake	0.8 ± 0.2[b]	-	-	1.0[c]	0.7 ± 0.3	0.6 ± 0.4
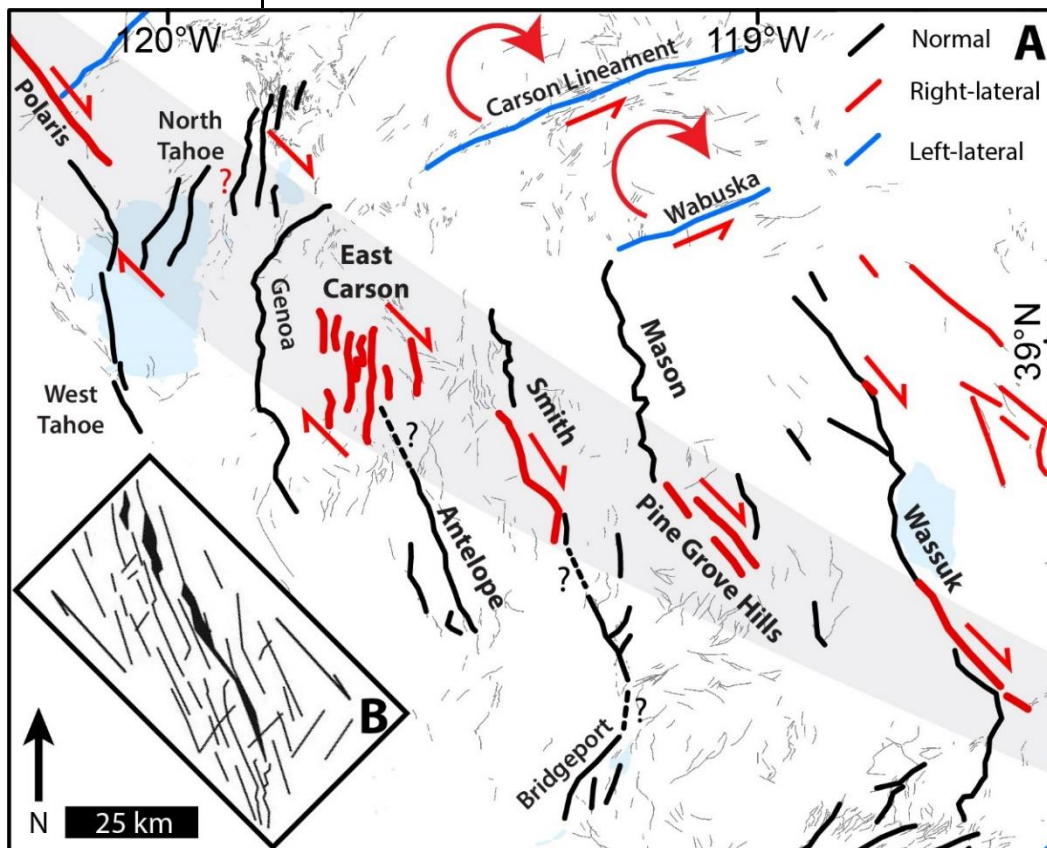
Figure 1 *(a) Fault pattern of the Central Walker Lane. The grey band demonstrates a well-defined zone of en-echelon left-stepping dextral strike-slip faulting. Queried dashed lines indicate possible connections between faults as discussed in text. (b) Sketch of a clay model copied from Atmaoui et al. (2006) produces a similar pattern of left stepping en echelon faults and basins as is observed in the Central Walker Lane.*
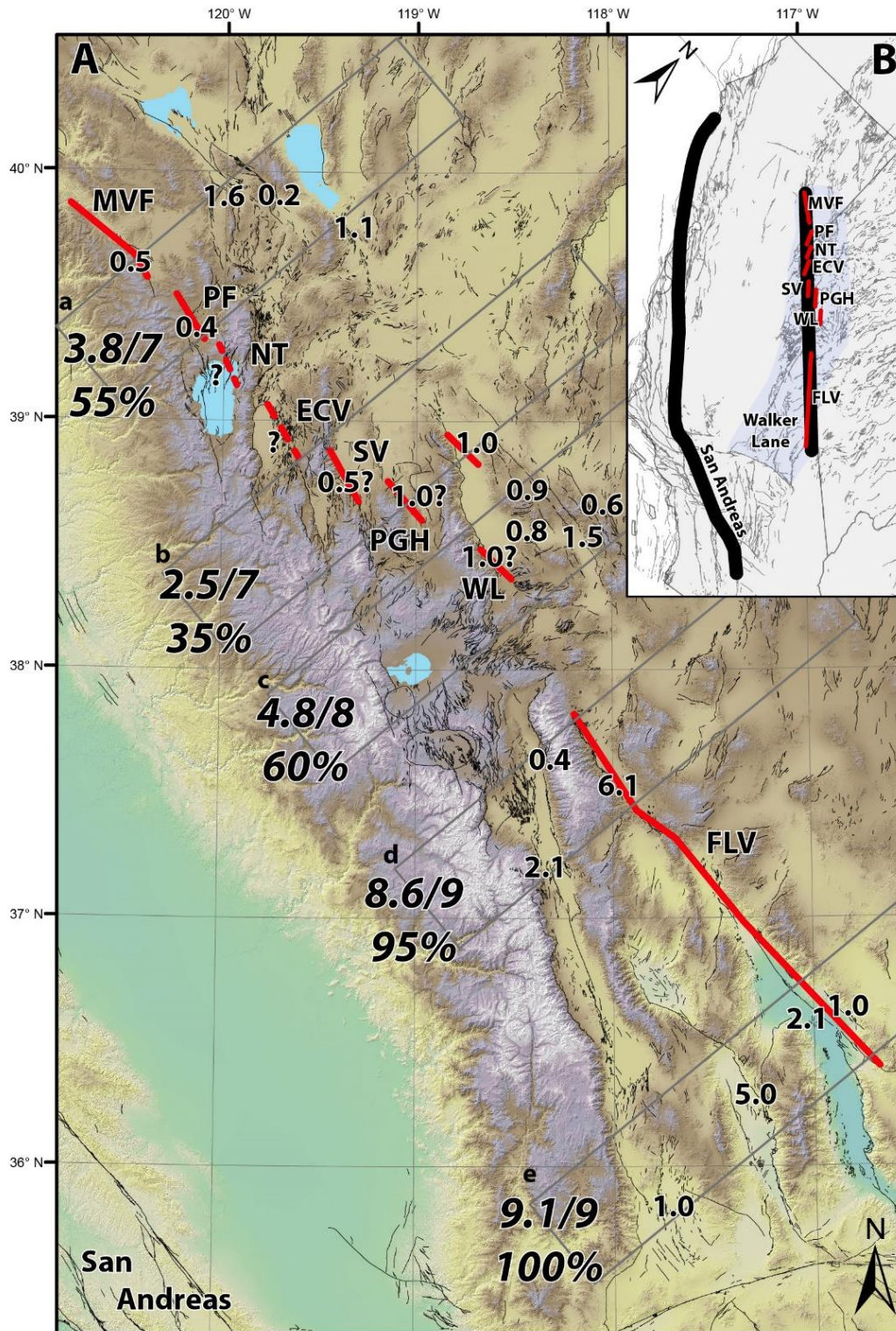
Figure 2. (a) Comparison of dextral shear rates measured across the Walker Lane in various profiles (gray boxes) by GPS (bold numbers), and on individual faults (smaller numbers), in mm/yr (fault slip rates from: Kirby et al., 2006; Guest et al., 2007; Frankel et al., 2011; Hunter et al., 2011; Amos et al., 2013; Gold Ryan D. et al., 2013; Dong et al., 2014; Gold et al., 2014; Angster et al., 2016; Choi, 2016; Frankel et al., 2016; Haddon et al., 2016; Gold et al., 2017). These GPS rates were provided by J. Bormann and are contained in Redwine et al. (2015). The percentages are taken by summing the rates of individual faults in each profile and dividing those by the total geodetic rate in each profile. There is good agreement between geodetic and geologic observations in the Southern Walker Lane, but less so in the Central and Northern Walker Lane. Major strike-slip fault zone discussed in this paper is highlighted by bold red lines with fault abbreviations: FLV-Fish Lake Valley, WL-Walker Lake, PGH-Pine Grove Hills, SV-Smith Valley, ECV-East Carson Valley, NT-North Tahoe, PF-Polaris Fault, MVF-Mohawk Valley. (b) Oblique oriented map of California and Nevada showing the trend of these faults as a bold black line (right) that is subparallel to the San Andreas (left black line).

2.5.4   Geometry of an incipient strike-slip system

Ian Pierce

The grey band in **Figure 1a** highlights the series of fault systems described in the preceding section. Each of these six fault systems is ~25-km-long, and is separated from its neighboring strike-slip faults by left steps ranging in size from ~15 to 25 km. Together these fault systems form a clear en-echelon left-stepping ~25-km-wide pattern of active dextral faults extending for ~200 km from south of Walker Lake to north of Lake Tahoe.

The pattern of faults presented in **Figure 1a** is consistent with the early stages of models of distributed strike-slip fault systems (e.g., Schreurs, 2003; Hatem et al., 2017) such as shown in **Figure 1b**. This model produces a discontinuous pattern of left-stepping Riedel shears that form en-echelon extensional basins and dextral faults similar to what is observed in the Central Walker Lane (Atmaoui et al., 2006). All of the faults in these models begin as extensional cracks. Aydin and Nur (1982) show that pull-apart basins in a strike-slip system are largely a result of step overs of en-echelon strike-slip faults, which is consistent with the pattern of faulting observed in the Central Walker Lane. Thus, the majority of north-striking normal faulting along a number of the ranges in this region is driven by northwest directed dextral shear along discrete faults, similar to these experimental models (e.g., Aydin and Nur, 1982; Atmaoui et al., 2006). In this light the westward decrease in inception age and total magnitude of extension and normal faulting from the Wassuk Range to the Sierra Nevada may be evidence for the encroachment of strike-slip faulting through this region.

When viewed in large scale the pattern of strike-slip faulting in the Central Walker Lane falls on strike with both the Mohawk Valley and the Death Valley/Fish Lake Valley faults (**Figures 1, 12**), which are among the most active strike-slip faults of the Northern and Southern Walker Lane, respectively. Laboratory models predict that as displacement accumulates across fault systems, initial distributed faulting will eventually organize into a single through going strike-slip fault. The trend of faults illustrated by the right bold line in **Figure 12b** forms a linear, >500-km-long fault zone that is nearly parallel to the San Andreas fault, and eventually this may be the trace of a continuous strike-slip fault, accommodating much of the strain across the Pacific-North American plate boundary. However, fault complexity is not solely a result of total shear accumulated across a fault zone, as faults largely take advantage of pre-existing crustal weaknesses (e.g., Molnar, 1988; Ziegler et al., 1998; Matenco et al., 2007; Dyksterhuis and Müller, 2008; Aitken et al., 2013; Raimondo et al., 2014; Calzolari et al., 2016), which in the Walker Lane may have been inherited from an earlier episode of Basin and Range extension, prior to initiation of the current Walker Lane strain regime (Surpless et al., 2002), or even earlier structural irregularities (e.g. Faulds and Henry, 2008).
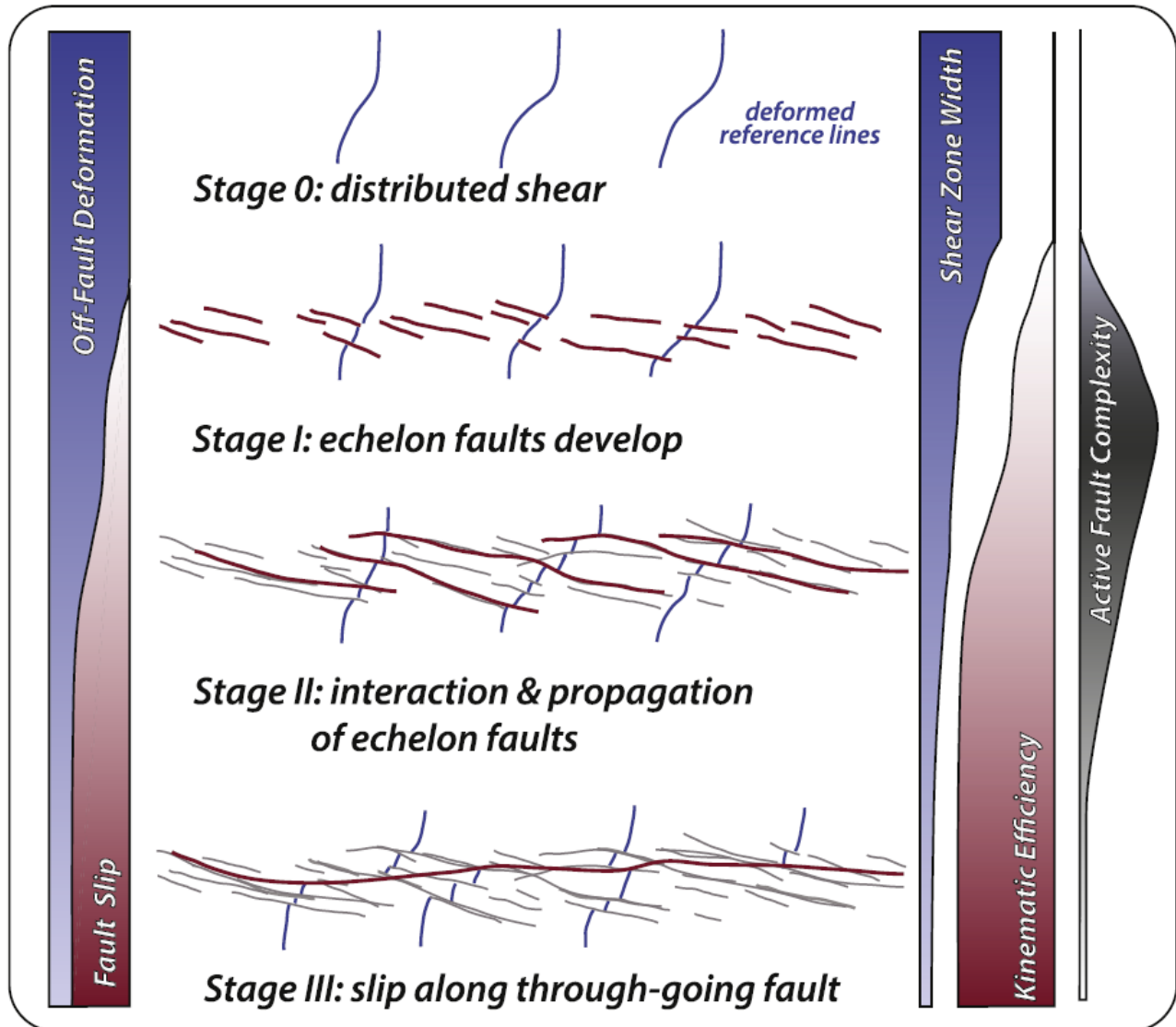
Figure 3 Copied from Hatem et al. (2017)

3 DAY 3: Bridgeport Basin

3.1 Bridgeport Basin

The following is a synopsis, with abstract and figures of:

3.1.1 Drought-triggered magmatic inflation, crustal strain and seismicity at the Long Valley Caldera, Central Walker Lane

by

W.C. Hammond, C. Kreemer, I. Zaliapin, G. Blewitt

[1]Nevada Geodetic Laboratory Nevada Bureau
of Mines and Geology, University of Nevada,
Reno

Reno NV, 89557

[2]Department of Mathematics and Statistics
University of Nevada, Reno
Reno NV, 89557

Citation:

Abstract

We use GPS data to show synchronization between the 2011-2016 drought cycle in California, accelerated uplift of the Sierra Nevada Mountains, and enhanced magmatic inflation of the Long Valley Caldera (LVC) magmatic system. The drought period coincided with faster uplift rate, changes in gravity seen in the Gravity Recovery and Climate Experiment (GRACE), and changes in standardized relative climate dryness index. These observations together suggest that the Sierra Nevada elevation is sensitive to changes in hydrological loading conditions which subsequently influences the LVC magmatic system. We use robust imaging of horizontal GPS velocities to derive time-variable shear and dilatational strain rates in a region with highly variable station distribution. The results show that the highest strain rates are near the eastern margin of the Sierra Nevada and western edge of the Central Walker Lane (CWL) passing directly through LVC. The drought period saw geographic shifts in the distribution in active shear strain in the CWL more than 60 km from the LVC, delineating the minimum extent over which the active magmatic system effects the CWL tectonic environment. We analyze declustered seismicity data to show that locations with higher seismicity rates tend to be 1) areas with higher strain rates, and 2) areas in which strain rates increased during drought-enhanced inflation. We hypothesize that drought conditions reduce vertical surface mass loading which decreases pressure at depth in the LVC system, in turn enhances magmatic inflation, and drives horizontal elastic stress changes that redistribute active CWL strain and modulate seismicity.
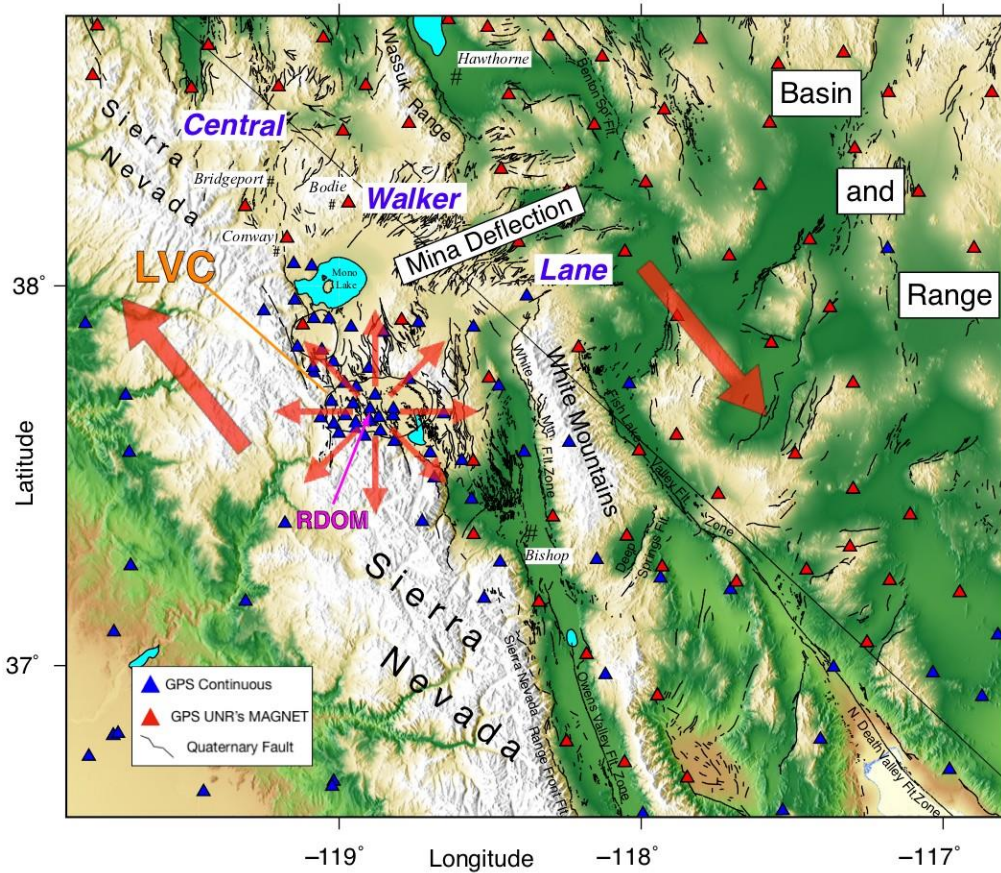
Figure 1. Color shaded topography of the central Sierra Nevada Mountains, Long Valley Caldera (LVC) and western Great Basin. Triangles are locations of GPS stations from the MAGNET GPS Network (red) and other continuous GPS stations (blue). Black lines are Quaternary faults. Large red arrows indicate general sense of crustal shear across CWL, smaller red arrows indicate sense of inflation at LVC. Orange text and line segment indicate location of LVC. The location of GPS station RDOM, which sits atop the Resurgent Dome near the center of the LVC, is indicated with the magenta text and arrow. Location of other geographic and tectonic features, such as towns, the Sierra Nevada Mountains, Mina Deflection, Wassuk Range, White Mountains, Basin and Range and selected active faults are indicated with black text.
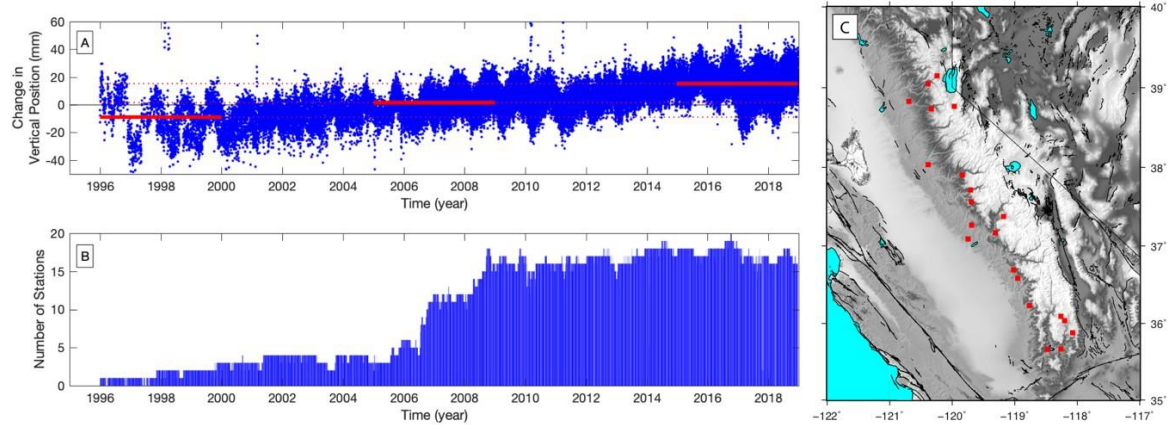
Figure 2. A) Stack of GPS vertical position time series for stations on the west slope of the Sierra Nevada, shifted to minimize misfit so that the aggregate time series crosses zero near year 2007.0. Red line segments show median relative elevation for early (1996.0-2000.0), middle (2005.0-2009.0) and late (2015 - 2019) intervals. The difference between the late and early (middle) periods indicates a net increase in elevation of 24.2 (13.7) mm since the earliest (middle) period of GPS observation. The horizontal dotted lines are extensions of the red segments to better visualize the difference between elevations. B) Number of stations providing data as a function of time. C) Map showing location of GPS stations (red dots) on Sierra Nevada west slope.
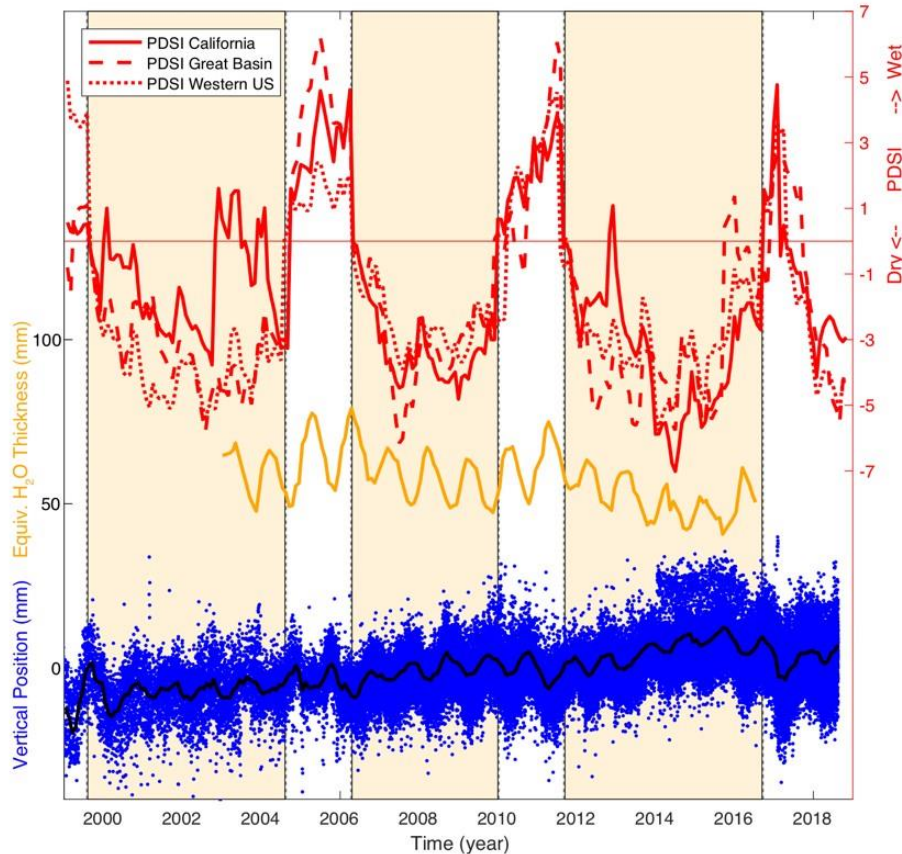

Figure 3. Comparison between indicators of drought versus wet periods to GPS uplift data. Red lines show monthly values of Palmer Drought Severity Index (PDSI) for California, Great Basin and Western US (referring to scale on right vertical axis). Orange line shows GRACE Mascon #1895 in mm of H_2O equivalent water thickness (referring to scale on left vertical axis). Blue dots are summary of Sierra Nevada west slope GPS stations vertical positions as plotted in Figure 1, with monthly means in black (referring to scale on left vertical axis). The time series are shifted vertically to increase clarity.
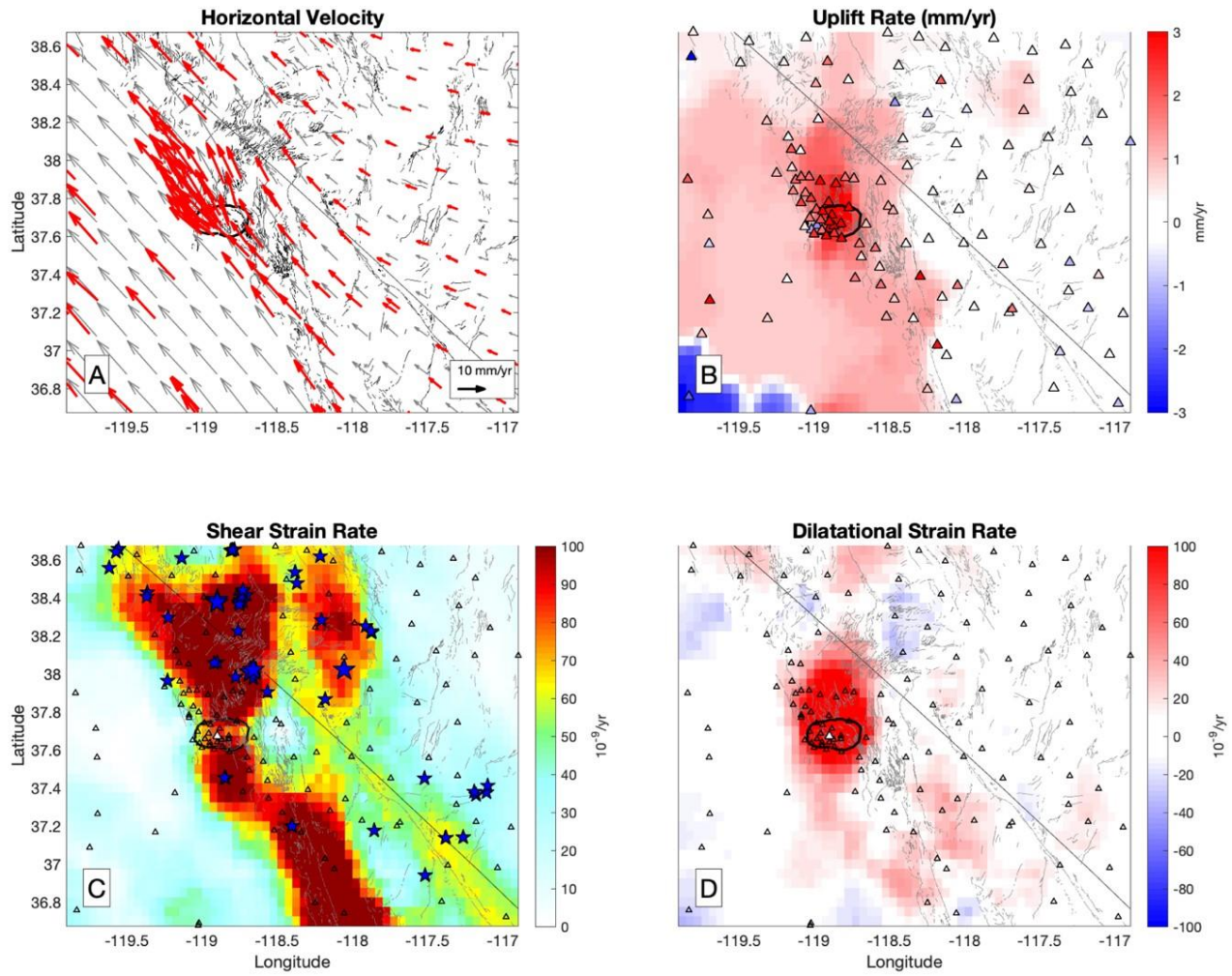
Figure 4. A) Horizontal GPS velocities for the entire GPS dataset 1996.0 to the present. Gray lines are Quaternary faults. Black outline is location of LVC. Gray vectors are interpolated from the red vectors using GPS Imaging. B) Uplift rate from GPS Imaging, vertical rate at each station is shown with triangle color. C) Shear strain rate. Blue stars are epicenter locations for earthquakes above M4, larger stars if M≥5, for events occurring in years 2000.0-2018.0, the period of the seismicity analysis (see Discussion for details). D) Dilatational strain rate. In this and in the following figures the black northwest-southeast diagonal line is the California/Nevada border.
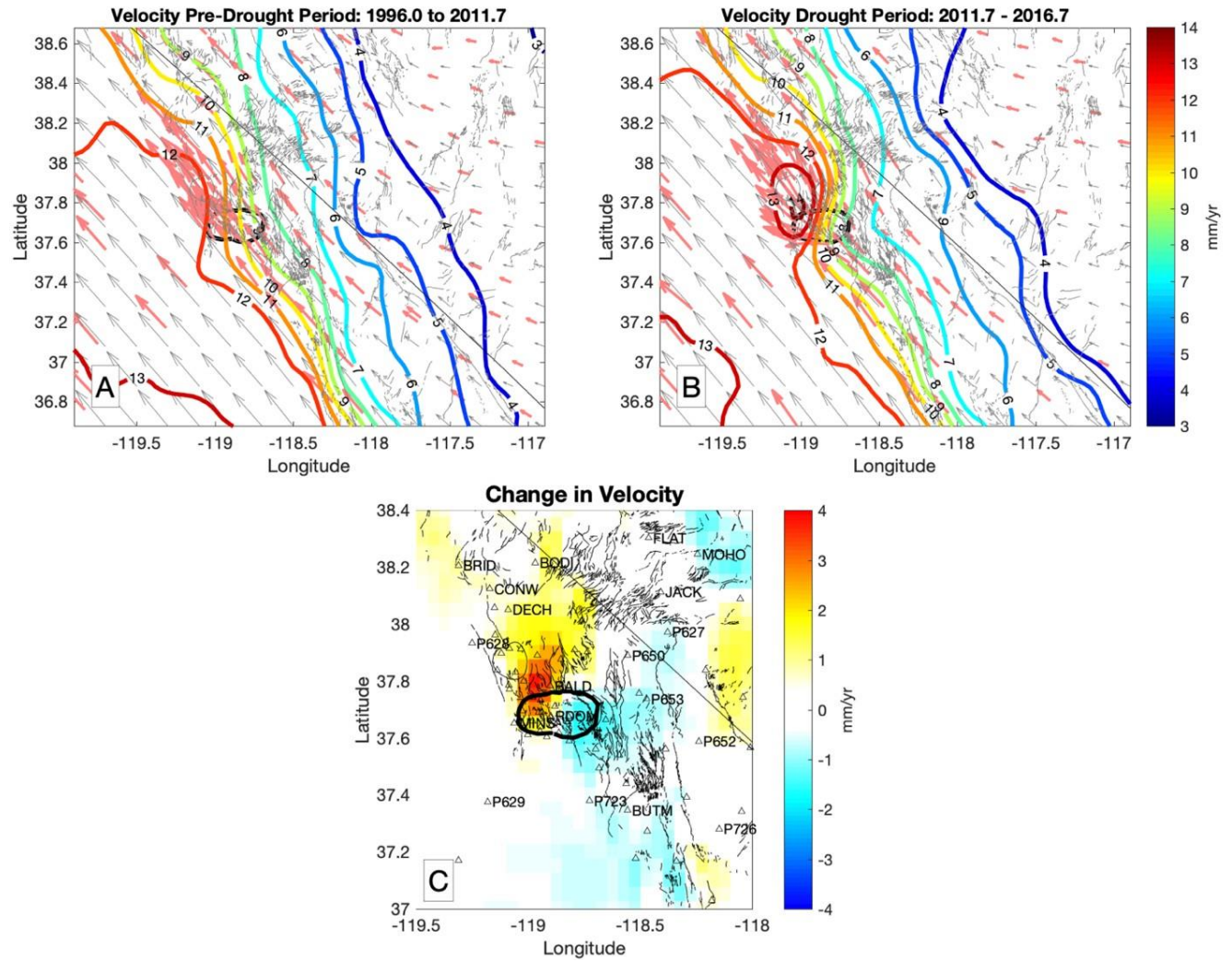
Figure 5. A) GPS horizontal velocity before year 2011.7. Light red vectors are velocities at GPS stations, gray vectors are decimated gridded version of those used to generate color contours of velocity magnitude at levels of 1 mm/yr. Gray lines are Quaternary faults. Black outline is location of LVC. B) Same as A except GPS velocity during the drought 2011.7 to
2016.7. C) Color shaded plot of change in GPS velocity from pre-drought to drough period, zoomed in closer into LVC area. Triangles are locations of GPS stations, names of selected stations are shown. Faults with black lines. Hot colors indicate increase in magnitude of GPS velocity, cool colors indicate decrease, in mm/yr.
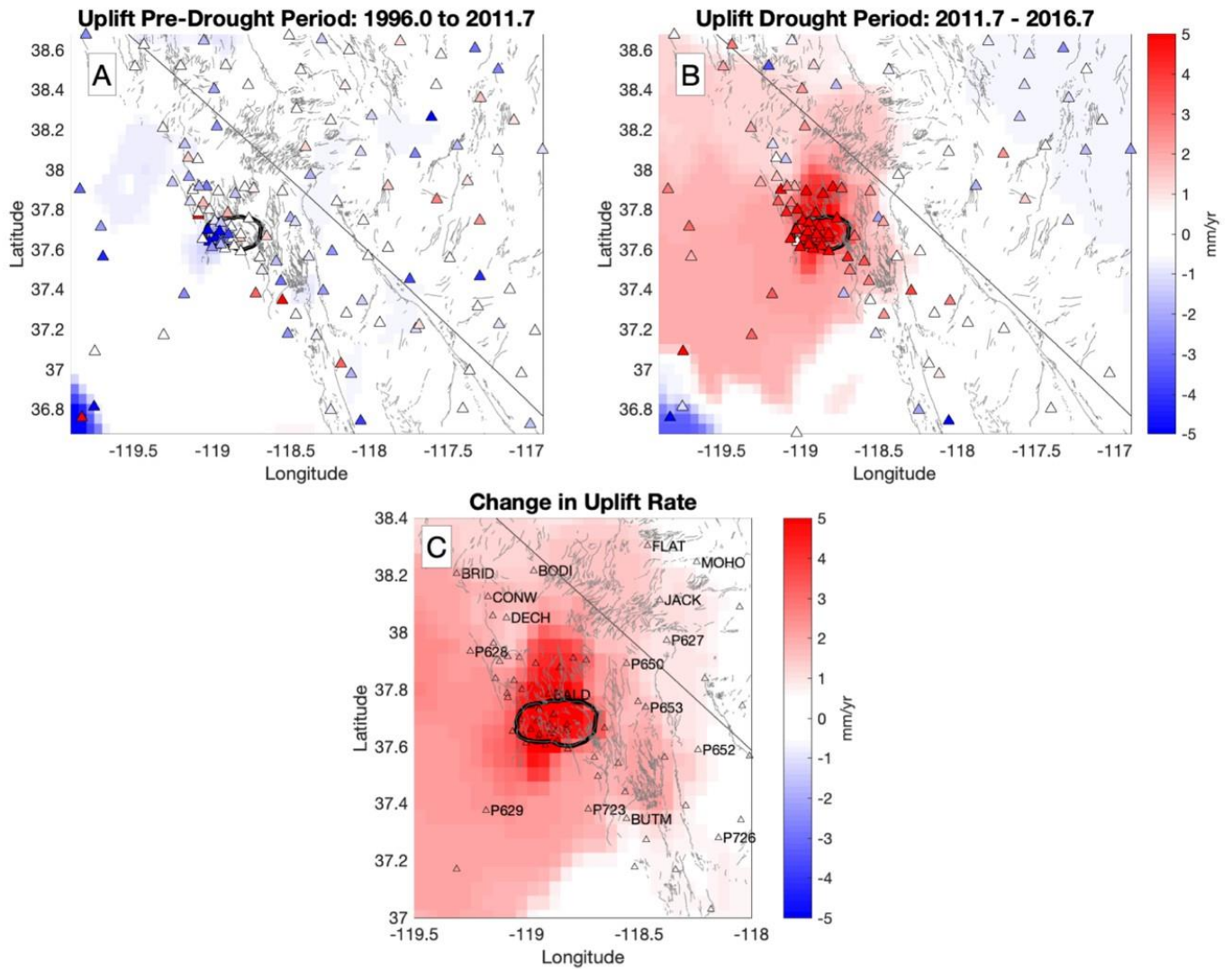
Figure 6. A) GPS uplift rate before 2011.7. Color scale is in mm yr^{-1}. Triangles are locations of GPS stations used to estimate uplift field. Gray lines are Quaternary faults. Black outline is location of LVC. Vertical rate at each station is shown with face color of triangle. B) GPS uplift rate 2011.7 to 2016.7. C) Color shaded plot of difference of GPS uplift rate, zoomed in closer to LVC.
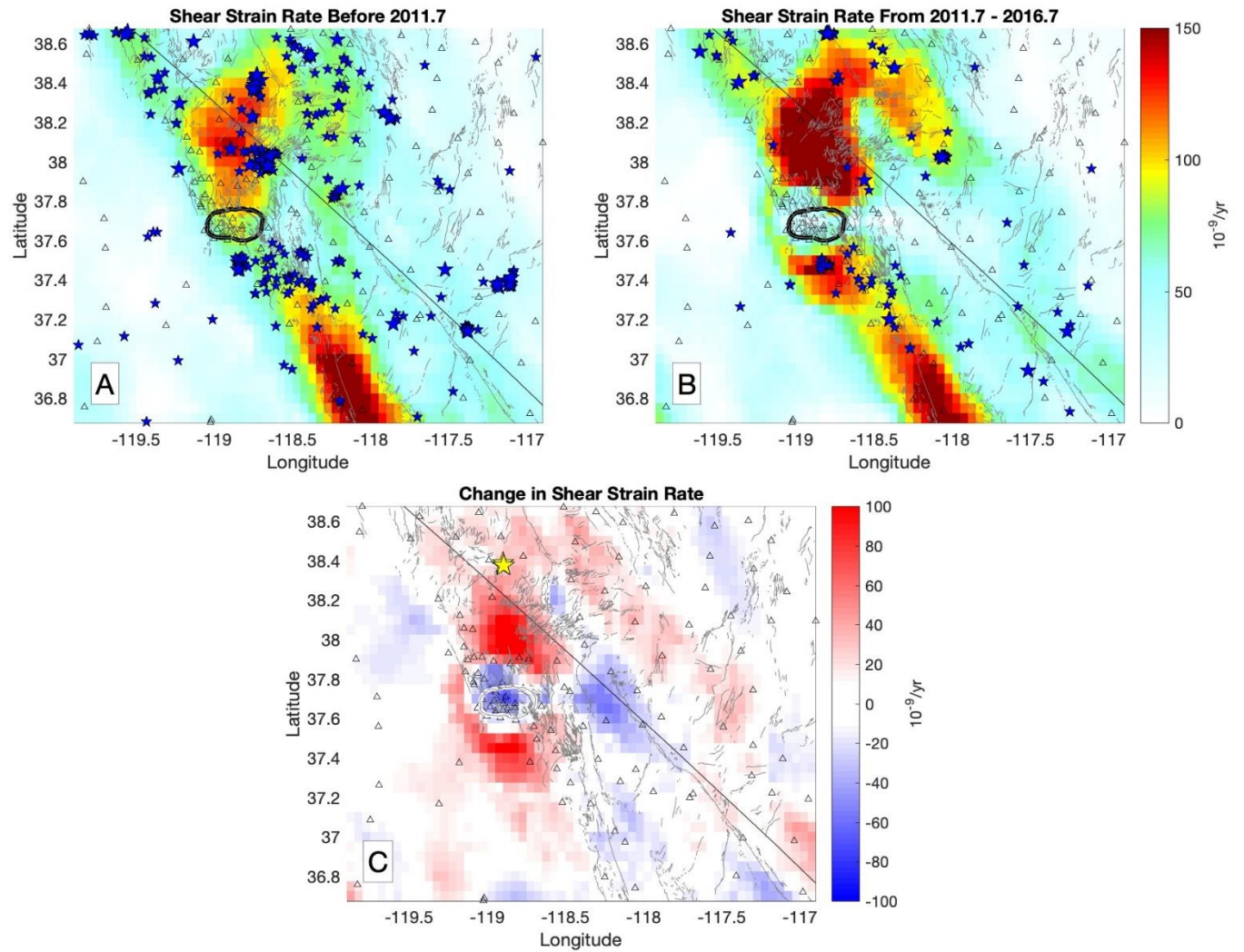
Figure 7. A) Shear strain rate before 2011.7. Color scale is in 10^{-9} yr^{-1}. Triangles are locations of GPS stations used to estimate shear strain rate field. Black outline is location of LVC. Gray lines are Quaternary faults. White triangles are earthquake epicenters for events with M3-4 (small stars) and M>4 (larger stars). B) Shear strain rate from 2011.7 to 2016.7. Symbols as in A. C) Difference in shear strain rate from wet to dry period. Yellow stars indicate location of the three Nine Mile Ranch earthquakes over M5.5 that occurred in December, 2016.
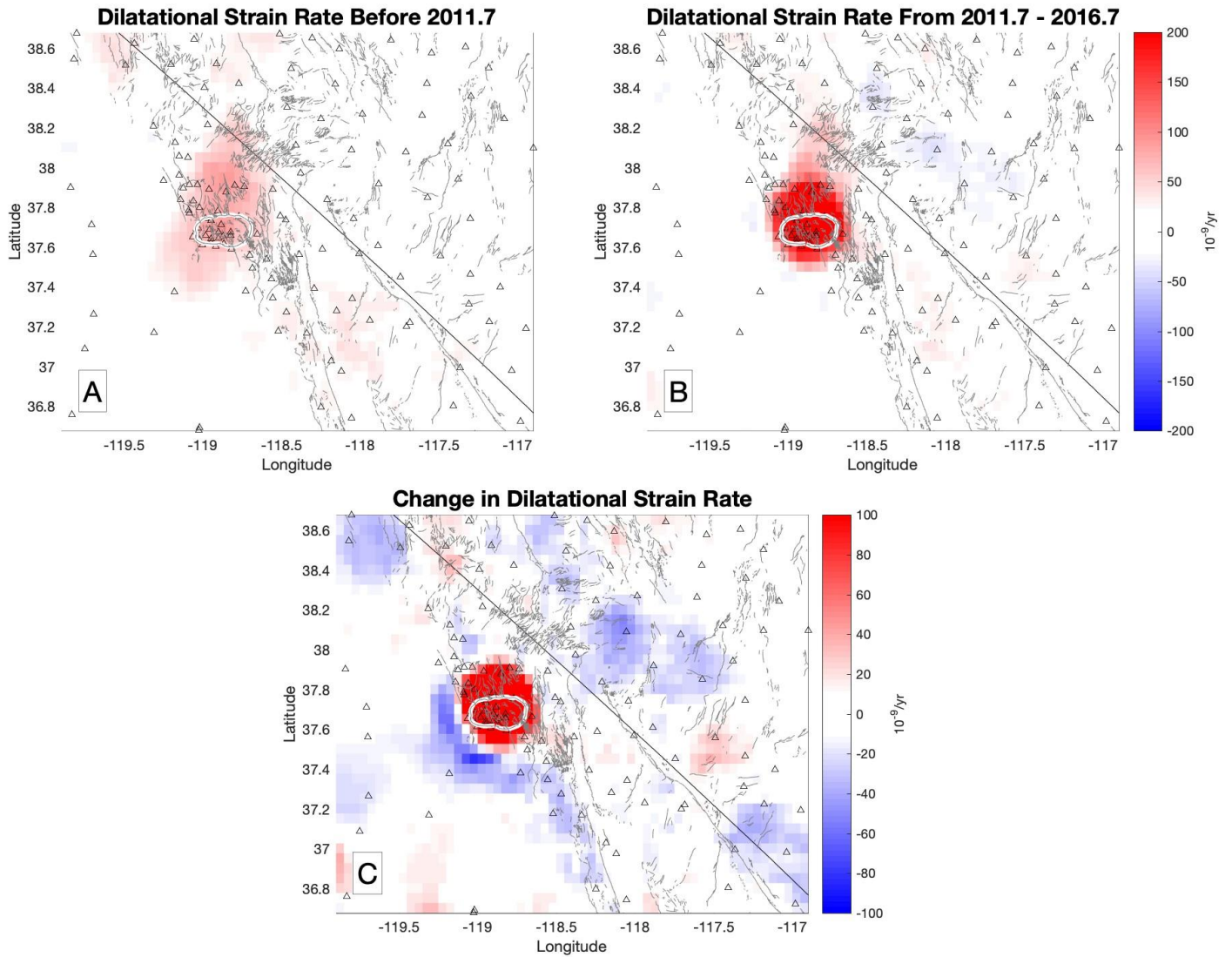
Figure 8. Dilatational strain rate A) before 2011.7 and B) during the drought period 2011.7 to 2016.7. Color scale is in 10^{-9} yr^{-1}. Triangles are locations of GPS stations used to estimate strain rate field. White outline is location of LVC. Gray lines are Quaternary faults. C) Difference in dilatation rate from early to later period.
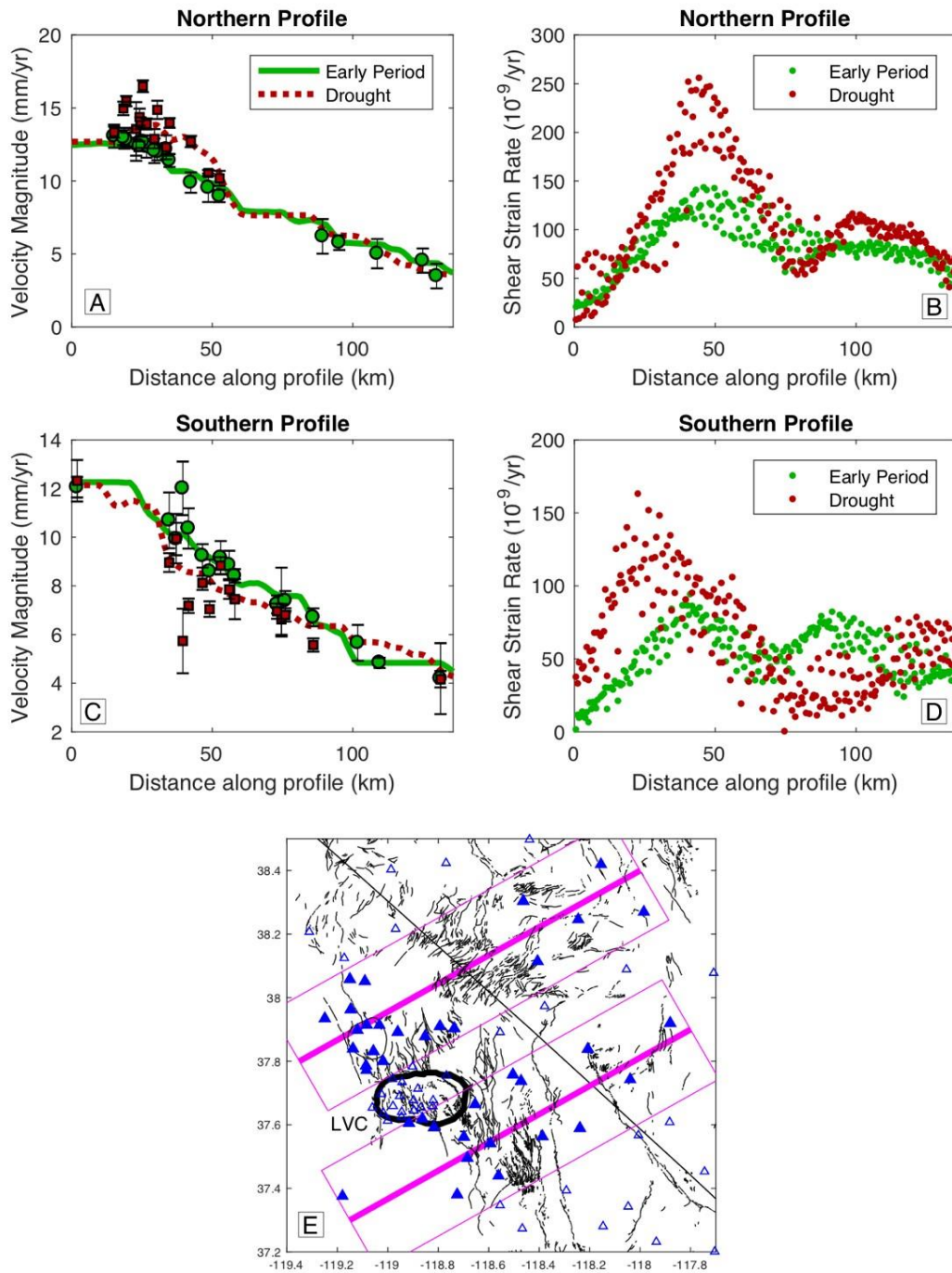
Figure 9. GPS velocity, imaged velocity and shear strain rate in two profiles, one north and one south of the LVC. A) and B) are northern profile, C) and D) southern profile. In A) and C) velocity (circles and squares) and imaged velocity (solid lines) are shown together. B) and D) are profiles of imaged shear strain rate at all grid points that lie within the profile bounds (magenta boxes in E). E) location of profiles on same map bounds as previous figures. Black outline is location of LVC. Black lines are Quaternary faults. Blue triangles are GPS stations, that are filled for stations within the profile bounding boxes.
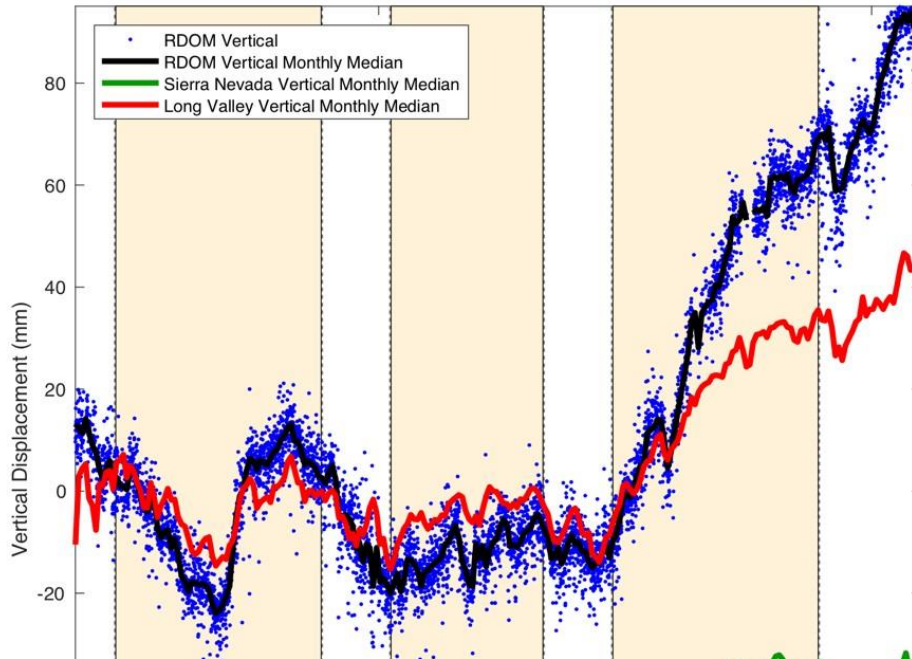
Figure 10. Time series of GPS station RDOM (blue dots) and its monthly median (black line), compared to monthly medians of positions from 25 stations in the LVC (red line), and to change in elevation of west slope of Sierra Nevada using nine stations nearest and west of LVC (green line). There are fewer stations to constrain Sierra Nevada uplift before 2006 (Figure 2), so the green line is dotted to indicate greater uncertainty. Drought intervals in California are indicated with light colored shading as in Figure 3.
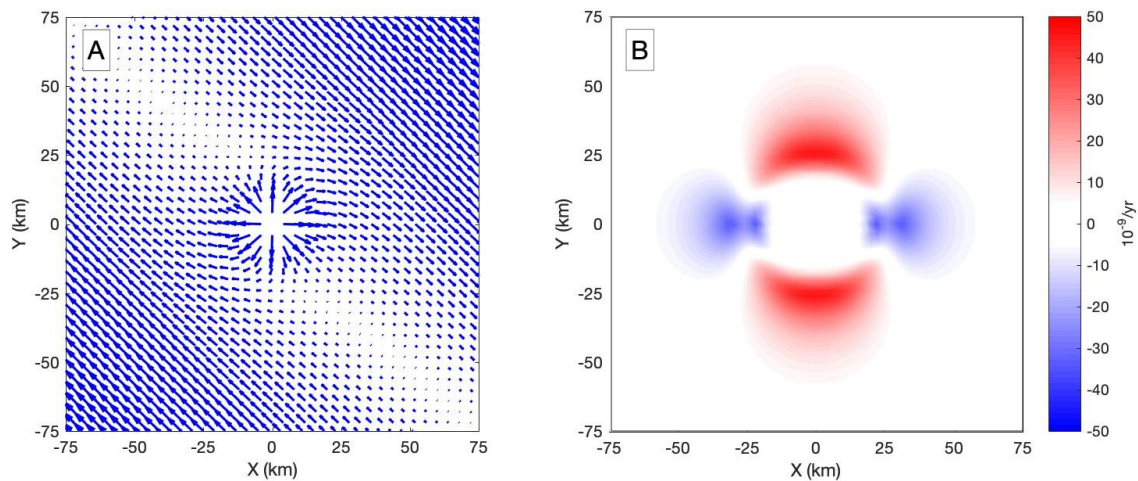

Figure 11. A) The velocity pattern from a superposition of Mogi inflation plus a constant shear strain rate similar to LVC in the CWL. The velocity field is actually four times as dense as indicated but is decimated for plotting. B) The change in shear strain rate between the velocities shown in (A) and a similar model with the inflation removed.
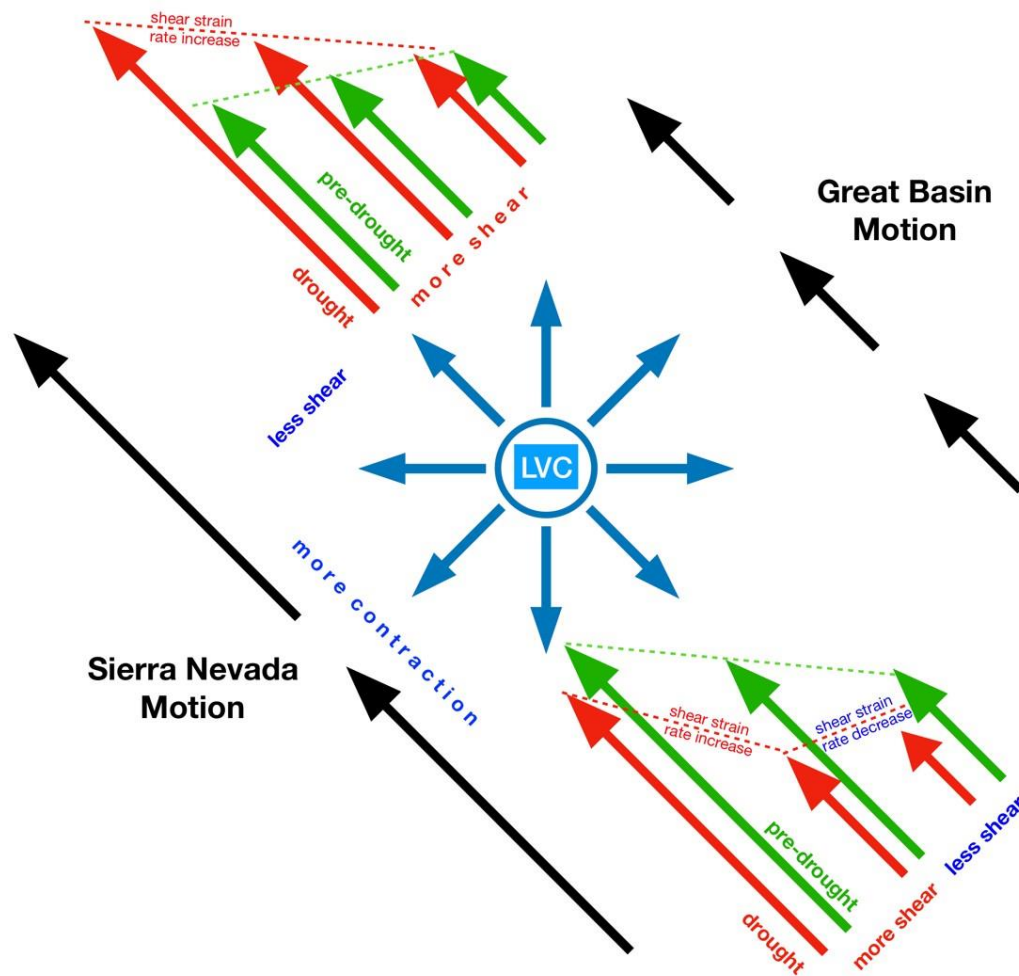
Figure 12. Cartoon model of crustal shear deformation in the presence of an inflationary source near a right step in the Walker Lane fault system. Simplified time-invariant far field motion of the Sierra Nevada and Great Basin are shown with black vectors. LVC inflation is indicated with blue vectors. Shear deformation in the CWL is shown both prior to the drought period (green vectors) and during the drought period (red vectors). The changes in lengths of these vectors resulting from LVC inflation changes the distribution of shear and dilatational deformation in the CWL. Dashed lines help to visualize gradients in velocity and how they change between pre-drought and drought periods.

3.1.2   Bridgeport Overview

Bridgeport basin is cut by a number of north-northeast striking active faults (Figure 1). Rood et al. measured a slip rate from the Buckeye creek outwash moraines of ~0.3 mm/yr for the frontal fault, however this rate does not include the other faults within the basin. We will visit the Twin Lakes moraines at the next stop. Fault orientation would suggest left-lateral/oblique normal faulting, though no clear piercing points are identified.
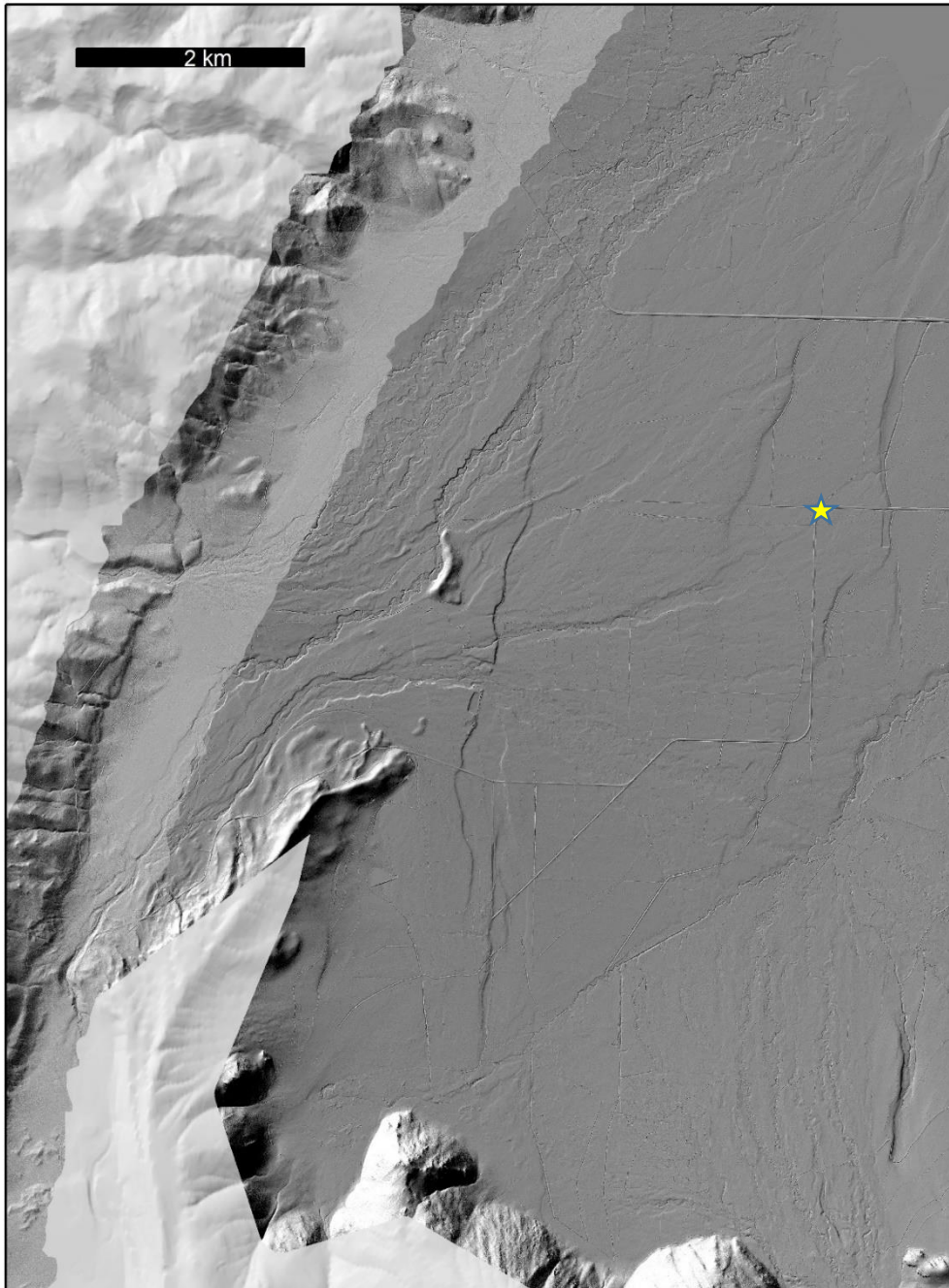

Figure 1: Lidar hillshade of Bridgeport basin showing numerous active NNE striking faults. Star denotes stop.

3.1.3 Neotectonics and Geothermal systems

After Faulds et al. 2011: Assessment of favorable structural settings of geothermal systems in the Great Basin, western USA
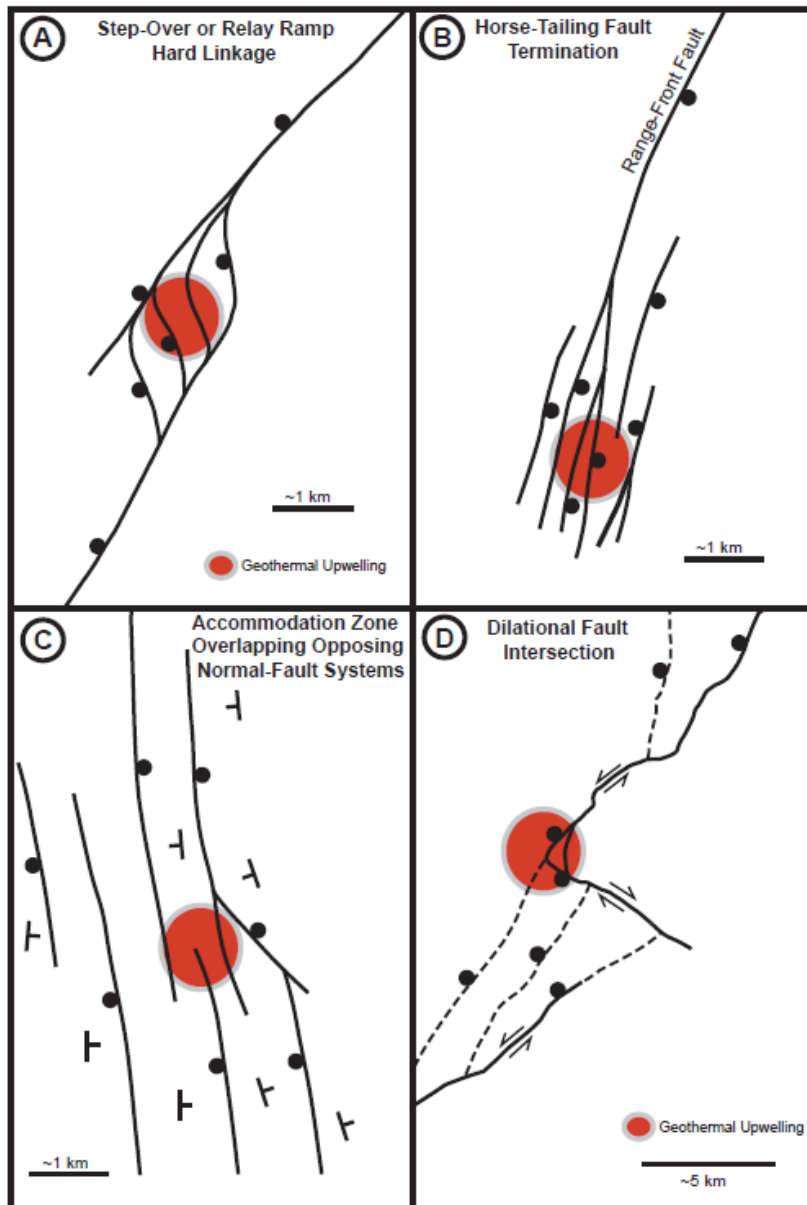

Geothermal systems are heavily controlled by active (Holocene) faults, especially structural complexities. Bell and Ramelli (2007) found that of 37 examined geothermal systems in the Great Basin, 31 were found directly on or in close proximity to Holocene active faults. From this stop, both Buckeye & Travertine hot springs are visible, and both are in close proximity to active faults. Other hot springs we passed on this trip near faults include the Wabuska geothermal plant on the Wabuska fault, and a hot spring near the Artesia fan at the fault bend.

Figure 2. Examples of favorable structural settings for geothermal systems. Areas of upwelling geothermal fluids are shaded in red. A. Step-over or relay ramp between two overlapping normal fault segments with multiple minor faults providing hard linkage between two major faults. B. Terminations of major normal faults, whereby faults break up into multiple splays or horsetail. C. Overlapping, oppositely dipping normal fault systems (accommodation zones) that generate multiple fault intersections in the subsurface. Strike and dip symbols indicate tilt directions of fault blocks. D. Dilational fault intersection between oblique-slip normal faults.
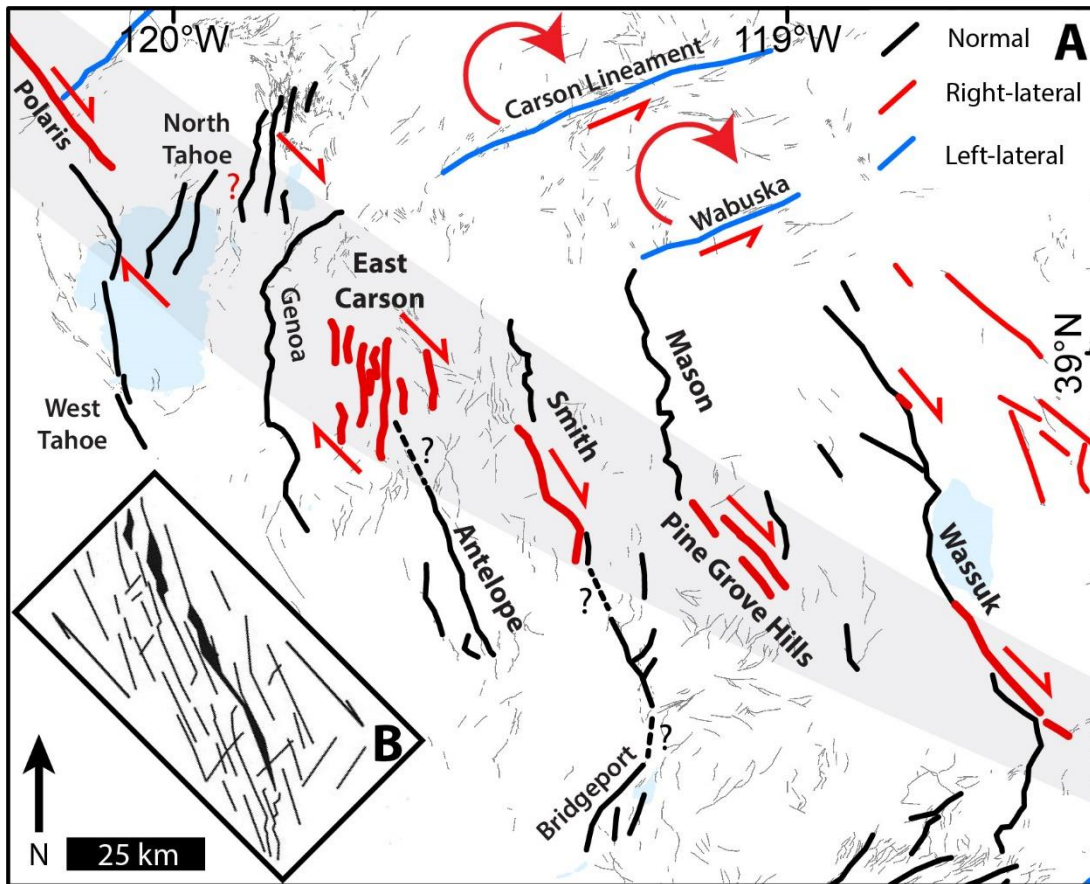
3.1.4 "Short" faults in CWL?

Ian Pierce

Figure 1 *(a) Fault pattern of the Central Walker Lane. The grey band demonstrates a well-defined zone of en-echelon left-stepping dextral strike-slip faulting. Queried dashed lines indicate possible connections between faults as discussed in text. (b) Sketch of a clay model copied from Atmaoui et al. (2006) produces a similar pattern of left stepping en echelon faults and basins as is observed in the Central Walker Lane.*

Using the relation of fault length to moment magnitude from Wesnousky (2008) results in expected magnitudes of 6.9 and 6.7 for the 50- and 22-km-long faults in Smith and Antelope valleys, respectively. These estimates are approximately a quarter magnitude less than estimated using the moment magnitude equation above. Likewise, for the mapped fault lengths, the expected displacements for these faults should be on average 1.5 and 0.7 m, with maxima of 4.5 and 2.0 m, respectively (Figure 2; Wesnousky, 2008). These average values are roughly half and a quarter of what is observed along the Smith and Antelope valley rangefront faults, respectively. Average displacements of ~3 m, similar to values observed on each of these faults, are typically associated with a normal fault surface rupture length of ~100 km (Wesnousky, 2008). Two hypotheses can explain the observation that observed fault lengths appear insufficient to produce the observed offsets: (1) faults in this part of the Walker Lane rupture with other nearby faults producing longer total rupture lengths, or (2) these faults rupture independently and produce high-stress drop earthquakes.

(a)

Average Geologic Slip (m) vs Length (km)

Legend:
- SS-Slip(m)
- N-Slip
- R-Slip

Data points labeled: 1, 7, 32, 4, 29 (log-linear), 37, 36, 3, 5, 14, 30, 35, 2, 10, 12 (power law), 33, 9, 8, 24, 22, 15, 31&6, 28, 19, 17, 27, 16, 20, 26, 25, 21, 18, 23

$$\text{Slip(m)} = C * \text{Length(km)}$$

Type	C	Chisq	R	N	StDev
SS	.01	23.1	0.60	21	1.10
N	.03	4.7	0.46	7	.82
R	.06	2.7	0.89	7	.62

$$\text{Slip(m)} = -C + C * \log(\text{Length(km)})$$

SS	2.31	12.41	0.88	21	.77

$$\text{Slip(m)} = C * L \wedge D$$

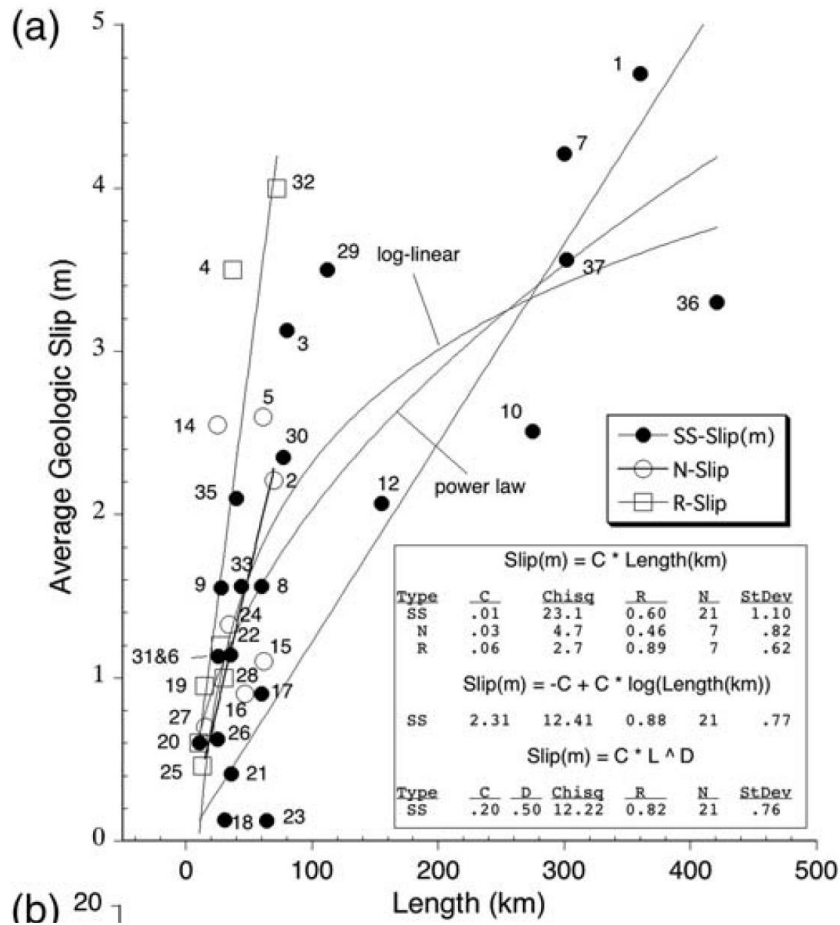| Type	C	D	Chisq	R	N	StDev
SS	.20	.50	12.22	0.82	21	.76

(b) 20

Figure 2 – Copied from Wesnousky 2008: Relation between average geologic slip and surface rupture length for historical earthquakes. For normal faults to produce ~3m of average slip, the surface rupture length should be ~80-100 km.

The size of the observed single event displacements on a number of other faults in this region (e.g., the Incline Village, Little Valley, Stateline, Pine Grove Hills, Bridgeport Valley, and the unnamed faults of eastern Mason Valley) are also greater than expected from historical observations relating fault rupture length to displacement (Wesnousky, 2008; Seitz and Kent, 2014). The traces of several of these faults are less than 20 km yet some have been demonstrated to have produced single event displacements of ~3 m. Faults in the Central Walker Lane may produce complicated, multi-segment ruptures with multiple shorter fault strands (including previously unrecognized fault strands) supporting larger (Mw 7+) earthquakes, not dissimilar to the 1891 Mw 7.5 Nobi, Japan (Kaneda and Okada, 2008), 1932 Ms7.2 Cedar Mountain, Nevada (Bell et al., 1999), 1970 Ms 7.2 Gediz, Turkey (Ambraseys and Tchalenko, 1972), or 2016 Mw 7.8 Kaikoura, New Zealand (Hamling et al., 2017) earthquakes. In Smith Valley, for example, the rangefront fault may produce ruptures extending further south along strike towards Strawberry Flat, or even as far as Bridgeport Valley, where numerous large normal fault scarps are preserved in these two small (~15-km-long) basins (**Figure 1a**). This would result in a total rupture length of ~75-100 km, as one might expect based on the measured displacements and the relations in Wesnousky (2008). Antelope Valley might rupture along with faults to the north in the East Carson Valley fault zone, increasing rupture length from ~20 to ~65 km (**Figure 1a**).

It is also possible that the earthquake ruptures in this region are indeed limited to these short mapped fault traces, as normal faults have historically produced large displacements with short rupture lengths in the Basin and Range (e.g. the 1959 M_w 7.2 Hebgen Lake earthquake produced an average displacement of 2.9 m over a 27-km-long rupture; Myers and Hamilton, 1964). If fault ruptures in this part of the Walker Lane are indeed "short", then to produce the same displacements as earthquakes with typically longer ruptures implies that these earthquakes have a high stress-drop. Hecker et al. (2010) show that faults with low slip rates and little cumulative slip, like those in the Central Walker Lane, produce particularly high static stress-drop earthquakes. Perhaps this is evidence that faults in this part of the Walker Lane are stronger than faults elsewhere in the Cordillera, which is counterintuitive to what one might expect based on the high geothermal gradient and shallow crust of this region.
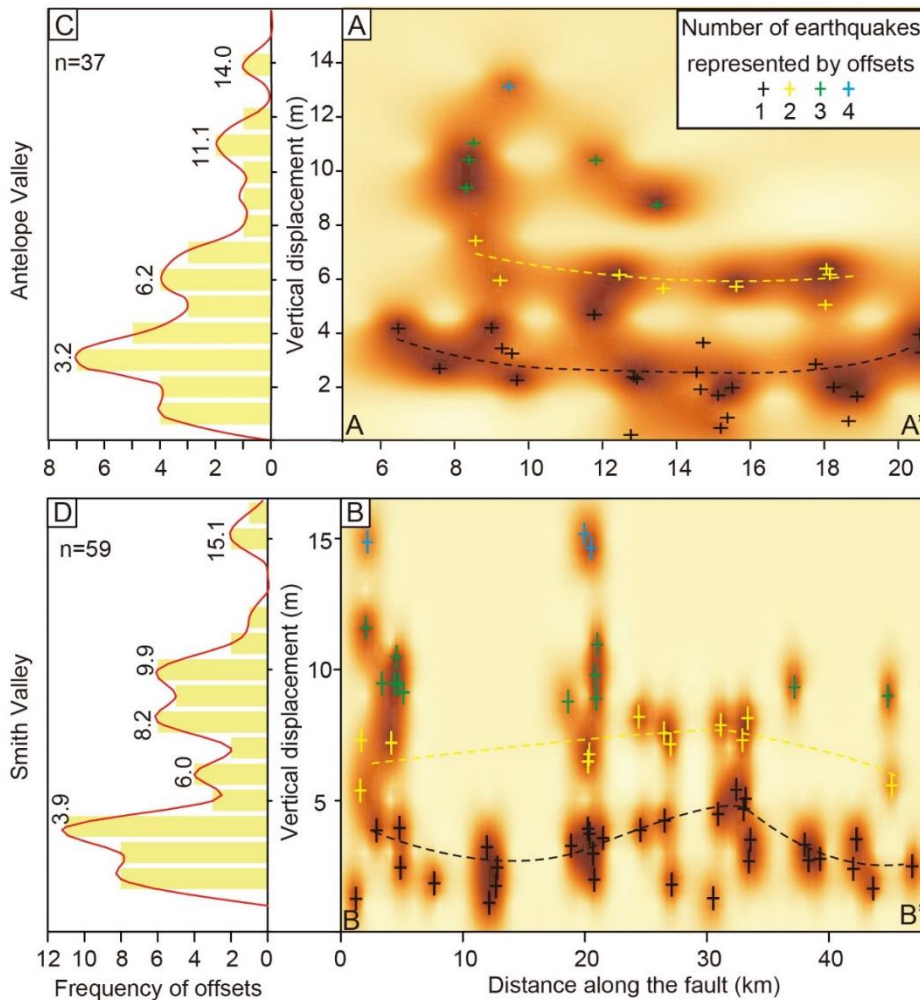
Figure 3 *Slip distribution plots (a, b) and displacement histograms (c, d) for Antelope Valley (a, c) and Smith Valley (b, d). Locations of cross sections indicated on Figure 2. The displacement of the most recent and penultimate earthquakes for each fault can be estimated by looking at the smallest two peaks of each histogram. For the slip distributions (a, b), darker colors indicate higher probabilities. The colored crosses represent our interpretation of the number of earthquakes which produced each displacement measurement.*

3.2 Twin Lakes & Buckeye Moraines

copied from Rood et al. 2011

Table 1
Summary of fault slip rates from Monte Carlo simulations of scarp profiles and [10]Be surface exposure ages.

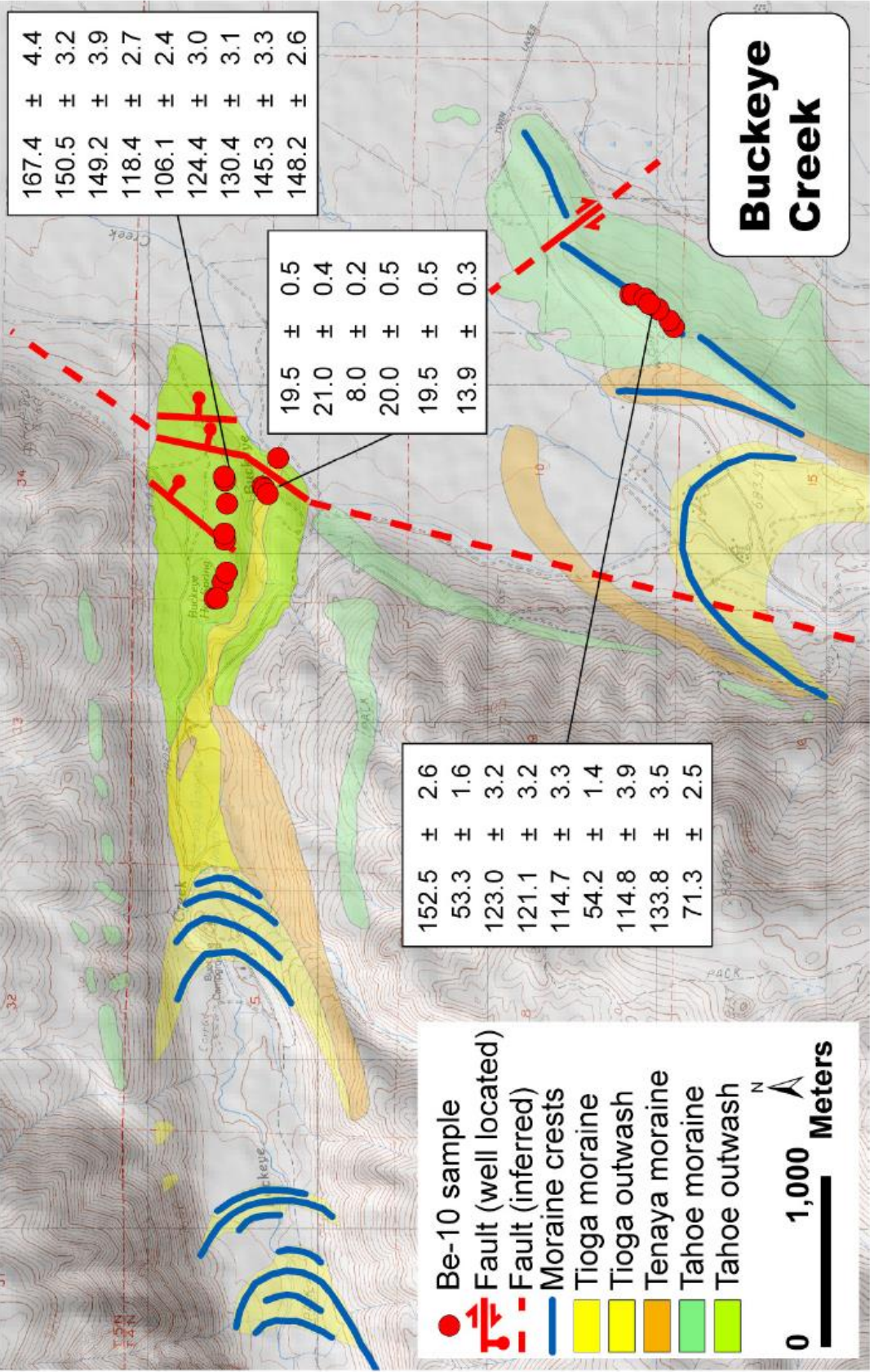| Profile	Survey method[a]	Slip mode (m)	Slip uncertainty (m) (95%CI)	Age association[b]	Exposure age (ky)	Age uncertainty (ky) (1σ)[c]	n[d]	Slip rate mode (mm year^{-1})	Slip rate uncertainty (mm year^{-1}) (95%CI)
Buckeye Creek Tioga outwash terrace									
BCTI-1	dGPS	6	+2/−1	BCTI07	20	+/−1	4	0.3	+0.1/−0.1
Buckeye Creek Tahoe outwash terrace									
BCTA-1	dGPS	45	+13/−10	BCTA06	148	+/−2	4	0.3	+0.1/−0.1
BCTA-2	dGPS	48	+12/−9	BCTA06	148	+/−2	4	0.3	+0.1/−0.1
BCTA-3	dGPS	44	+14/−6	BCTA06	148	+/−2	4	0.3	+0.1/−0.1
BCTA-4	dGPS	44	+15/−8	BCTA06	148	+/−2	4	0.3	+0.1/−0.1

Buckeye Creek

167.4 ± 4.4
150.5 ± 3.2
149.2 ± 3.9
118.4 ± 2.7
106.1 ± 2.4
124.4 ± 3.0
130.4 ± 3.1
145.3 ± 3.3
148.2 ± 2.6

19.5 ± 0.5
21.0 ± 0.4
8.0 ± 0.2
20.0 ± 0.5
19.5 ± 0.5
13.9 ± 0.3

152.5 ± 2.6
53.3 ± 1.6
123.0 ± 3.2
121.1 ± 3.2
114.7 ± 3.3
54.2 ± 1.4
114.8 ± 3.9
133.8 ± 3.5
71.3 ± 2.5

Be-10 sample
Fault (well located)
Fault (inferred)
Moraine crests
Tioga moraine
Tioga outwash
Tenaya moraine
Tahoe moraine
Tahoe outwash

N

0   1,000   Meters
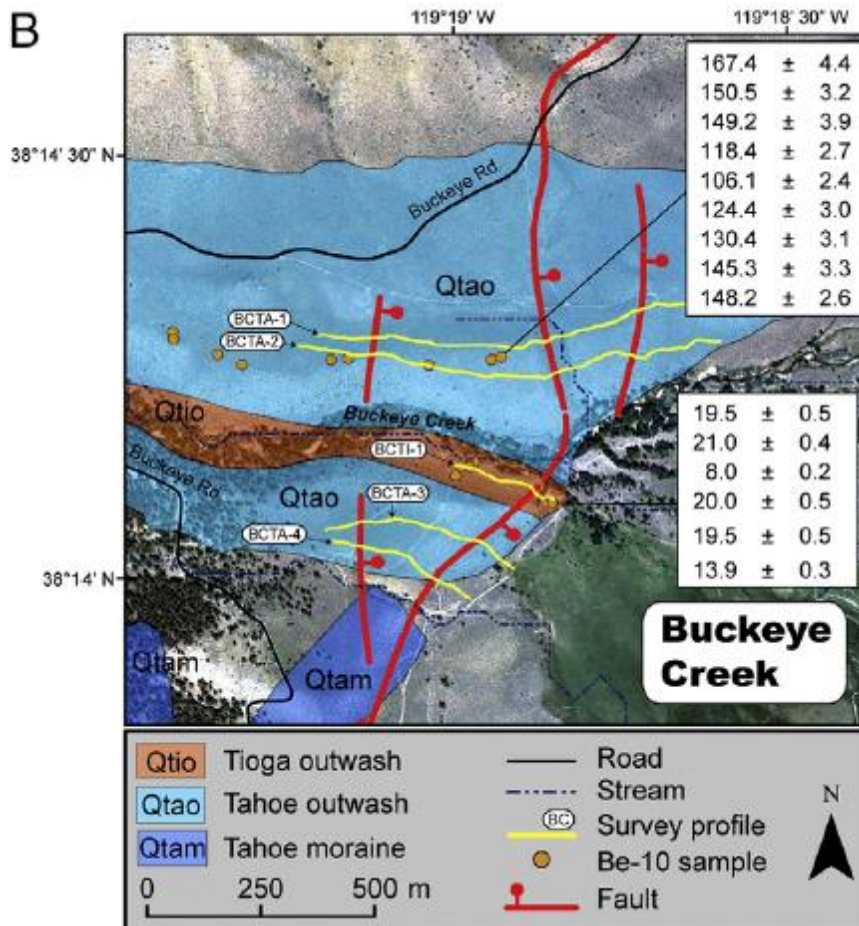
4   References for Pierce stops

Adams, K.D., Wesnousky, S.G., 1998. Shoreline processes and the age of the Lake Lahontan highstand in the Jessup embayment, Nevada. Geol. Soc. Am. Bull. 110, 1318–1332.

Aitken, A.R.A., Raimondo, T., Capitanio, F.A., 2013. The intraplate character of supercontinent tectonics. Gondwana Res. 24, 807–814. https://doi.org/10.1016/j.gr.2013.03.005

Aktug, B., Nocquet, J.M., Cingöz, A., Parsons, B., Erkan, Y., England, P., Lenk, O., Gürdal, M.A., Kilicoglu, A., Akdeniz, H., Tekgül, A., 2009. Deformation of western Turkey from a combination of permanent and campaign GPS data: Limits to block-like behavior. J. Geophys. Res. Solid Earth 114. https://doi.org/10.1029/2008JB006000

Ambraseys, N.N., Tchalenko, J.S., 1972. Seismotectonic Aspects of the Gediz, Turkey, Earthquake of March 1970. Geophys. J. R. Astron. Soc. 30, 229–252. https://doi.org/10.1111/j.1365-246X.1972.tb05811.x

An, L.-J., Sammis, C.G., 1996. Development of strike-slip faults: shear experiments in granular materials and clay using a new technique. J. Struct. Geol. 18, 1061–1077. https://doi.org/10.1016/0191-8141(96)00012-0

Angster, S., Wesnousky, S., Figueiredo, P., Owen, L.A., Hammer, S., 2019. Late Quaternary slip rates for faults of the Central Walker Lane: Spatiotemporal strain release in a strike-slip fault system. Geosphere 57.

Angster, S., Wesnousky, S., Huang, W., Kent, G., Nakata, T., Goto, H., 2016. Application of UAV Photography to Refining the Slip Rate on the Pyramid Lake Fault Zone, Nevada. Bull. Seismol. Soc. Am. 106, 785–798. https://doi.org/10.1785/0120150144

Atmaoui, N., Kukowski, N., Stöckhert, B., König, D., 2006. Initiation and development of pull-apart basins with Riedel shear mechanism: insights from scaled clay experiments. Int. J. Earth Sci. 95, 225–238. https://doi.org/10.1007/s00531-005-0030-1

Aydin, A., Nur, A., 1982. Evolution of pull-apart basins and their scale independence. Tectonics 1, 91–105. https://doi.org/10.1029/TC001i001p00091

Balco, G., Stone, J.O., Lifton, N.A., Dunai, T.J., 2008. A complete and easily accessible means of calculating surface exposure ages or erosion rates from 10Be and 26Al measurements. Quat. Geochronol. 3, 174–195. https://doi.org/10.1016/j.quageo.2007.12.001

Beanland, S., Clark, M.M., 1994. The Owens Valley Fault Zone, Eastern California, and Surface Faulting Associated with the 1872 Earthquake (U.S. Geological Survey Bulletin No. 1982). U.S. Geological Survey.

Bell, J.W., Caskey, S.J., Ramelli, A.R., Guerrieri, L., 2004. Pattern and rates of faulting in the central Nevada seismic belt, and paleoseismic evidence for prior beltlike behavior. Bull. Seismol. Soc. Am. 94, 1229–1254.

Bell, J.W., dePolo, C.M., Ramelli, A.R., Sarna-Wojcicki, A.M., Meyer, C.E., 1999. Surface faulting and paleoseismic history of the 1932 Cedar Mountain earthquake area, west-central Nevada, and implications for modern tectonics of the Walker Lane. Geol. Soc. Am. Bull. 111, 791–807. https://doi.org/10.1130/0016-7606(1999)111<0791:SFAPHO>2.3.CO;2

Bennett, R.A., Wernicke, B.P., Niemi, N.A., Friedrich, A.M., Davis, J.L., 2003. Contemporary strain rates in the northern Basin and Range province from GPS data. Tectonics 22, 31 pp. https://doi.org/10.1029/2001TC001355

Borchers, B., Marrero, S., Balco, G., Caffee, M., Goehring, B., Lifton, N., Nishiizumi, K., Phillips, F., Schaefer, J., Stone, J., 2016. Geological calibration of spallation production rates in the CRONUS-Earth project. Quat. Geochronol. 31, 188–198. https://doi.org/10.1016/j.quageo.2015.01.009

Bormann, J.M., Hammond, W.C., Kreemer, C., Blewitt, G., 2016. Accommodation of missing shear strain in the Central Walker Lane, western North America: Constraints from dense GPS measurements. Earth Planet. Sci. Lett. 440, 169–177. https://doi.org/10.1016/j.epsl.2016.01.015

Bormann, J.M., Surpless, B.E., Caffee, M.W., Wesnousky, S.G., 2012. Holocene Earthquakes and Late Pleistocene Slip-Rate Estimates on the Wassuk Range Fault Zone, Nevada. Bull. Seismol. Soc. Am. 102, 1884–1891. https://doi.org/10.1785/0120110287

Briggs, R.W., 2005. Late Pleistocene and Holocene Paleoearthquake Activity of the Olinghouse Fault Zone, Nevada. Bull. Seismol. Soc. Am. 95, 1301–1313. https://doi.org/10.1785/0120040129

Briggs, R.W., 2004. Late Pleistocene fault slip rate, earthquake recurrence, and recency of slip along the Pyramid Lake fault zone, northern Walker Lane, United States. J. Geophys. Res. 109. https://doi.org/10.1029/2003JB002717

Calzolari, G., Rossetti, F., Seta, M.D., Nozaem, R., Olivetti, V., Balestrieri, M.L., Cosentino, D., Faccenna, C., Stuart, F.M., Vignaroli, G., 2016. Spatio-temporal evolution of intraplate strike-slip faulting: The Neogene–Quaternary Kuh-e-Faghan Fault, central Iran. GSA Bull. 128, 374–396. https://doi.org/10.1130/B31266.1

Carlson, C., 2017. Kinematics and Transfer Mechanisms of Strain Accommodation at the Transition between the Northern and Central Walker Lane, Western Nevada (Doctoral Dissertation). University of Nevada, Reno, Reno, NV.

Cashman, P.H., Fontaine, S.A., 2000. Strain partitioning in the northern Walker Lane, western Nevada and northeastern California. Tectonophysics 326, 111–130.

dePolo, C.M., Sawyer, T., 2005. Paleoseismic studies along the Eastern Carson Valley fault system (Final Technical Report), U.S. Geological Survey National Hazards Reduction Program.

Dixon, T.H., Miller, M., Farina, F., Wang, H., Johnson, D., 2000. Present-day motion of the Sierra Nevada block and some tectonic implications for the Basin and Range province, North American Cordillera. Tectonics 19, 1–24.

Dong, S., Ucarkus, G., Wesnousky, S.G., Maloney, J., Kent, G., Driscoll, N., Baskin, R., 2014. Strike-slip faulting along the Wassuk Range of the northern Walker Lane, Nevada. Geosphere 10, 40–48.

Dyksterhuis, S., Müller, R.D., 2008. Cause and evolution of intraplate orogeny in Australia. Geology 36, 495–498. https://doi.org/10.1130/G24536A.1

Faulds, J.E., Bouchot, V., Moeck, I., Oguz, K., 2009. Structural Controls on Geothermal Systems in Western Turkey: A Preliminary Report 33, 8.

Faulds, J.E., Henry, C.D., 2008. Tectonic influences on the spatial and temporal evolution of the Walker Lane: An incipient transform fault along the evolving Pacific – North American plate boundary 34.

Faulds, J.E., Henry, C.D., Hinz, N.H., 2005. Kinematics of the northern Walker Lane: An incipient transform fault along the Pacific–North American plate boundary. Geology 33, 505–508.

Frankel, K.L., Dolan, J.F., Finkel, R.C., Owen, L.A., Hoeft, J.S., 2007. Spatial variations in slip rate along the Death Valley-Fish Lake Valley fault system determined from LiDAR topographic data and cosmogenic 10Be geochronology. Geophys. Res. Lett. 34. https://doi.org/10.1029/2007GL030549

Frankel, K.L., Dolan, J.F., Owen, L.A., Ganev, P., Finkel, R.C., 2011. Spatial and temporal constancy of seismic strain release along an evolving segment of the Pacific–North America plate boundary. Earth Planet. Sci. Lett. 304, 565–576. https://doi.org/10.1016/j.epsl.2011.02.034

Ganev, P.N., Dolan, J.F., Frankel, K.L., Finkel, R.C., 2010. Rates of extension along the Fish Lake Valley fault and transtensional deformation in the Eastern California shear zone–Walker Lane belt. Lithosphere 2, 33–49. https://doi.org/10.1130/L51.1

Gilbert, C.M., Reynolds, M.W., 1973. Character and Chronology of Basin Development, Western Margin of the Basin and Range Province. Geol. Soc. Am. Bull. 84, 2489. https://doi.org/10.1130/0016-7606(1973)84<2489:CACOBD>2.0.CO;2

Gold, R., dePolo, C., Briggs, R., Crone, A., Gosse, J., 2013. Late Quaternary Slip-Rate Variations along the Warm Springs Valley Fault System, Northern Walker Lane, California–Nevada Border. Bull. Seismol. Soc. Am. 103, 542–558. https://doi.org/10.1785/0120120020

Gold, R.D., Briggs, R.W., Crone, A.J., DuRoss, C.B., 2017. Refining fault slip rates using multiple displaced terrace risers—An example from the Honey Lake fault, NE California, USA. Earth Planet. Sci. Lett. 477, 134–146. https://doi.org/10.1016/j.epsl.2017.08.021

Gold, R.D., Briggs, R.W., Personius, S.F., Crone, A.J., Mahan, S.A., Angster, S.J., 2014. Latest Quaternary paleoseismology and evidence of distributed dextral shear along the Mohawk Valley fault zone, northern Walker Lane, California: Paleoseismology Mohawk Valley fault zone. J. Geophys. Res. Solid Earth 119, 5014–5032. https://doi.org/10.1002/2014JB010987

Gold, R.D., Reitman, N.G., Briggs, R.W., Barnhart, W.D., Hayes, G.P., Wilson, E., 2015. On- and off-fault deformation associated with the September 2013 Mw 7.7 Balochistan earthquake: Implications for geologic slip rate measurements. Tectonophysics. https://doi.org/10.1016/j.tecto.2015.08.019

Gosse, J.C., Phillips, F.M., 2001. Terrestrial in situ cosmogenic nuclides: theory and application. Quat. Sci. Rev. 20, 1475–1560.

Gourmelen, N., Dixon, T.H., Amelung, F., Schmalzle, G., 2011. Acceleration and evolution of faults: An example from the Hunter Mountain–Panamint Valley fault zone, Eastern California. Earth Planet. Sci. Lett. 301, 337–344. https://doi.org/10.1016/j.epsl.2010.11.016

Guest, B., Niemi, N., Wernicke, B., 2007. Stateline fault system: A new component of the Miocene-Quaternary Eastern California shear zone. GSA Bull. 119, 1337–1347. https://doi.org/10.1130/0016-7606(2007)119[1337:SFSANC]2.0.CO;2

Haddon, E.K., Amos, C.B., Zielke, O., Jayko, A.S., Bürgmann, R., 2016. Surface slip during large Owens Valley earthquakes. Geochem. Geophys. Geosystems 17, 2239–2269. https://doi.org/10.1002/2015GC006033

Hamling, I.J., Hreinsdóttir, S., Clark, K., Elliott, J., Liang, C., Fielding, E., Litchfield, N., Villamor, P., Wallace, L., Wright, T.J., D'Anastasio, E., Bannister, S., Burbidge, D., Denys, P., Gentle, P., Howarth, J., Mueller, C., Palmer, N., Pearson, C., Power, W., Barnes, P., Barrell, D.J.A., Dissen, R.V., Langridge, R., Little, T., Nicol, A., Pettinga, J., Rowland, J., Stirling, M., 2017. Complex multifault rupture during the 2016 Mw 7.8 Kaikōura earthquake, New Zealand. Science 356, eaam7194. https://doi.org/10.1126/science.aam7194

Hammond, W.C., Blewitt, G., Kreemer, C., 2011. Block modeling of crustal deformation of the northern Walker Lane and Basin and Range from GPS velocities. J. Geophys. Res. 116. https://doi.org/10.1029/2010JB007817

Hammond, W.C., Thatcher, W., 2007. Crustal deformation across the Sierra Nevada, northern Walker Lane, Basin and Range transition, western United States measured with GPS, 2000–2004. J. Geophys. Res. 112. https://doi.org/10.1029/2006JB004625

Hammond, W.C., Thatcher, W., 2005. Northwest Basin and Range tectonic deformation observed with the Global Positioning System, 1999–2003. J. Geophys. Res. 110. https://doi.org/10.1029/2005JB003678

Hanks, T.C., Kanamori, H., 1979. A moment magnitude scale. J. Geophys. Res. Solid Earth 84, 2348–2350. https://doi.org/10.1029/JB084iB05p02348

Hatem, A.E., Cooke, M.L., Toeneboehn, K., 2017. Strain localization and evolving kinematic efficiency of initiating strike-slip faults within wet kaolin experiments. J. Struct. Geol. 101, 96–108. https://doi.org/10.1016/j.jsg.2017.06.011

Hecker, S., Dawson, T.E., Schwartz, D.P., 2010. Normal-Faulting Slip Maxima and Stress-Drop Variability: A Geological PerspectiveNormal-Faulting Slip Maxima and Stress-Drop Variability: A Geological Perspective. Bull. Seismol. Soc. Am. 100, 3130–3147. https://doi.org/10.1785/0120090356

Herbert, J.W., Cooke, M.L., Oskin, M., Difo, O., 2014. How much can off-fault deformation contribute to the slip rate discrepancy within the eastern California shear zone? Geology 42, 71–75. https://doi.org/10.1130/g34738.1

Hidy, A.J., Gosse, J.C., Pederson, J.L., Mattern, J.P., Finkel, R.C., 2010. A geologically constrained Monte Carlo approach to modeling exposure ages from profiles of cosmogenic nuclides: An example from Lees Ferry, Arizona. Geochem. Geophys. Geosystems 11. https://doi.org/10.1029/2010GC003084

Hunter, L.E., Howle, J.F., Rose, R.S., Bawden, G.W., 2011. LiDAR-Assisted Identification of an Active Fault near Truckee, California. Bull. Seismol. Soc. Am. 101, 1162–1181. https://doi.org/10.1785/0120090261

Kaneda, H., Okada, A., 2008. Long-Term Seismic Behavior of a Fault Involved in a Multiple-Fault Rupture: Insights from Tectonic Geomorphology along the Neodani Fault, Central Japan. Bull. Seismol. Soc. Am. 98, 2170–2190. https://doi.org/10.1785/0120070204

Kent, G.M., Babcock, J.M., Driscoll, N.W., Harding, A.J., Dingler, J.A., Seitz, G.G., Gardner, J.V., Mayer, L.A., Goldman, C.R., Heyvaert, A.C., Richards, R.C., Karlin, R., Morgan, C.W., Gayes, P.T., Owen, L.A., 2005. 60 k.y. record of extension across the western boundary of the Basin and Range province: Estimate of slip rates from offset shoreline terraces and a catastrophic slide beneath Lake Tahoe. Geology 33, 365–368. https://doi.org/10.1130/G21230.1

Kirby, E., Anandakrishnan, S., Phillips, F., Marrero, S., 2008. Late Pleistocene slip rate along the Owens Valley fault, eastern California. Geophys. Res. Lett. 35. https://doi.org/10.1029/2007GL031970

Kirby, E., Burbank, D.W., Reheis, M., Phillips, F., 2006. Temporal variations in slip rate of the White Mountain Fault Zone, Eastern California. Earth Planet. Sci. Lett. 248, 168–185. https://doi.org/10.1016/j.epsl.2006.05.026

Koehler, R.D., Wesnousky, S.G., 2011. Late Pleistocene regional extension rate derived from earthquake geology of late Quaternary faults across the Great Basin, Nevada, between 38.5° N and 40° N latitude. Geol. Soc. Am. Bull. 123, 631–650.

Kohl, C.P., Nishiizumi, K., 1992. Chemical isolation of quartz for measurement of in-situ-produced cosmogenic nuclides. Geochim. Cosmochim. Acta 56, 3583–3587.

Lal, D., 1991. Cosmic ray labeling of erosion surfaces: in situ nuclide production rates and erosion models. Earth Planet. Sci. Lett. 104, 424–439.

Lee, J., Spencer, J., Owen, L., 2001. Holocene slip rates along the Owens Valley fault, California: Implications for the recent evolution of the Eastern California Shear Zone. Geology 29, 819–822. https://doi.org/10.1130/0091-7613(2001)029<0819:HSRATO>2.0.CO;2

Li, X., Huang, W., Pierce, I.K.D., Angster, S.J., Wesnousky, S.G., 2017. Characterizing the Quaternary expression of active faulting along the Olinghouse, Carson, and Wabuska lineaments of the Walker Lane. Geosphere 13, 2119–2136. https://doi.org/10.1130/GES01483.1

Lifton, N., 2016. Implications of two Holocene time-dependent geomagnetic models for cosmogenic nuclide production rate scaling. Earth Planet. Sci. Lett. 433, 257–268. https://doi.org/10.1016/j.epsl.2015.11.006

Link, M.H., Roberts, M.T., Newton, M.S., 1985. Walker Lake Basin, Nevada: An Example of Late Tertiary (?) to Recent Sedimentation in a Basin Adjacent to an Active Strike-Slip Fault, in: Strike-Slip Deformation, Basin Formation, and Sedimentation. Society for Sedimentary Geology.

Maloney, J.M., Noble, P.J., Driscoll, N.W., Kent, G.M., Smith, S.B., Schmauder, G.C., Babcock, J.M., Baskin, R.L., Karlin, R., Kell, A.M., Seitz, G.G., Zimmerman, S., Kleppe, J.A., 2013. Paleoseismic history of the Fallen Leaf segment of the West Tahoe-Dollar Point fault reconstructed from slide deposits in the Lake Tahoe Basin, California-Nevada. Geosphere 9, 1065–1090. https://doi.org/10.1130/GES00877.1

Mann, P., 2007. Global catalogue, classification and tectonic origins of restraining- and releasing bends on active and ancient strike-slip fault systems. Geol. Soc. Lond. Spec. Publ. 290, 13–142. https://doi.org/10.1144/SP290.2

Martin, L.C.P., Blard, P.-H., Balco, G., Lavé, J., Delunel, R., Lifton, N., Laurent, V., 2017. The CREp program and the ICE-D production rate calibration database: A fully parameterizable and updated online tool to compute cosmic-ray exposure ages. Quat. Geochronol. 38, 25–49. https://doi.org/10.1016/j.quageo.2016.11.006

Matenco, L., Bertotti, G., Leever, K., Cloetingh, S., Schmid, S.M., Tărăpoancă, M., Dinu, C., 2007. Large-scale deformation in a locked collisional boundary: Interplay between subsidence and uplift, intraplate stress, and inherited lithospheric structure in the late stage of the SE Carpathians evolution. Tectonics 26. https://doi.org/10.1029/2006TC001951

Molnar, P., 1988. Continental tectonics in the aftermath of plate tectonics. Nature 335, 131. https://doi.org/10.1038/335131a0

Myers, W.B., Hamilton, W., 1964. The Hebgen Lake, Montana, earthquake of August 17, 1959 (No. 435– I), Geological Survey Professional Paper.

Nishiizumi, K., Winterer, E.L., Kohl, C.P., Klein, J., Middleton, R., Lal, D., Arnold, J.R., 1989. Cosmic ray production rates of 10Be and 26Al in quartz from glacially polished rocks. J. Geophys. Res. Solid Earth 94, 17907–17915. https://doi.org/10.1029/JB094iB12p17907

Oskin, M.E., Arrowsmith, J.R., Corona, A.H., Elliott, A.J., Fletcher, J.M., Fielding, E.J., Gold, P.O., Garcia, J.J.G., Hudnut, K.W., Liu-Zeng, J., Teran, O.J., 2012. Near-Field Deformation from the El Mayor–Cucapah Earthquake Revealed by Differential LIDAR. Science 335, 702–705. https://doi.org/10.1126/science.1213778

Personius, S.F., Briggs, R.W., Maharrey, J.Z., Angster, S.J., Mahan, S.A., 2017. A paleoseismic transect across the northwestern Basin and Range Province, northwestern Nevada and northeastern California, USA. Geosphere 13, 782–810. https://doi.org/10.1130/GES01380.1

Pierce, I.K.D., Wesnousky, S.G., Owen, L.A., 2017. Terrestrial cosmogenic surface exposure dating of moraines at Lake Tahoe in the Sierra Nevada of California and slip rate estimate for the West Tahoe Fault. Geomorphology 298, 63–71. https://doi.org/10.1016/j.geomorph.2017.09.030

Raimondo, T., Hand, M., Collins, W.J., 2014. Compressional intracontinental orogens: Ancient and modern perspectives. Earth-Sci. Rev. 130, 128–153. https://doi.org/10.1016/j.earscirev.2013.11.009

Ramelli, A.R., Bell, J.W., dePolo, C.M., Yount, J.C., 1999. Large-magnitude, late Holocene earthquakes on the Genoa fault, west-central Nevada and eastern California. Bull. Seismol. Soc. Am. 89, 1458–1472.

Redwine, J., Wakabayashi, J., Sawyer, T., Bormann, J.M., Kemp, C., Humphrey, J., Unruh, J., Briggs, R.W., Adams, K.D., Ramelli, A.R., Gold, R.D., Burke, R.M., 2015. The 2015 Annual Pacific Cell Friends of the Pleistocene field trip. From Mohawk Valley to Caribou Junction Middle and North Forks of the Feather River, northeastern California (Field Trip Guide).

Reheis, M., 1999. Extent of Pleistocene Lakes in the Western Great Basin. Miscellaneous Field Studies.

Rittase, W.M., Kirby, E., McDonald, E., Walker, J.D., Gosse, J., Spencer, J.Q.G., Herrs, A.J., 2014. Temporal variations in Holocene slip rate along the central Garlock fault, Pilot Knob Valley, California. Lithosphere 6, 48–58. https://doi.org/10.1130/L286.1

Rood, D.H., Burbank, D.W., Finkel, R.C., 2011. Spatiotemporal patterns of fault slip rates across the Central Sierra Nevada frontal fault zone. Earth Planet. Sci. Lett. 301, 457–468. https://doi.org/10.1016/j.epsl.2010.11.006

Sarmiento, A.C., Wesnousky, S.G., Bormann, J.M., 2011. Paleoseismic Trenches across the Sierra Nevada and Carson Range Fronts in Antelope Valley, California, and Reno, Nevada. Bull. Seismol. Soc. Am. 101, 2542–2549. https://doi.org/10.1785/0120100176

Schreurs, G., 2003. Fault development and interaction in distributed strike-slip shear zones: an experimental approach. Geol. Soc. Lond. Spec. Publ. 210, 35–52. https://doi.org/10.1144/GSL.SP.2003.210.01.03

Seitz, G.G., Kent, G., 2014. Closing the Gap between on and Offshore Paleoseismic Records in the Lake Tahoe Basin (Final Technical Report), U.S. Geological Survey National Hazards Reduction Program.

Stauffer, H., 2003. Timing of the Last Highstand of Pluvial Lake Wellington, Smith Valley, Nevada (Master's Thesis). San Jose State University.

Stirling, M.W., Wesnousky, S.G., Shimazaki, K., 1996. Fault trace complexity, cumulative slip, and the shape of the magnitude-frequency distribution for strike-slip faults: a global survey. Geophys. J. Int. 124, 833–868. https://doi.org/10.1111/j.1365-246X.1996.tb05641.x

Stockli, D.F., Dumitru, T.A., McWilliams, M.O., Farley, K.A., 2003. Cenozoic tectonic evolution of the White Mountains, California and Nevada. Geol. Soc. Am. Bull. 115, 788–816.

Stone, J.O., 2000. Air pressure and cosmogenic isotope production. J. Geophys. Res. 105, 23,753-23,759.

Surpless, B., Kroeger, G., 2015. The unusual temporal and spatial slip history of the Wassuk Range normal fault, western Nevada (USA): Implications for seismic hazard and Walker Lane deformation. Geol. Soc. Am. Bull. 127, 737–758. https://doi.org/10.1130/B31159.1

Surpless, B.E., Stockli, D.F., Dumitru, T.A., Miller, E.L., 2002. Two-phase westward encroachment of Basin and Range extension into the northern Sierra Nevada. Tectonics 21, 2-1-2–10. https://doi.org/10.1029/2000tc001257

Tapponnier, P., Armijo, R., Manighetti, I., Courtillot, V., 1990. Bookshelf faulting and horizontal block rotations between overlapping rifts in southern Afar. Geophys. Res. Lett. 17, 1–4. https://doi.org/10.1029/GL017i001p00001

Thatcher, W., Foulger, G.R., Julian, B.R., Svarc, J., Quilty, E., Bawden, G.W., 1999. Present-Day Deformation Across the Basin and Range Province, Western United States. Science 283, 1714–1717.

Unruh, J., Humphrey, J., Barron, A., 2003. Transtensional model for the Sierra Nevada frontal fault system, eastern California. Geology 31, 327–330.

Uppala, S.M., KAllberg, P.W., Simmons, A.J., Andrae, U., Bechtold, V.D.C., Fiorino, M., Gibson, J.K., Haseler, J., Hernandez, A., Kelly, G.A., Li, X., Onogi, K., Saarinen, S., Sokka, N., Allan, R.P., Andersson, E., Arpe, K., Balmaseda, M.A., Beljaars, A.C.M., Berg, L.V.D., Bidlot, J., Bormann, N., Caires, S., Chevallier, F., Dethof, A., Dragosavac, M., Fisher, M., Fuentes, M., Hagemann, S., H?lm, E., Hoskins, B.J., Isaksen, L., Janssen, P.A.E.M., Jenne, R., Mcnally, A.P., Mahfouf, J.-F., Morcrette, J.-J., Rayner, N.A., Saunders, R.W., Simon, P., Sterl, A., Trenberth, K.E., Untch, A., Vasiljevic, D., Viterbo, P., Woollen, J., 2005. The ERA-40 re-analysis. Q. J. R. Meteorol. Soc. 131, 2961–3012. https://doi.org/10.1256/qj.04.176

Wesnousky, S.G., 2008. Displacement and Geometrical Characteristics of Earthquake Surface Ruptures: Issues and Implications for Seismic-Hazard Analysis and the Process of Earthquake Rupture. Bull. Seismol. Soc. Am. 98, 1609–1632. https://doi.org/10.1785/0120070111

Wesnousky, S.G., 2005. Active faulting in the Walker Lane. Tectonics 24, 35 pp. https://doi.org/10.1029/2004TC001645

Wesnousky, S.G., 1988. Seismological and structural evolution of strike-slip faults. Nature 335, 340. https://doi.org/10.1038/335340a0

Wesnousky, S.G., Bormann, J.M., Kreemer, C., Hammond, W.C., Brune, J.N., 2012. Neotectonics, geodesy, and seismic hazard in the Northern Walker Lane of Western North America: Thirty kilometers of crustal shear and no strike-slip? Earth Planet. Sci. Lett. 329–330, 133–140. https://doi.org/10.1016/j.epsl.2012.02.018

Wesnousky, S.G., Caffee, M., 2011. Range-Bounding Normal Fault of Smith Valley, Nevada: Limits on Age of Last Surface-Rupture Earthquake and Late Pleistocene Rate of Displacement. Bull. Seismol. Soc. Am. 101, 1431–1437. https://doi.org/10.1785/0120100238

Wilcox, R.E., Harding, T.P., Seely, D.R., 1973. Basic wrench tectonics. AAPG Bull. 57, 74–96.

Wintle, A.G., Murray, A.S., 2006. A review of quartz optically stimulated luminescence characteristics and their relevance in single-aliquot regeneration dating protocols. Radiat. Meas. 41, 369–391. https://doi.org/10.1016/j.radmeas.2005.11.001

Xu, X., Ma, X., Deng, Q., 1993. Neotectonic activity along the Shanxi rift system, China. Tectonophysics 219, 305–325. https://doi.org/10.1016/0040-1951(93)90180-R

Zechar, J.D., Frankel, K.L., 2009. Incorporating and reporting uncertainties in fault slip rates. J. Geophys. Res. Solid Earth 114, B12407. https://doi.org/10.1029/2009JB006325

Zhao, B., Zhang, C., Wang, D., Huang, Y., Tan, K., Du, R., Liu, J., 2017. Contemporary kinematics of the Ordos block, North China and its adjacent rift systems constrained by dense GPS observations. J. Asian Earth Sci. 135, 257–267. https://doi.org/10.1016/j.jseaes.2016.12.045

Ziegler, P.A., van Wees, J.-D., Cloetingh, S., 1998. Mechanical controls on collision-related compressional intraplate deformation. Tectonophysics 300, 103–129. https://doi.org/10.1016/S0040-1951(98)00236-4

Zinke, R., Dolan, J.F., Dissen, R.V., Grenader, J.R., Rhodes, E.J., McGuire, C.P., Langridge, R.M., Nicol, A., Hatem, A.E., 2015. Evolution and progressive geomorphic manifestation of surface faulting: A comparison of the Wairau and Awatere faults, South Island, New Zealand. Geology 43, 1019–1022. https://doi.org/10.1130/G37065.1

Zuza, A.V., Yin, A., Lin, J., Sun, M., 2017. Spacing and strength of active continental strike-slip faults. Earth Planet. Sci. Lett. 457, 49–62. https://doi.org/10.1016/j.epsl.2016.09.041